The Henryk Niewodniczański
INSTITUTE OF NUCLEAR PHYSICS
Polish Academy of Sciences
ul. Radzikowskiego 152, 31-342 Kraków, Poland
www.ifj.edu.pl/badania/publikacje
Kraków, April 2019

Photoproduction cross section measurements in ultra-peripheral Pb-Pb and p-Pb collisions at the LHC with ALICE

Christoph Mayer

Habilitation Thesis

To my teachers

Wydano nakładem Instytutu Fizyki Jądrowej im. Henryka Niewodniczańskiego
Polskiej Akademii Nauk
Kraków 2019

Recenzent: prof. dr hab. Marek Kowalski

ISBN 978-83-63542-14-6

Contents

1 Introduction **4**

1.1 Ultra-peripheral collisions 4

1.2 Equivalent photon approximation 5

1.3 Nuclear breakup in coincidence with photoproduction 9

1.4 A flat MC generator for $\rho^0 \to \pi^+\pi^-$ 11

2 The ALICE detector **12**

2.1 ITS 13

2.2 TPC 14

2.3 TOF 16

2.4 VZERO 17

2.5 AD 19

2.6 ZDC 23

2.7 Muon spectrometer 24

3 Low-mass vector meson production **26**

3.1 ρ^0 photoproduction in Pb-Pb collisions at $\sqrt{s_{NN}} = 2.76$ TeV 26

3.2 ρ^0 photoproduction in Pb-Pb collisions at $\sqrt{s_{NN}} = 5.02$ TeV 38

4 $\gamma\gamma$ processes in Pb-Pb collisions at $\sqrt{s_{NN}} = 2.76$ TeV **41**

4.1 Low-mass continuum dielectron photoproduction 41

4.2 High-mass continuum dielectron photoproduction 41

4.3 Low- and high-mass continuum dielectron photoproduction 45

5 High-mass vector meson production **46**

5.1 J/ψ photoproduction in Pb-Pb collisions at $\sqrt{s_{\mathrm{NN}}} = 2.76$ TeV 46

5.2 J/ψ photoproduction in p-Pb collisions at $\sqrt{s_{\mathrm{NN}}} = 5.02$ TeV 49

6 Outlook on LHC run 3 and 4 **56**

6.1 ALICE upgrades for LHC Run 3 and 4 56

6.2 Prospects for UPC measurements in LHC Run 3 and 4 60

7 Summary and conclusions **62**

8 Author's contribution **64**

9 Acknowledgments **66**

1 Introduction

Ultra-peripheral collisions of ultra-relativistic lead ions are a tool for studying γ-nucleus or $\gamma\gamma$ interactions at the LHC. Beams of lead ions at the LHC are a source of intense photon fluxes with very high energies, due to the effect of Lorentz contraction and the fact that the equivalent flux of almost real photons around lead ions is proportional to the square of their charge.

Since in ultra-peripheral collisions the impact parameter is greater than the sum of the nuclear radii, hadronic interactions are suppressed and electromagnetic interactions dominate. Experimentally, ultra-peripheral collision events are characterized by very low multiplicities in the central rapidity region and rapidity gaps outside central rapidity.

In this thesis, photoproduction cross section measurements performed by ALICE (A Large Ion Collider Experiment) in ultra-peripheral collisions are summarized. After a review of ultra-peripheral physics in this section, the sub-detectors of ALICE used in ultra-peripheral analyses are described in section 2. Section 3 contains a review of ALICE measurements of ρ^0 photoproduction in Pb-Pb collisions at $\sqrt{s_{\mathrm{NN}}} = 2.76$ and 5.02 TeV, and section 4 summarizes ALICE measurements of continuum $\gamma\gamma \to e^+e^-$ photoproduction in Pb-Pb collisions at $\sqrt{s_{\mathrm{NN}}} = 2.76$ TeV. ALICE measurements of J/ψ photoproduction in Pb-Pb collisions at $\sqrt{s_{\mathrm{NN}}} = 2.76$ TeV and in p-Pb collisions at $\sqrt{s_{\mathrm{NN}}} = 5.02$ TeV are discussed in section 5. In section 6 detector upgrades for LHC run 3 and 4, and prospects for ultra-peripheral measurements in run 3 and 4 are described. The last section contains a summary and conclusions.

1.1 Ultra-peripheral collisions

A collision of two ultra-relativistic ions is called ultra-peripheral, when the impact parameter b is larger than the sum of the radii of the two ions, see figure 1.1. As a consequence the interaction between the two ions is dominated by electromagnetic processes, while hadronic interactions between the two ions are suppressed. For a review of ultra-peripheral physics see [1–3] and the references therein. Ultra-peripheral collision are called *coherent* if the photon is emitted coherently by all nucleons and *incoherent* if it is emitted by a fraction of all nuclei. When the interaction is coherent (incoherent), the transverse momentum of the produced state is small (large).

As shown in figure 1.2 there are two main ways in which ultra-peripheral collisions can proceed: $\gamma\gamma$ interactions and γ-nucleus interactions, where in the latter case the nucleus may break up due to additional photon exchanges. In this thesis we present ALICE measurements of ultra-peripheral processes in Pb-Pb collisions at the LHC covering all three of these modes.

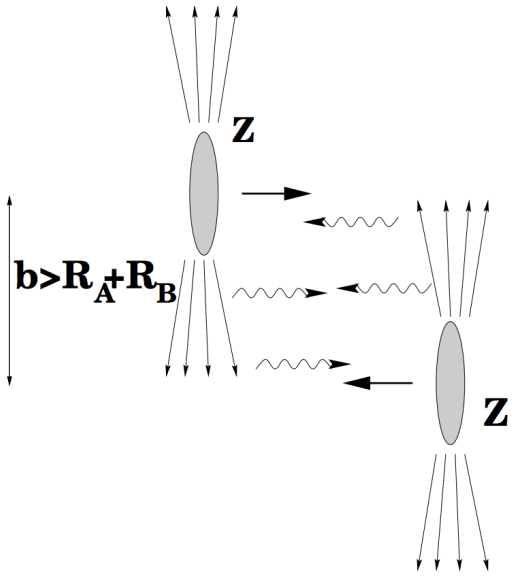

Fig. 1.1: Schematic diagram of an ultra-peripheral collision of two ions [2]. In ultra-peripheral collisions the impact parameter, b, is larger than the sum of the two radii, $R_A + R_B$.

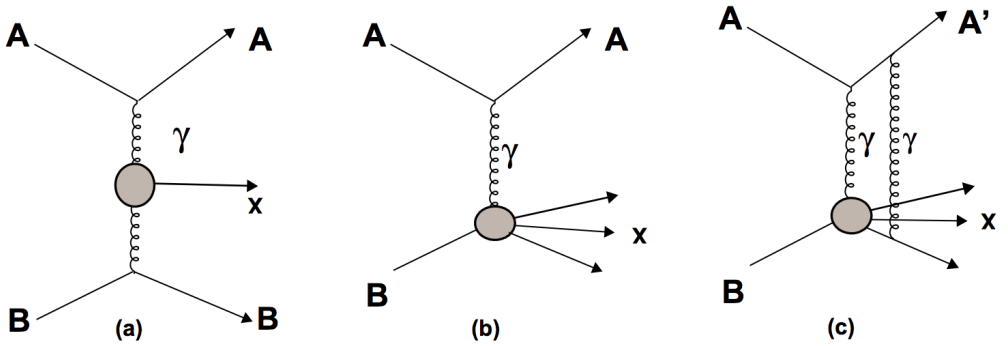

Fig. 1.2: A schematic view of (a) an electromagnetic interaction where photons emitted by the ions interact with each other, (b) a photon-nuclear reaction in which a photon emitted by an ion interacts with the other nucleus, (c) photo-nuclear reaction with nuclear breakup due to photon exchange [2].

1.2 Equivalent photon approximation

A long time ago it was realized by E. Fermi [4, 5] and subsequently Weizsäcker and Williams [6, 7] that the electromagnetic field around an ultra-relativistic nucleus can be described as a flux of almost-real photons. In this so-called equivalent photon approximation, the number of photons per unit area and per unit energy at a distance b from a given ultra-relativistic nucleus with Lorentz factor γ is given by [1, 2, 8]

$$\frac{\mathrm{d}^3N(k,b)}{\mathrm{d}k\mathrm{d}^2b} = \frac{Z^2\alpha}{\pi^2}\frac{k}{(\hbar c)^2}\frac{1}{\gamma^2}\left[K_1^2(x)+\gamma^{-2}K_0^2(x)\right], \quad x = kb/\gamma\hbar c\,, \tag{1.1}$$

where $\alpha \approx 1/137$ is the electromagnetic fine structure constant, and K_1, K_0 are modified Bessel functions. For ultra-relativistic ions, *i.e.*, $\gamma \gg 1$, the second summand can be neglected.

The equivalent photon flux in Equation (1.1) is given in the rest frame of the nucleus: the Lorentz boost γ in the frame of the target nucleus is related to the Lorentz boost in the collider center of mass frame, Γ_{CM}, by $\gamma = 2\Gamma_{\mathrm{CM}}^2 - 1$, and the Lorentz factor of a moving nucleus is $\gamma = E_A/M_A \gg 1$ where E_A and M_A denote the energy and the mass of the nucleus, respectively. Because the equivalent photon flux in Equation (1.1) is proportional to Z^2, it is enhanced by a factor of $82^2 = 6724$ in Pb-Pb collisions compared with proton-proton collisions. The virtuality of the photons around an ultra-relativistic nucleus is bounded by $|q|^2 < \hbar c/R_A$ [2] which for lead nuclei translates into $|q|^2 \approx (30\mathrm{MeV})^2$.

The photon flux for gamma-nucleus interaction is obtained by integrating equation (1.1) over the two-dimensional impact parameter space:

$$\frac{\mathrm{d}N_\gamma}{\mathrm{d}k} = \int \mathrm{d}^2 b P(b) \frac{\mathrm{d}^3 N(k,b)}{\mathrm{d}k \mathrm{d}^2 b} \,, \tag{1.2}$$

where $P(b)$ is the probability for having no hadronic interaction at impact parameter b, see, *e.g.*, [9, 10]. Similarly, the photon flux for two-gamma interactions is defined as

$$\frac{\mathrm{d}^2 N_{\gamma\gamma}}{\mathrm{d}k_1 \mathrm{d}k_2} = \int \mathrm{d}^2 b_1 \mathrm{d}^2 b_2 P\big(|b_1 - b_2|\big) \frac{\mathrm{d}^3 N(k_1,b_1)}{\mathrm{d}k_1 \mathrm{d}^2 b_1} \frac{\mathrm{d}^3 N(k_2,b_2)}{\mathrm{d}k_2 \mathrm{d}^2 b_2} \,. \tag{1.3}$$

The probability for having no hadronic reactions is [9]

$$P(b) = \exp\big(-\sigma_{\mathrm{NN}} T_{\mathrm{AA}}(b)\big) \,, \tag{1.4}$$

where σ_{NN} is the nucleon-nucleon interaction cross section, and $T_{\mathrm{AA}}(b)$ is related to the so-called nuclear thickness, $T_{\mathrm{A}}(b)$,

$$T_{\mathrm{AA}}\big(|\vec{b}|\big) = \int \mathrm{d}^2 r T_{\mathrm{A}}(\vec{r}) T_{\mathrm{A}}\big(\vec{r} - \vec{b}\big) \,, \tag{1.5}$$

and the nuclear thickness is obtained by integrating over the nuclear density

$$T_{\mathrm{A}}\big(\vec{r}\big) = \int \mathrm{d}z \rho_{\mathrm{A}}\Big(\sqrt{|\vec{r}|^2 + z^2}\Big) \,. \tag{1.6}$$

One parametrization of the nuclear density is due to Woods and Saxon [11],

$$\rho_{\mathrm{A}}(r) = \frac{\rho_0}{1 + \exp\big[(r - r_A)/a\big]} \,, \tag{1.7}$$

where ρ_0 is a normalization constant, r_A is the nuclear radius, and the so-called skin depth a

parametrizes the diffuseness of the nuclear surface. Equation (1.4) is motivated by the fact that the number of nucleon-nucleon collisions follows a Poisson distribution with mean $\sigma_{\mathrm{NN}} T_{\mathrm{AA}}(b)$.

The equivalent photon fluxes in equations (1.2) and (1.3) can be used to relate cross section in nucleus-nucleus collisions to elementary γ-nucleus and $\gamma\gamma$ cross sections, *i.e.*, for γ-nucleus processes we have

$$\sigma(AA \to AAV) = 2 \int \mathrm{d}k \frac{\mathrm{d}N_\gamma}{\mathrm{d}k} \sigma(\gamma A \to AV) \,, \tag{1.8}$$

where the factor of two is there because the photons can be emitted by both nuclei. The photon energy, k, is related to the final state meson rapidity, y, as

$$y = \ln \frac{k}{2M_V} \,, \tag{1.9}$$

where M_V is the mass of the produced vector meson. An example for such an interaction is the photo-production of ρ^0 mesons in Pb-Pb collisions, see section 3.

In two-photon interactions the final state rapidity Y and invariant mass W are related to the photon energies k_1 and k_2 as follows

$$W = \sqrt{4k_1k_2} \,, \quad Y = \frac{1}{2} \ln\left(k_1/k_2\right) \,, \qquad \mathrm{d}k_1\mathrm{d}k_2 = \frac{W}{2}\mathrm{d}W\mathrm{d}Y \,, \tag{1.10}$$

and this can be used to relate the cross section of a given two-gamma process in AA$\to$ AAX collisions to the cross section $\gamma\gamma \to X$ as follows:

$$\sigma(AA \to AAX) = \iint \frac{\mathrm{d}^2 N_{\gamma\gamma}}{\mathrm{d}W\,\mathrm{d}Y} \sigma(\gamma\gamma \to X) \mathrm{d}W\mathrm{d}Y \,. \tag{1.11}$$

In section 4, ALICE measurements of continuum photoproduction $\gamma\gamma \to e^+e^-$ in Pb-Pb collisions are described.

The nuclear form factor is the Fourier transform of the nuclear density. Since the Woods-Saxon potential (1.7) cannot be analytically Fourier transformed, a good approximation, used *e.g.*by STARLIGHT [9], is as follows, see also Fig. 1.3,

$$F\left(q = \sqrt{|t|}\right) = \frac{4\pi\rho_0}{Aq^3}\left[\sin(qr_A) - qR_A\cos(qR_A)\right]\frac{1}{1+a^2q^2} \tag{1.12}$$

where q denotes the 4-momentum transfer q and $t^2 \approx p_T^2$.

One way to obtain the cross section for γ-nucleus vector meson photo-production, $\gamma A \to VA$, is via a Glauber calculation, where $\gamma p \to Vp$ cross sections, *e.g.*, measured at HERA, are used as an input, see fig. 1.4. This method is used, *e.g.*, in STARLIGHT [9, 10].

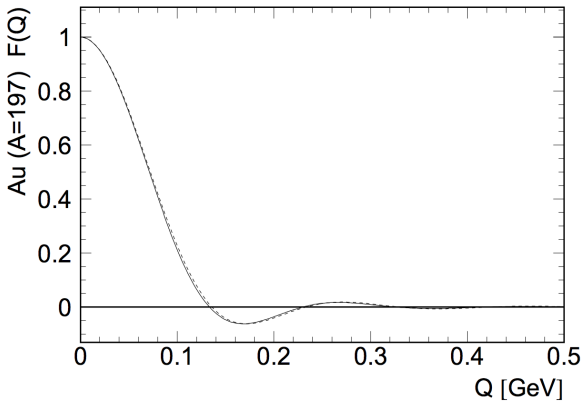

Fig. 1.3: The electromagnetic form factor for gold [9]. The solid line is the exact result from Fourier transformation of a Woods-Saxon potential, and the dotted line from equation (1.12).

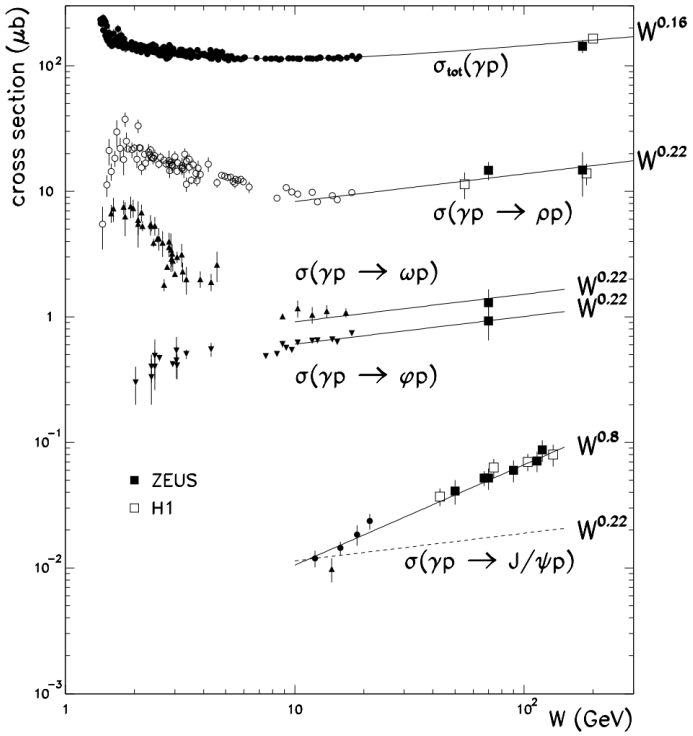

Fig. 1.4: Total and elastic vector meson photoproduction measurements as a function of $W_{\gamma p}$ at HERA [12].

While the cross sections for γ-nucleus vector meson photo-production in Pb-Pb collisions are only indirectly related to $\gamma p \to Vp$ cross sections, *i.e.*, using a Glauber model calculation, in pA collisions the relation between them is more direct: for instance in exclusive vector meson production off protons, the cross section measured in pA collisions is related to the γp cross section by multiplication with the photon flux, *i.e.*,

$$\frac{\mathrm{d}\sigma\left(pA \to VpA\right)}{\mathrm{d}y} = k\frac{\mathrm{d}N_\gamma}{\mathrm{d}k}\,\sigma\left(\gamma p \to Vp\right)\,, \tag{1.13}$$

where k is related to y as in equation (1.9). The photon can be emitted either from the proton or from the nucleus. However, photon emission by the nucleus is strongly enhanced with respect to that from the proton because of the large electric charge of the nucleus [13, 14]. The rapidity y in the laboratory frame at which the vector meson, *e.g.*, a J/ψ, is measured, is related to a γp energy $W_{\gamma p}$ as follows,

$$W_{\gamma p}^2 = 2E_p M_V \exp(-y) \tag{1.14}$$

where E_p is the energy of the proton beam. Therefore, by measuring vector meson production in different rapidity intervals, different ranges in $W_{\gamma p}$ can be probed.

1.3 Nuclear breakup in coincidence with photoproduction

In coincidence with vector meson photoproduction there may be so-called final state interactions which lead to nuclear excitations, as shown in the Feynman diagrams in Figure 1.5. Experimentally such interactions can be measured by detecting neutrons emitted from the excited nuclei, *e.g.*, in zero-degree calorimeters. Following the discussion in [15], we distinguish between two

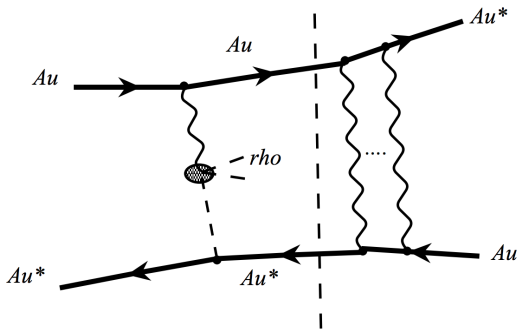

Fig. 1.5: The dominant Feynman diagrams for vector meson production with nuclear excitation [15].

cases: (1) a general Coulomb excitation leading to the emission of at least one neutron, called Xn, and (2) the emission of exactly one neutron corresponding to an excitation to the giant dipole resonance of the nucleus, called 1N.

The probability for an excitation to any state emitting at least one neutron (Xn) is given, to lowest order, by the following equation

$$P_{\mathrm{Xn}}^{\mathrm{1st-order}}(b) = \int \mathrm{d}k \frac{\mathrm{d}^3 n}{\mathrm{d}k \mathrm{d}^2 b} \sigma_{\gamma A \to A^\star}(k) \ . \tag{1.15}$$

Here, $\sigma_{\gamma A \to A^\star}(k)$ denotes the cross section for nuclear excitation. It is obtained from experimental data, see [16]. The dominant contribution to this cross section is due to the giant dipole resonance which can be clearly seen at low energies in figure 1.6.

More precisely, equation (1.15) corresponds to the mean number of excitations at a given impact

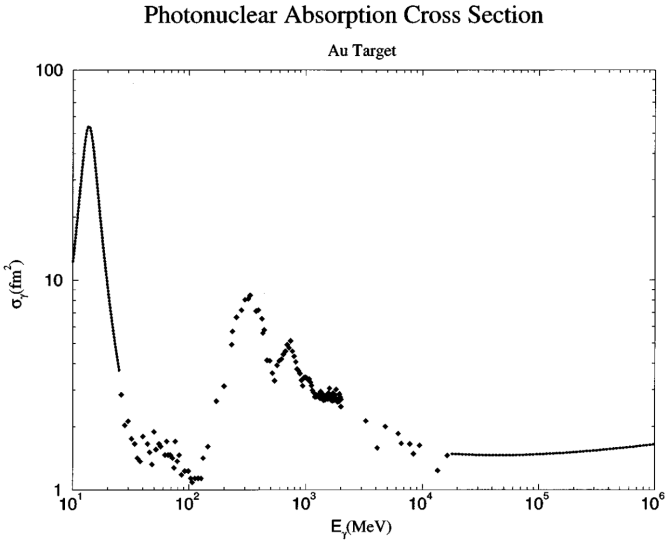

Fig. 1.6: Photo-nuclear absorption cross section as utilized for Au Coulomb dissociation calculations [16].

parameter b. Using Poisson statistics, the probability P_N for having exactly N excitations is

$$P_N = \frac{p(1)^N}{N!} e^{-p(1)} \,, \tag{1.16}$$

with $p(1)$ denoting the probability for having one excitation. Therefore the probability for emitting at least one neutron is given by the following expression,

$$P_{\mathrm{Xn}}(b) = 1 - \exp\left(P_{\mathrm{Xn}}^{\mathrm{1st-order}}(b)\right) \,, \tag{1.17}$$

i.e., the probability for not emitting zero neutrons. When the integral over k in equation (1.15) is truncated to include only the giant dipole resonance we obtain $P_{\mathrm{1n}}^{\mathrm{1st-order}}(b)$ which in turn can be used to find the probability for emitting exactly one neutron,

$$P_{\mathrm{1n}}(b) = P_{\mathrm{1n}}^{\mathrm{1st-order}}(b) \exp\left(-P_{\mathrm{1n}}^{\mathrm{1st-order}}(b)\right) \,. \tag{1.18}$$

In events with mutual excitations of both nuclei, each excitation occurs independently, so the probabilities (1.17) or (1.18) are multiplied. We distinguish four cases: (1) 0N0N — no neutron emitted by any nucleus, (2) XN — at least one neutron emitted by any nucleus, (3) 0NXN — no neutron emitted by one nucleus and at least on neutron emitted by the other nucleus, and (4) XNXN — at least one neutron emitted by both nuclei. For calculating cross section for vector meson photoproduction accompanied with neutron emission, the appropriate combination of the probabilities in (1.17) and in (1.18) are included in the integration over impact parameter space in equation (1.2).

1.4 A flat MC generator for $\rho^0 \to \pi^+\pi^-$

Here we describe a method to generate 4-vectors of a given state X decaying into two daughter particles, for instance, $\rho^0 \to \pi^+\pi^-$. As an input we use the rapidity Y, the transverse momentum p_T, and the invariant-mass M of the state X. The 4-vector of X can be parametrized as

$$v = \left[p_T \cos\alpha,\ p_T \sin\alpha,\ M_T \sinh y,\ M_T \cosh y\right] , \quad M_T^2 = M^2 + p_T^2 \tag{1.19}$$

where the angle α is uniformly distributed in $[0, 2\pi)$ and M_T is called the transverse mass.

The 4-momenta of the two daughter particles can be generated as follows: (1) generate a 3-vector $\vec{p}$ with length $|\vec{p}| = \sqrt{M^2/4 - m^2}$ and a random uniformly distributed angle in the transverse plane (x,y). Here, m denotes the mass of the daughter particle. The distribution of the θ angle of $\vec{p}$ is determined by the combination of the spin of the mother particle and the type of the daughter particles into which it decays. For instance, when a spin-1 particle decays into two pions, the distribution in θ is given by:

$$\frac{\mathrm{d}n}{\mathrm{d}\cos\theta} = 1 - \cos^2\theta , \qquad \text{for} \quad \text{Spin1} \to \pi^+\pi- \ . \tag{1.20}$$

Then, (2), tn the rest frame of X the 4-momenta of the two daughter particles are obtained as

$$v_\pm = \left[\pm\vec{p},\ M/2\right] , \quad \text{in the rest frame of } v , \tag{1.21}$$

and (3), in a final step, the 4-vectors of the daughter particles $v_\pm$ are boosted into the detector center-of-mass frame using v.

This method is used by STARLIGHT, where the distributions of (M, Y, p_T) are derived from numerical calculations. However one can use this method also with flat distributions for M, Y, and for p_T, see section 3.

2 The ALICE detector

Figure 2.1 shows a schematic view of the ALICE detector [17–19]. For a full description of the ALICE experiment and its performance see [20, 21]. The central detectors are situated inside a large solenoid magnet providing a $B = 0.5$ T field.

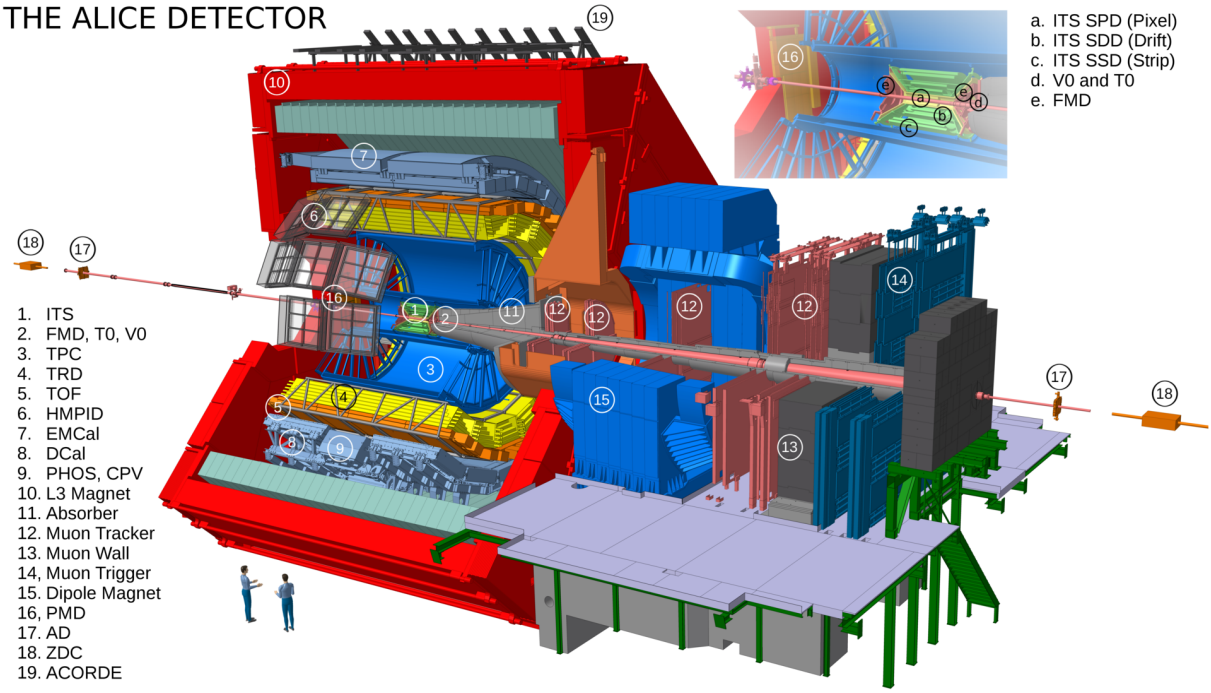

Fig. 2.1: The ALICE detector

For the ultra-peripheral analyses presented in this thesis the inner tracking system (ITS) and the time projection chamber (TPC) are used for tracking in the central rapidity region, VZERO and AD are used for vetoing on activity outside the central region, and the zero-degree calorimeters (ZDC) are used to detect neutrons emitted from lead ions. In addition, the forward muon spectrometer is used for triggering on, and tracking of forward muons. Besides the vetoes on VZERO and on AD, a positive trigger condition is needed. Such positive trigger conditions are available thanks to the triggering capabilities of the two innermost layers of the ITS and of the time-of-flight TOF detector, and are described below.

Figure 2.2 shows the pseudo-rapidity coverage of some of the detectors used in ultra-peripheral analyses. Note that there is an almost continuous coverage in pseudo-rapidity between -7.0 and $+6.5$.

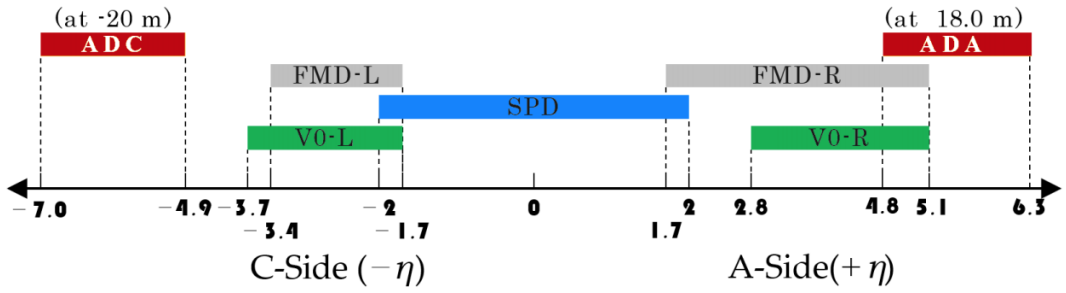

Fig. 2.2: Pseudo-rapidity coverage of ALICE detectors used in UPC triggers. Note that ADA,ADC were installed between LHC run 1 and run 2 and that the muon forward spectrometer and the zero-degree calorimeters are not shown in this figure.

2.1 ITS

The inner tracking system (ITS) consists of six layers of silicon detectors arranged in a cylindrical fashion around the beam pipe with the innermost layer at a radius $r = 3.9$ cm and the outermost layer at $r = 43$ cm. The two innermost layers are made of silicon pixel detectors (SPD), the two middle layer are made of silicon strip detectors (SSD), and the two outermost layers are made of silicon drift detectors (SDD). The six layers have a pseudo-rapidity acceptance of $|\eta| < 0.9$ w.r.t. a vertex at the nominal position at $z = 0$.

Besides being used for tracking and for precise vertex determination, the two innermost layers (SPD) participate in the generation of UPC triggers. They are located at 39 and 70 mm from the beam-pipe and use hybrid silicon pixel detectors with pixel size 50×425 μm^2. The passage of charged particles through a given pixel is provided as a binary output when the signal is above a set threshold. As the two layers comprising the SPD are more close to the beam pipe than the other four layer of the ITS, the pseudo-rapidity acceptance of the SPD, $|\eta| < 2.0$ for the inner layer and $|\eta| < 1.4$ for the outer layer, is larger than the acceptance of the ITS as a whole.

For triggering purposes the pixels are combined into 1,200 so-called fast-or (FO) chips, 400 in the inner and 800 in the outer layer, where the segmentation in the direction parallel to the beam line is 20 FO chips, both for inner and for outer layer, and 20 (40) FO chips in the transverse direction to the beam line in inner (outer) layer.

Using a powerful FPGA, a trigger can be generated from an arbitrary activity patters in these FO chips. As part of UPC triggers two trigger conditions were used

- ≥ 2 FO chips fired (inner or outer layer)
- a topological SPD trigger selecting back-to-back activity, see figure 2.3, which requires a 4-fold coincidence between inner and outer layer FO chips.

During LHC run 2 the SPD topological trigger described above was generalized to arbitrary, configurable opening angles and to two versions of forming the 4-fold coincidence, a more

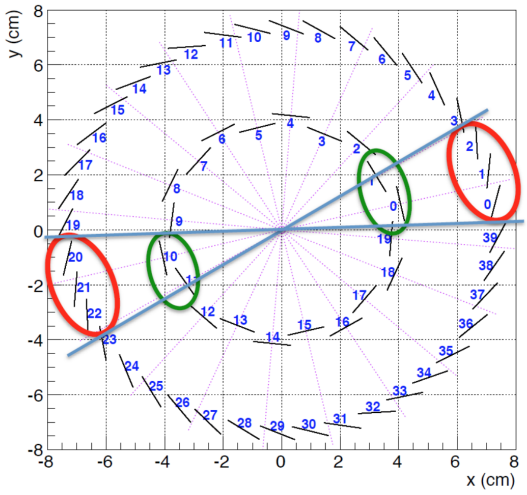

Fig. 2.3: SPD topological trigger selecting 4-fold coincidences of back-to-back activity in SPD FO chips.

narrow one and a more wide one.

In standard ALICE MC simulation the efficiency of active FO chips is assumed to be 100%, while in reality this efficiency depends on the how many tracks pass a given fast-or chip. Therefore a method was developed which evaluates this fast-or efficiency for low-multiplicity events as a function of the number of tracks crossing a FO chip, using minimum-bias triggered events. For the ultra-peripheral analyses described in the following sections, the efficiency for exactly one track passing through a FO chip was used, given that the track multiplicity for the described analyses is two, and therefore it is very unlikely that two tracks pass through the same FO chip.

2.2 TPC

The ALICE time-projection chamber (TPC) is the main tracking detector of the central barrel. It is an 88m^3 cylinder filled with a Ne-CO_2-N_2 gas mixture. This cylinder is divided into two drift regions by the central electrode located at its axial center, where between the two end caps and the central electrode there is a static electric field with 400 v/cm, see figure 2.4. When a charged particle traverses the TPC the gas is ionized along its track, and the released electrons drift in the electric field towards the end caps. At the end plates the electrons are amplified by multi-wire proportional chambers which consist of 570,132 pads that form the cathode plane. In this way, the transverse positions of a given track are determined by the projection to the end caps along the beam axis, while the information about the z coordinates is obtained from the measurement of the drift time. Because the gas in the TPC is at room temperature and subject to changes in atmospheric pressure, the drift velocity is measured regularly during data taking using a laser calibration system.

The TPC covers the full azimuth and $|\eta| < 0.9$ for full length tracks. For finding and reconstructing tracks in the TPC, two-dimensional clusters in pad-row–time planes are used as an

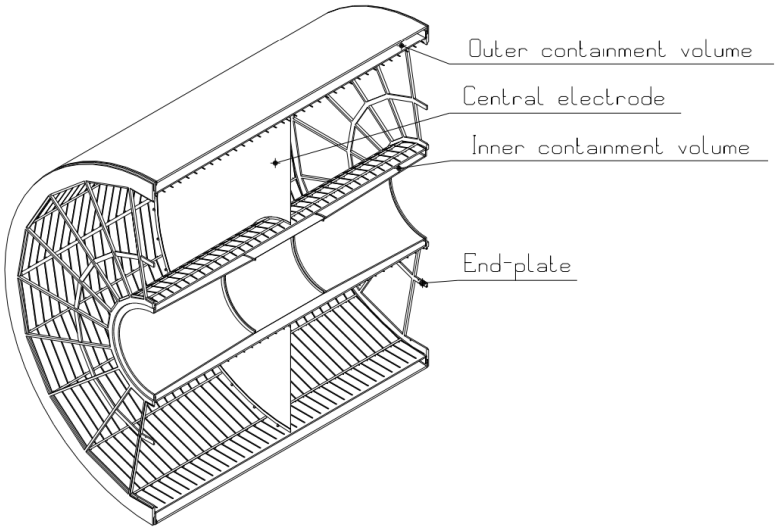

Fig. 2.4: Schematic view of the TPC field cage without readout chambers.

input, from which corresponding space points are reconstructed. The reconstruction of tracks then proceeds using a Kalman filter, taking into account the magnetic field, multiple scattering, energy loss in the gas, the removal of outliers, and distortions of the static electric due to the build up of positive space charge at high interaction rates.

One of the advantages of using a Kalman filter for tracking is that a given track reconstructed in the TPC can be followed through the ITS (and vice versa), improving the tracking precisions. Figure 2.5 shows TPC track finding efficiencies and ITS–TPC matching efficiencies for Pb-Pb collisions [21].

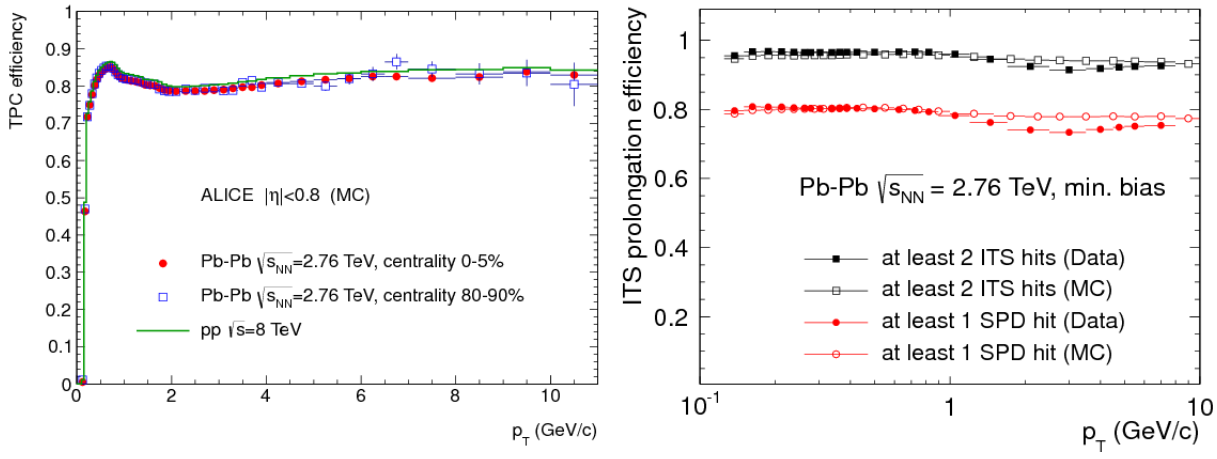

Fig. 2.5: Left: TPC track finding efficiency for primary particles in pp and Pb-Pb collisions (simulation). The efficiency does not depend on the detector occupancy [21]. Right: ITS–TPC matching efficiency vs. p_T for data and Monte Carlo for Pb-Pb collisions.

Unlike in minimum-bias events, in ultra-peripheral events there are very few tracks in an otherwise empty detector. For events consisting of two pions, figure 2.6 shows the resolution in

two-pion invariant-mass at fixed pair-p_T and the resolution in two-pion pair-p_T at fixed invariant mass.

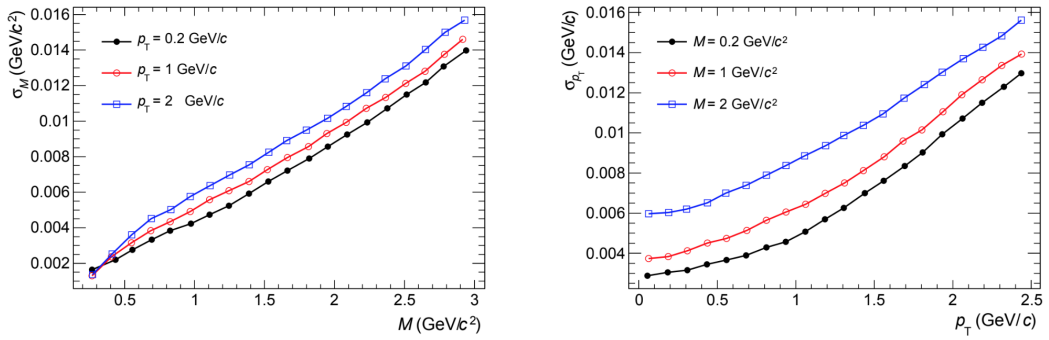

Fig. 2.6: Left: Invariant mass resolution as a function of invariant mass at fixed p_T of 2π system. Right: p_T resolution as a function of p_T at fixed invariant mass of 2π system. Results are obtained based on MC simulations. (Courtesy M. Poghosyan)

One of the advantages of using a time projection chamber is that the specific energy loss along a given track provides excellent particle identification, down to very low transverse momenta, see figure 2.7. For the ultra-peripheral analyses particle identification based on TPC dE/dx is used to separate pions from electrons.

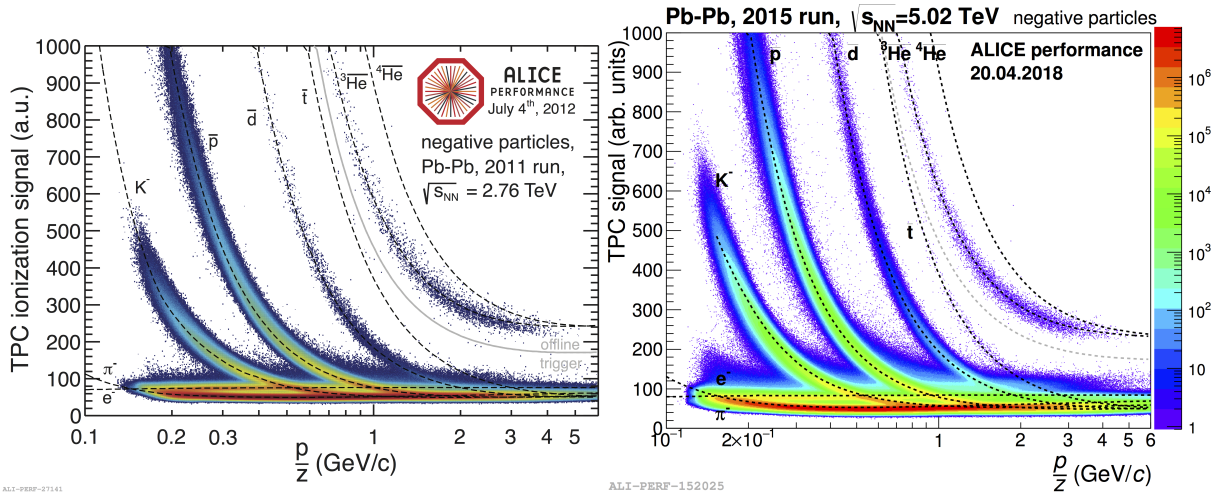

Fig. 2.7: TPC dE/dx vs. rigidity distribution for all events passing the offline trigger selection of events with at least one $Z > 1$ track candidate. Left (right): Pb-Pb collisions in LHC run 1 (run 2). Only negatively charged particles are shown.

2.3 TOF

The ALICE time-of-flight (TOF) detector is made of 1593 glass Multigap Resistive Plate chamber (MPRC) detectors [22, 23], each with a sensitive area of 7.4×120 cm^2. It covers pseudo-rapidities between -0.9 and +0.9 and the full azimuthal angle, except the area in front of the

PHOS detector. There are 152,928 read-out channels with time resolution of the order of 50 ps. Its performance is reported in [24].

While the main use of TOF is for particle identification and precise event time determination, see [25] and figure 2.8, for UPC purposes, TOF is used as part of UPC triggers.

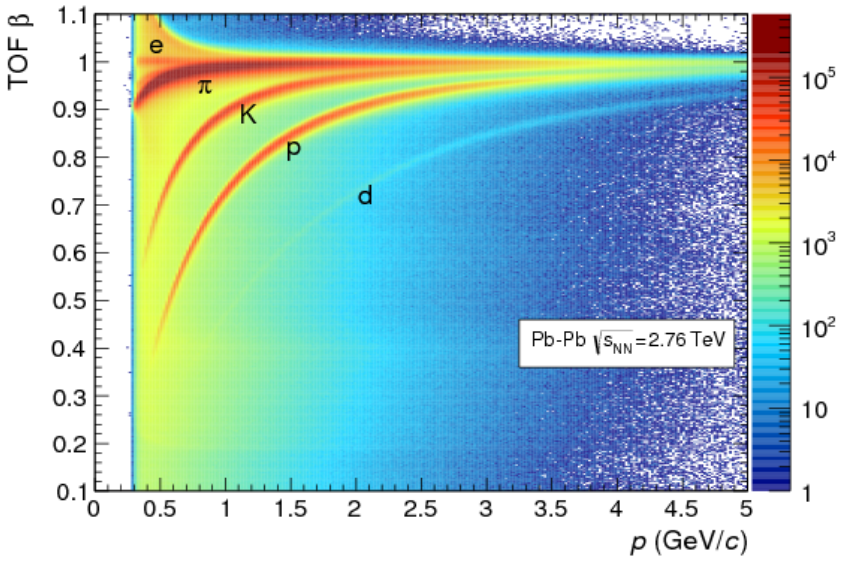

Fig. 2.8: Distribution of $\beta = v/c$ as measured by the TOF detector as a function of momentum for particles reaching the TOF in Pb-Pb interactions [21].

For the purpose of TOF trigger generation, its 152,928 read-out channels are grouped into 72×23 so-called maxi-pads. Based on activity patterns in these maxi-pads a trigger is generated. For the ultra-peripheral triggers used to collect the data the analyses described in this thesis two TOF trigger conditions were used:

- ≥ 2 TOF maxi-pads active (0OM2), and
- a topological TOF trigger selecting back-to-back activity patterns with opening angle $\geq 150^\circ$ and $2 \leq 6$ active TOF maxi-pads (0OMU) [26].

2.4 VZERO

The ALICE VZERO detector [27] consists of two arrays of counters located on both sides of the interaction point. Each of these arrays is made of 32 scintillators, where VZERO-A is located at $z = 330$ cm on the opposite to the muon spectrometer, and VZERO-C is located at $z = -90$ cm, see figure 2.9. The pseudo-rapidity coverage is $2.8 < \eta < 5.1$ for VZERO-A and $-3.7 < \eta < -1.7$ for VZERO-C w.r.t. a vertex at the nominal position at $z = 0$. Each scintillator array is segmented into counters distributed in four rings, see figure 2.10.

The light generated in the scintillators made of BC-404 material is guided by wavelength shifting fibers to photomultiplier tubes where it is converted into electrical pulses. These pulses

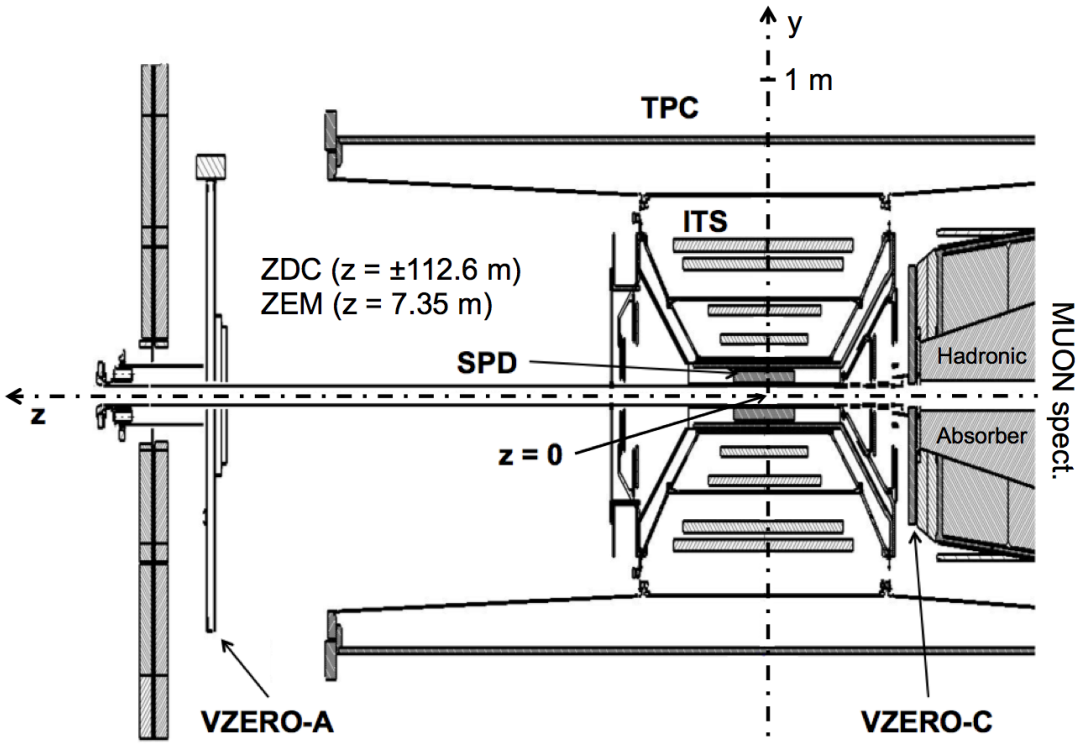

Fig. 2.9: Position of the two VZERO arrays within the general layout of the ALICE experiment [27].

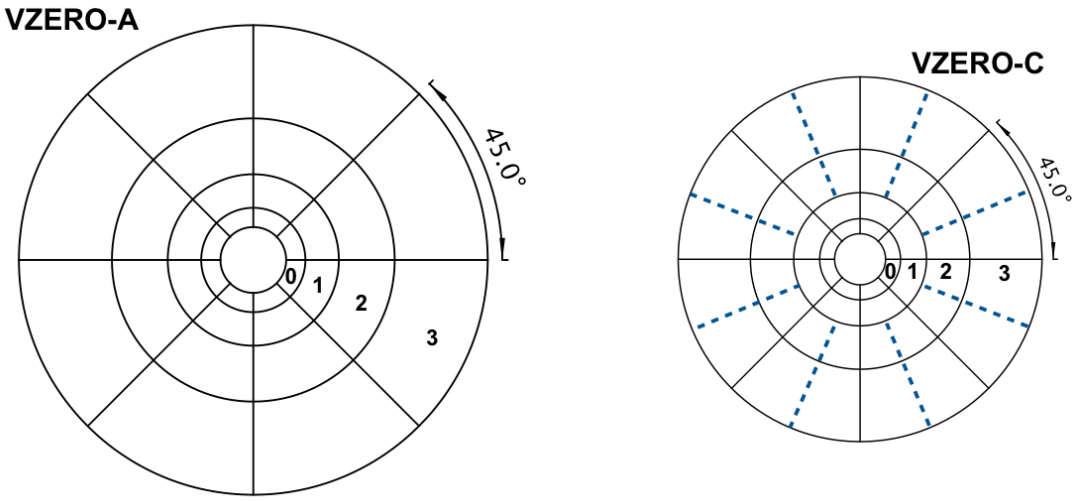

Fig. 2.10: Sketches of VZERO-A and VZERO-C arrays showing their segmentation. Scintillator thicknesses are 2.5 and 2 cm respectively. The scintillator segments on both sides of the dashed lines are connected to the same PMT. [27].

are then preamplified and pulse-shaped (PASA) and then processed in its front-end electronics. For this each signal is split into two paths, one amplified by a factor of 10 which is compared against a fixed threshold and a second path which is not amplified and then used to measured the integrated charge of the pulse in 25 ns intervals.

Besides providing a number of triggers based on the activity in the scintillators, the VZERO

front-end electronics measures in each of the 64 channels the charge of the pulse, its leading time and the pulse width, *i.e.*, the time over threshold. The time measurements are performed using a custom ASIC developed at CERN, called high-performance time digital converter (HPTDC) [28]. Figure 2.11 shows time correlations between VZERO-A and VZERO-C where beam-beam and beam-gas activity regions can be clearly distinguished.

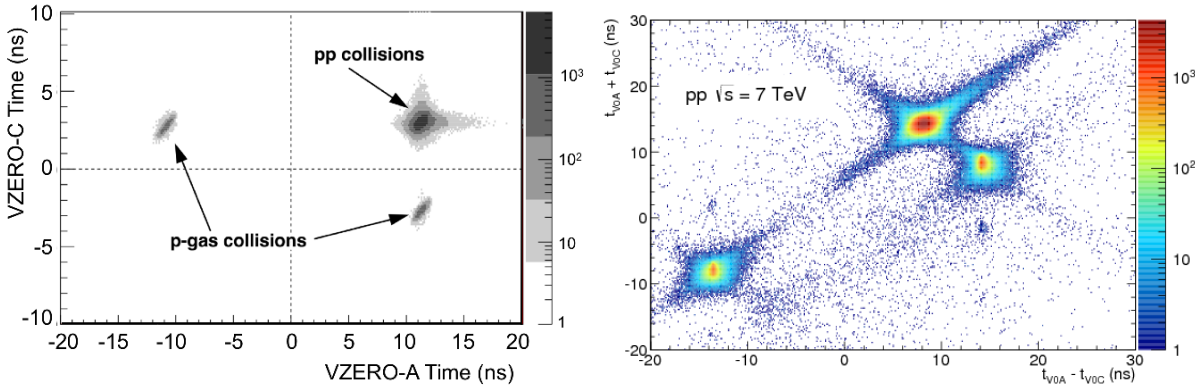

Fig. 2.11: Left: Weighted average time of flight of the particles detected in VZERO-C versus VZERO-A. The dashed line intersection represents the time of the collisions at the interaction point, or the crossing time of the background tracks at the vertical plane $z \approx 0$ [27]. Right: Correlation between the sum and difference of signal times in VZERO-A and VZERO-C [21]. Three classes of events – collisions at (8.3 ns, 14.3 ns), background from Beam 1 at (-14.3 ns, -8.3 ns), and background from Beam 2 at (14.3 *ns*,8.3 ns) – can be clearly distinguished.

One type of VZERO triggers is based on the time of a hit in a given VZERO channel: if the time is in a window compatible with collisions (beam-gas), a so-called BB (BG) trigger is issued. As part of ultra-peripheral triggers VZERO is used as a veto, *i.e.*, the online requirement (during data taking) is that there is no activity in the BB window in any VZERO channel. Then, offline, one can further clean up the data sample by requiring no HPTDC time measurements (offline veto).

2.5 AD

The Alice Diffractive (AD) detector was installed between LHC run 1 and run 2 [29]. It consists of two assemblies of plastic scintillator pads located on both sides of the interaction point, at about -20 m and $+18$ m, respectively. ADA is situated in the cavern at the A-side and ADC in the LHC tunnel just next to the last LHC dipole magnet, near the wall separating the tunnel on the C-side from the ALICE cavern, see figure 2.12.

Each station, ADA and ADC, consists of two layers of BC-404 scintillator pads where each layer is made of four pads of dimension $181 \times 216 \times 25$ mm^3, arranged around the beam pipe. In order to reduce background and electronic noise, coincidences between adjacent pads are required, which provides a natural trigger for cosmic muons.

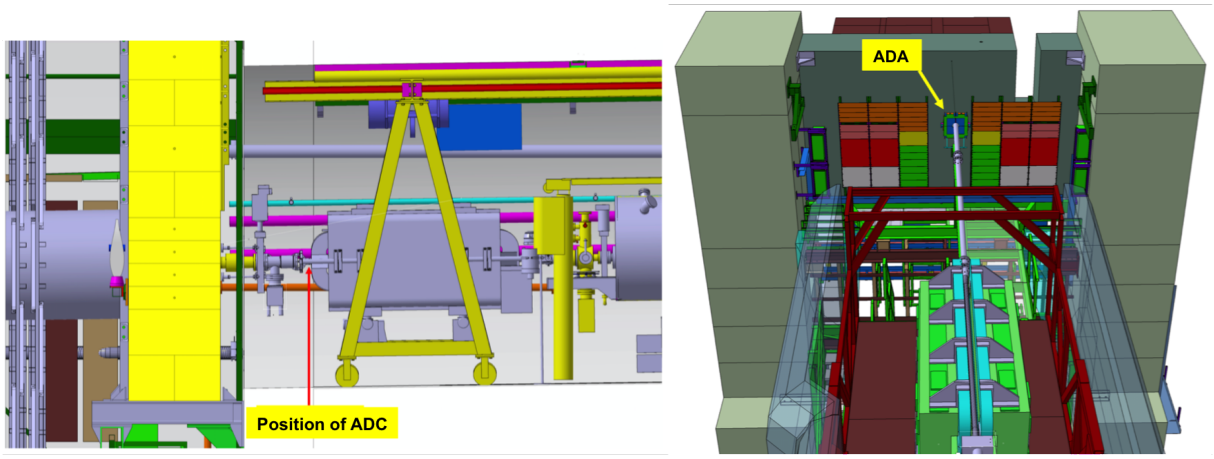

Fig. 2.12: Drawings showing the positions of the ADC (left) and of ADA (right). ADC is located in the LHC tunnel. It is using a small gap between the last dipole magnet and a flange that connects the LHC beam pipe to a vacuum pump. ADA is fixed onto the concrete wall (gray) which limits the space available for the ALICE experiment, and cannot be moved further away. (Courtesy T. Caudron)

The locations of ADA and ADC were carefully chosen in order to maximize the time differences at which signals from beam-gas and from collisions arrive when the LHC runs with 25 ns bunch spacing: the time-of-flight from the interaction point to ADC is $T_C = 65.2$ ns and to ADA $T_A = 56.6$ ns.

Signals from beam-gas from the same bunch are advanced w.r.t. collision signal by $-2T_A = -130.4$ ns and $-2T_C = -113.2$ ns, respectively, see figure 2.13. This can be easily seen by following one bunch, *e.g.*, arriving from the C-side and traveling towards the A-side. When it crosses ADC it may make a beam-gas signal. Following this bunch further to the interaction point it may interact with another bunch coming from the opposite side. Therefore the time difference between crossing ADC (beam-gas hit) and the signal in ADC from the collision is $2T_C$. When there are 25-ns spaced bunch trains in the LHC the minimum distance of any beam-gas signal w.r.t. a signal from a collision is 5.4 ns on C-side and 13.2 ns on A-side.

When particles traverse the BC-404 plastic scintillators, light is generated. This light is collected by two wavelength-shifting bars attached to both sides of each scintillator pad and then transferred by clear optical fibers to photo-multiplier tubes (PMT). On the C-side, the PMTs are located in the ALICE cavern while the scintillators are on the other side of the wall in the LHC tunnel.

When the light produced in the scintillator is absorbed in the wavelength shifting bars, it may be emitted at a different wavelength. The time behavior of this emission follows an exponential distribution with a time constant of about 8.5 ns for the used wavelength shifting bars made of the material EJ-280.

The electrical pulses from the PMTs are then transferred to the front-end-electronics, which is

based on the one from VZERO, using about 50 m long signal cables. Like for the VZERO detector the signal from a given PMT is split into two signal paths: in one path the signal is amplified and then compared to a fixed threshold from which the time, and time over threshold measurements are derived, while in the second signal path the signal is not amplified and its charge is integrated in intervals of one bunch crossing, *i.e.*, 25 ns. The main difference between the VZERO and AD front-end electronics is that in AD coincidences between adjacent pads are required which is not the case for VZERO.

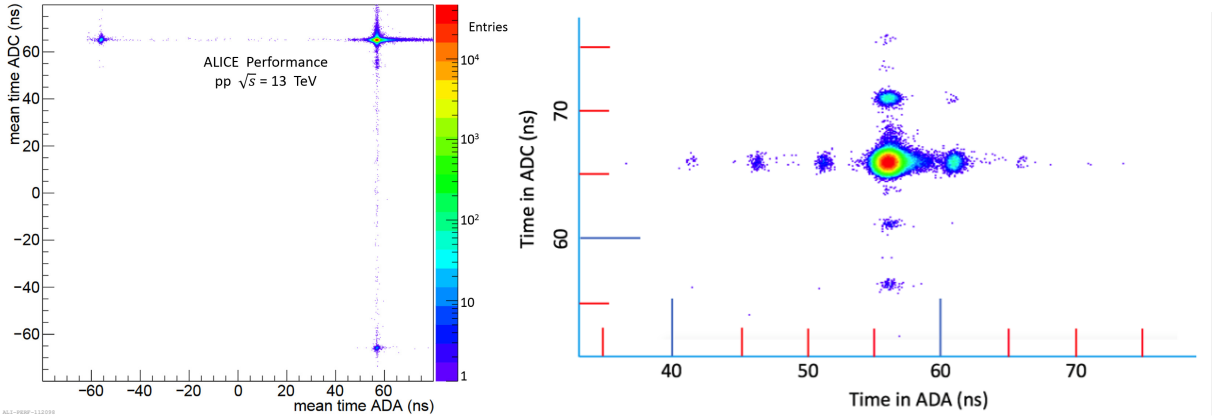

Fig. 2.13: Left: time measurement in ADC vs. time measurement in ADA in proton-proton collisions for run 234039. The secondary spots corresponds to beam background interactions. For single bunches, AD beam background arrives $-2T_A$ ($-2T_C$) earlier than collisions, resulting in an excellent rejection of beam background. Right: measured time in ADA versus measured time in ADC, obtained in Xe-Xe collisions, illustrating the excellent separation between the main bunch (center) and satellite bunches 5 ns away from each another. The small asymmetric tails are due to secondary particles produced in the material between the interaction point and the detectors. (Courtesy Jean-Pierre Revol)

The time resolution of AD depends on the high voltage (HV) gain settings of the PMTs and on the mean multiplicity seen by the scintillator modules. Typically it is about 0.4 ns on A-side and 0.3 ns on C-side, see figure 2.14. Due to the excellent time resolution, beam satellite bunches can be clearly distinguished, see 2.13 right.

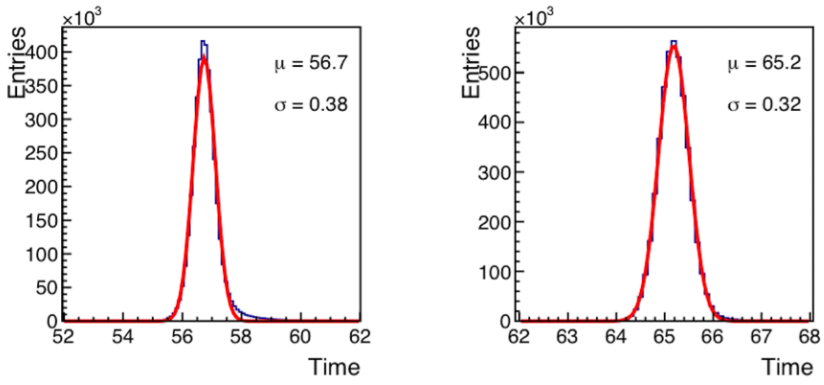

Fig. 2.14: Measured AD time distributions in ns, for A side (left) and C side (right), in Xe-Xe run 280234, showing a time resolution of 380 ps and 320 ps for A side and C side, respectively.

For adjusting and equalizing the gain of the PMTs, so-called gain curves are used, see figure 2.15. For the gain curves, the position of the 1-MIP peak in the charge distributions of a given channel is determined for different HV values and then fitted to the function $\left(\mathrm{HV}/a\right)^b$. These gain curves are updated 2–3 times per year, usually before the start of pp data taking in the beginning of each year and then again before data taking with Pb-Pb, p-Pb, or Xe-Xe collisions It is important to make these adjustments because it was found that the PMT response decreases with time (aging) which needs to be compensated for.

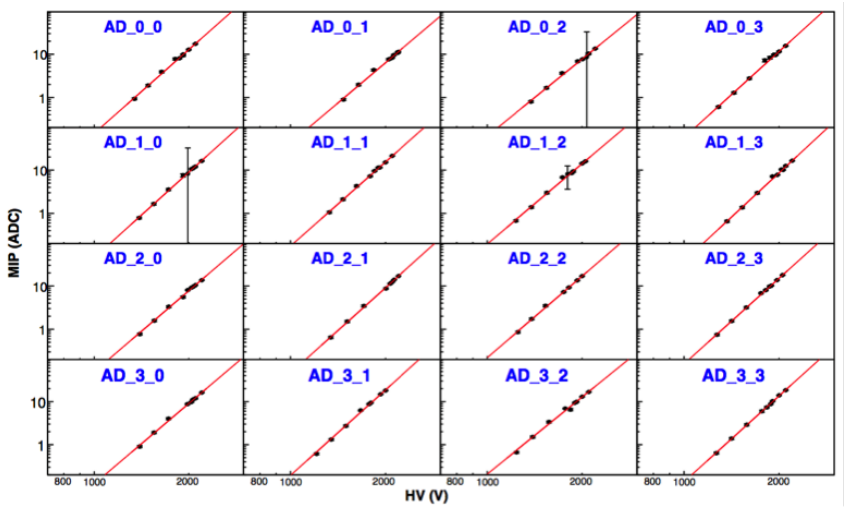

Fig. 2.15: AD gain curves obtained at the beginning of 2018 pp data taking period; the three points at the lowest high voltages were obtained from the 90% quantile of the charge distribution and converted into equivalent 1-MIP values in a combined fit as explained in the text.

Whenever a given pulse in a channel rises about the fixed threshold, a time measurement is made. If, in addition, (1) the time is inside a configurable timing window and (2) there is coincidence between adjacent pads, a trigger is generated. There are two, independently configurable time windows, called beam-beam (BB) and beam-gas (BG) windows. The BB window is adjusted to trigger on collisions and the BG window to trigger on beam-gas events. Figure 2.16 shows for each of the 16 channels the charge vs. raw time measurements: as the threshold is fixed, the time measurements of larger pulses are earlier than for smaller pulses. This time-slewing effect is corrected for during reconstruction. In addition, the vertical lines in figure 2.16 indicate the position of the BB window. It can be seen that the signals of all channels are aligned and inside the BB window. In particular, when AD is used as a veto in UPC triggers it is especially important that the tails of the pulses are as much as possible within the BB window.

Figure 2.17 shows a comparison of detection efficiencies for single diffraction with VZERO only and with AD and VZERO. Because AD is located at larger distances to the interaction point compared to VZERO it is sensitive to activity at larger pseudo-rapidities $|\eta|$, see also figure 2.2.

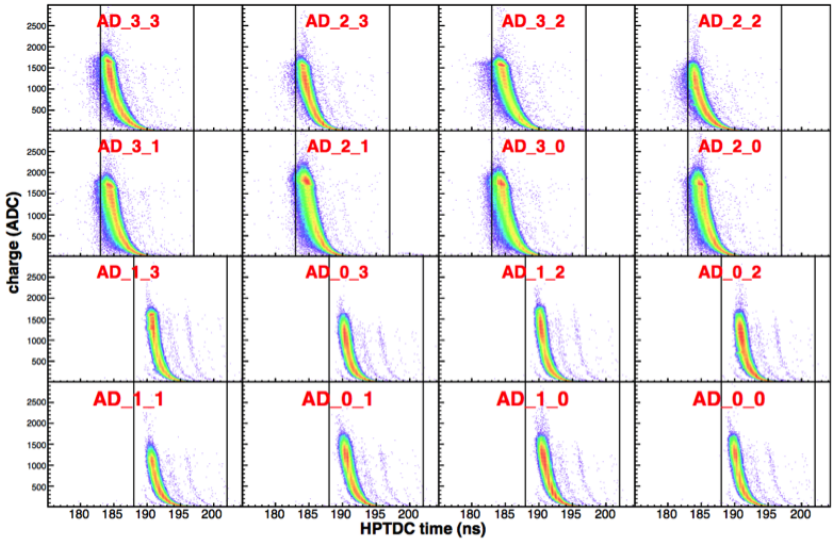

Fig. 2.16: Charge vs. HPTDC time in ns for a Pb-Pb run taken in 2018, and for the 16 AD channels. Vertical lines indicate the position of the beam-beam time window.

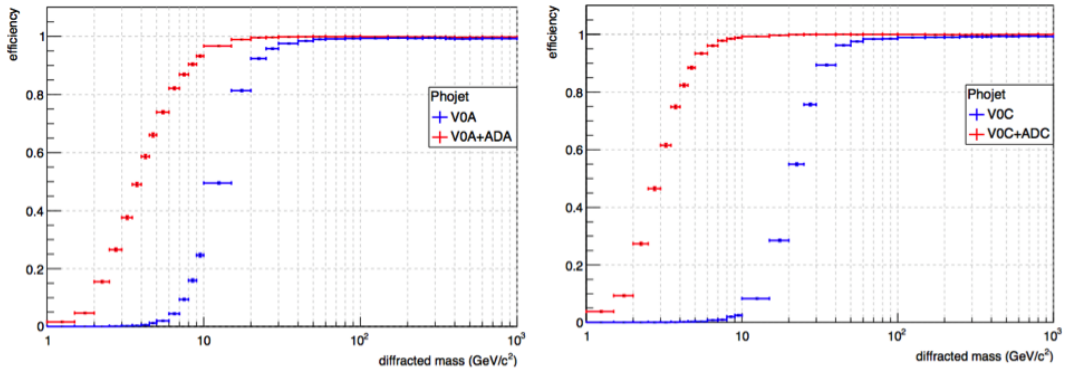

Fig. 2.17: A-side detection efficiency for A-side single diffraction at $\sqrt{s} = 13$ TeV, as a function of diffracted mass (left); C-side detection efficiency for C-side single diffraction at $\sqrt{s} = 13$ TeV, as a function of diffracted mass (right). Comparison with and without AD is shown. Efficiencies at 14 TeV are not expected to be significantly different from efficiencies at 13 TeV. (Courtesy E. Calvo)

2.6 ZDC

For detecting neutrons emitted by lead nuclei in ultra-peripheral collisions, a set of two neutron zero-degree calorimeters (ZDC) are used. They are located along the beam line in the LHC tunnel at a distance of about 114 m on both sides of the interaction point. At each side of the interaction points are two ZDCs: one for detecting neutrons and one for detecting protons.

The ZDCs consist of metal plates into which quartz optical fibers are embedded. The material of these plates is a tungsten alloy for the neutron ZDCs and brass for the proton ZDCs. When a high-energy particle crosses the ZDC, it may produce light due to the Cherenkov effect which is then guided by the optical fibers to photo-multiplier tubes where it is converted into an electric signal. The amplitude of these signals is proportional to the energy of the incoming neutrons

(or protons). For neutrons with $|\eta| > 8.8$ the detection probability in the ZDC is 99% [30].

Figure 2.18 shows the correlation between signals in the two neutron ZDCs where it can be seen that the resolution is good enough to measure single neutron emission. The fact that for Pb-Pb collisions,single neutron peaks are distinguishable helps in calibrating the signals from the photo-multiplier tubes, as it provides an absolute energy reference.

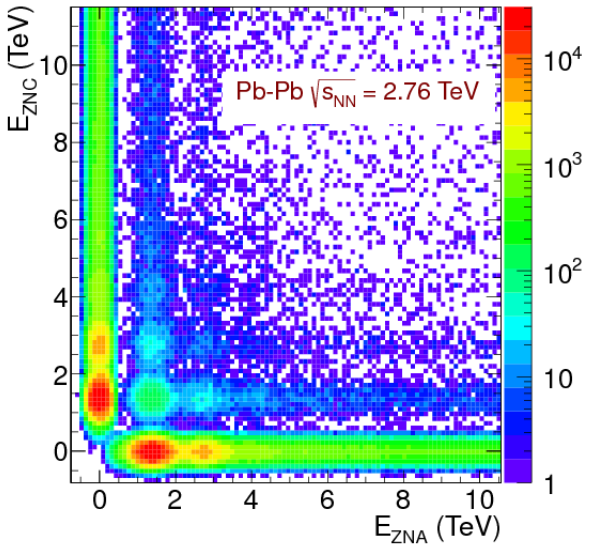

Fig. 2.18: Correlation between signals in the two neutron zero-degree calorimeters [21]. Single electromagnetic dissociation events produce a signal in only one of the calorimeters. Mutual dissociation and hadronic interactions populate the interior of the plot and can be distinguished from each other by the signal in ZEM.

2.7 Muon spectrometer

The ALICE forward muon spectrometer [31] consists of three components, a front absorber, a tracking system, and a trigger system, see figure 2.19. The conical front absorber is made of carbon, concrete and steel equivalent to 10 interaction lengths. It is there in order to suppresses all particles except muons coming from the interaction vertex. In addition, there is a conical absorber made of tungsten, lead and steel, that surrounds the beam pipe at small angles ($\Theta < 2°$) and shields the spectrometer from secondary particles produced in interactions of primary particles in the beam pipe.

The muon tracking system consists of five tracking stations, each one made of two planes of Cathode Pad Chambers. A 7.2 interaction-length iron wall is placed after the tracking stations. This iron wall is followed by the muon trigger system, which is made of four planes of Resistive Plate Chambers arranged in two stations. A dipole magnet is positioned at about 7 m from the interaction vertex and generates a magnetic field of 3 Tm (field integral). Due to this magnetic field, the momenta of muon tracks can be measured.

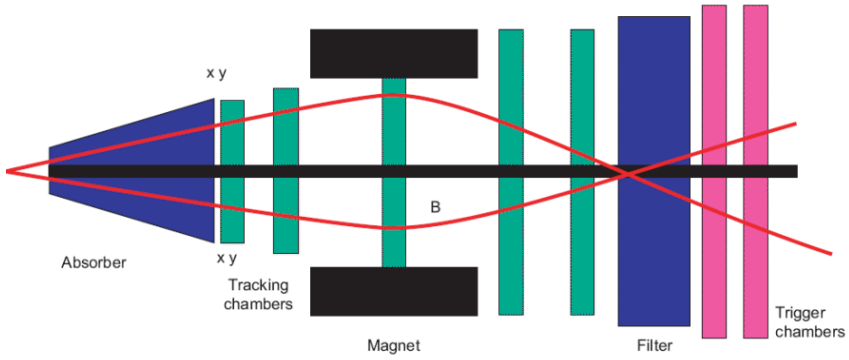

Fig. 2.19: Main components of the ALICE muon spectrometer.

The muon trigger system provides single-muon and dimuon triggers with a configurable p_T threshold, where due to the coarse grain of the trigger spatial information the p_T threshold is an approximate value. The pseudo-rapidity coverage of the ALICE muon spectrometer is $2.5 \leq \eta \leq 4$ and its acceptance extends down to zero transverse momenta.

3 Low-mass vector meson production

3.1 ρ^0 photoproduction in Pb-Pb collisions at $\sqrt{s_{NN}} = 2.76$ TeV

ALICE has measured for the first time the cross section of coherent ρ^0 photoproduction at mid-rapidity in ultra-peripheral Pb-Pb collisions at the LHC [32–34]. For the measurement of the coherent photoproduction cross section the decay channel $\rho^0 \to \pi^+\pi^-$, which has a branching ratio of almost 100% [35], was used. The measurement was done at mid-rapidity, $|y(\pi^+\pi^-)| < 0.5$, which translates into equivalent photon-nucleus energies in the range $36 < W_{\gamma N} < 59$ GeV with $\langle W_{\gamma N} \rangle = 48$ GeV. Compared to previous measurements, *e.g.*, at STAR [36], this corresponds to an increase of the corresponding photon-nucleus energy range by about a factor four.

3.1.1 Data sample and MC simulations

Two data samples were used which were collected with two different trigger conditions:

1. TOF only trigger: The trigger condition for this sample was ≥ 2 TOF maxi-pads fired. This is a minimum bias like trigger. In contrast to other minimum bias triggers based on coincidences between VZERO-A and VZERO-C, this trigger does include events with rapidity gaps due to UPC.
2. TOF+SPD+VZERO trigger: In addition to the TOF trigger described above, two or more fired SPD fast-or chips were required and a veto in both VZERO-A and in VZERO-C.

The integrated luminosity for both data samples was determined to be 48^{+3}_{-2} mb^{-1} and 214^{+14}_{-11} mb^{-1}, respectively, using the cross section for triggering on at least one neutron in the ZDC detectors. The cross section for triggering on at least one neutron on the ZDC was measured in a van der Meer scan [37] and found to be $371.4 \pm 0.6(\text{stat.})^{+24}_{-19}(\text{syst.})$ b [30].

In order to correct for trigger and detector inefficiencies, the STARLIGHT MC generator was used [10]. In addition, MC simulations with flat distributions in invariant-mass, pair transverse momentum, and in pair rapidity were used, see section 1.4. This has the advantage that MC sampling in invariant mass is uniform and therefore statistical fluctuations at the tails of the distribution are avoided. Using the flat MC simulation is justified because (1) at mid-rapidity the distribution in rapidity is approximately flat, and (2) acceptance$\times$efficiency is approximately flat in p_T for small pair p_T.

3.1.2 Event selection and analysis cuts

Figure 3.1 shows an event display of an ultra-peripheral ρ^0 candidate event, consisting of two oppositely charged tracks in an otherwise empty detector. Besides the trigger selection the following cuts were applied

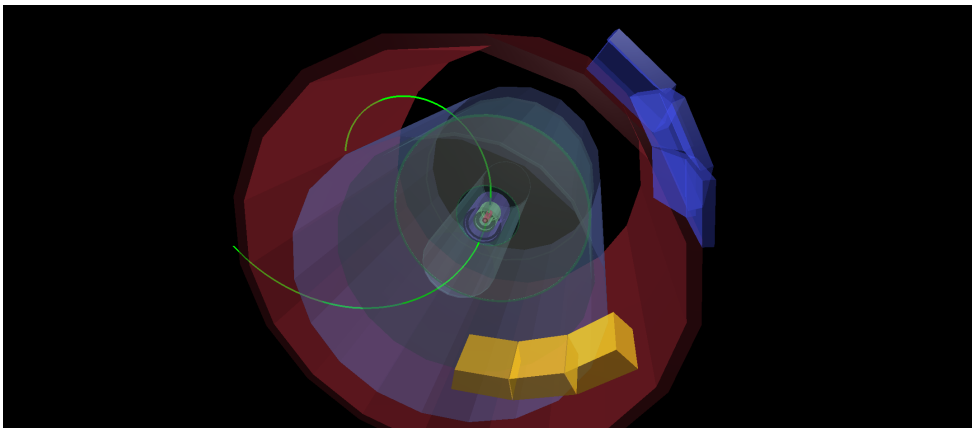

Fig. 3.1: Event display of a typical ultra-peripheral ρ^0 candidate event showing two oppositely charged tracks in an otherwise empty detector.

- The VZERO-A and VZERO-C detectors were required to be empty.
- A primary vertex within $\pm$ 10 cm of the interaction point along the beam direction was required
- Exactly two tracks were required having at least 70 (out of a maximum of 159) space points in the TPC with Kalman filter $\chi^2 < 4$, and having at least one hit in SPD with ITS Kalman filter $\chi^2 < 36$ (this is a fiducial cut). In addition the distance of closest approach (DCA) to the vertex of each track was limited to $\mathrm{DCA}_z < 2$ cm and $\mathrm{DCA}_{xy} < 0.0182 + 0.035 p_T^{-1.01}$ with the transverse momentum p_T in units of GeV/c [21].
- Pion PID using TPC $\mathrm{d}E/\mathrm{d}x$ for both tracks was performed using the deviation from the Bethe-Block parametrization of the energy loss of pions in the TPC in terms of number of sigmas: $\Delta\sigma^2_{\pi^+} + \Delta\sigma^2_{\pi^-} < 16$, see fig. 3.2 where the circle shows the used selection and the entries in the upper right part of this figure are due $\mathrm{e}^+\mathrm{e}^-$ pair production via two-photon interactions.

In order to select mostly coherently produced ρ^0 mesons, pion pair $p_T < 150$ MeV/c was required, and to avoid edge effects, the pion pair rapidity was restricted to $|y| < 0.5$. For the signal, events with opposite-sign pairs of tracks were used, *i.e.*, $\pi^+\pi^-$, and like-sign pair events, $\pi^+\pi^+$ and $\pi^-\pi^-$, were subtracted. The fraction of like-sign events was found to be 2%.

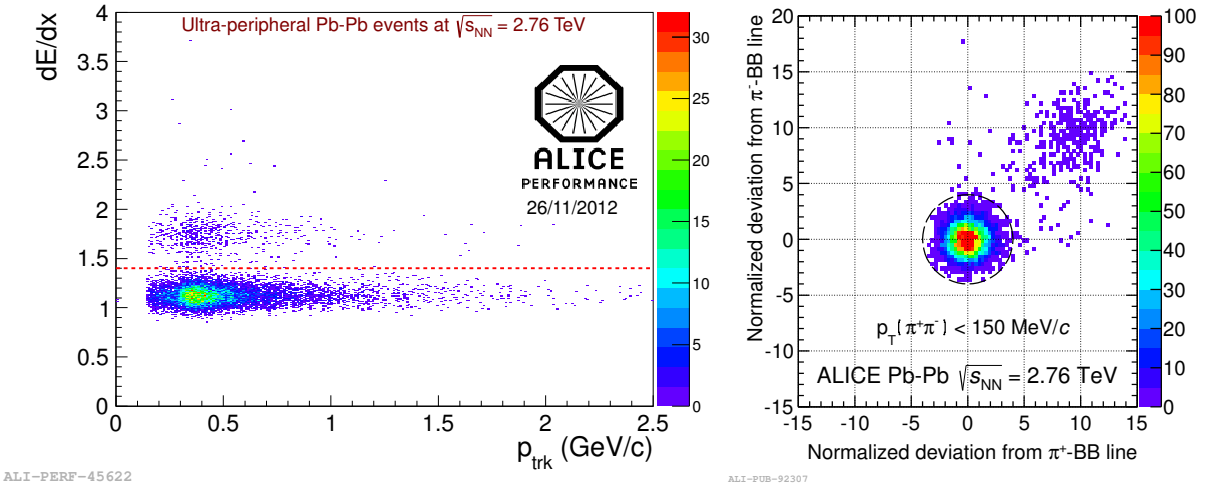

Fig. 3.2: Identification of $\pi^{\pm}$ using TPC dE/dx. Left: TPC dE/dx vs. track momentum; Right: normalized deviations (number of σs) from the pion Bethe-Bloch parametrization for π^- vs. π^+. In both cases pions are clearly separated from electrons. For the analysis, the cut indicated in the figure on the right-hand side is used.

3.1.3 Extraction of the coherent photoproduction cross section

The signal extraction proceeds in two steps, 1) fitting the invariant-mass distribution corrected for efficiency and acceptance, and 2) subtraction of the contribution of incoherent ρ^0 production using the pion pair p_T distribution.

Fits to the invariant-mass spectrum One parametrization of the ρ^0 invariant-mass distribution at two-pion rapidity $y = 0$ is due to Söding [38] and consists of the sum of two *amplitudes*:

$$\frac{\mathrm{d}\sigma^{\text{Soeding}}}{\mathrm{d}m_{\pi\pi}} = \left| A \cdot BW\left(m_{\pi\pi}; m_{\rho^0}, \Gamma(m_{\pi\pi})\right) + B \right|^2 , \tag{3.1}$$

where A denotes the strength of a relativistic Breit-Wigner amplitude,

$$BW\left(m_{\pi\pi}; m_{\rho^0}, \Gamma(m_{\pi\pi})\right) = \frac{\sqrt{m_{\pi\pi} m_{\rho^0} \Gamma(m_{\pi\pi})}}{m_{\pi\pi}^2 - m_{\rho^0}^2 + i m_{\rho^0} \Gamma(m_{\pi\pi})} , \tag{3.2}$$

having a mass-dependent width

$$\Gamma(m_{\pi\pi}) = \Gamma_{\rho^0} \frac{m_{\rho^0}}{m_{\pi\pi}} \left(\frac{m_{\pi\pi}^2 - 4m_\pi^2}{m_{\rho^0}^2 - 4m_\pi^2} \right)^{3/2} . \tag{3.3}$$

The constant amplitude B describes non-resonant pion-pair production. While in reality the non-resonant pion-pair production is not constant, it is a good approximation in the kinematic range for which this formula is being used which is from the threshold at $2m_\pi$ to $M_{\rho^0} + 5\Gamma_{\rho^0}$.

The fit of Equation (3.1) to the data results in

$$\begin{aligned} M_{\rho^0} &= 761.6 \pm 2.3(\text{stat.}) + 6.1(\text{syst.})\text{MeV}/c^2 \,, \\ \Gamma_{\rho^0} &= 150.2 \pm 5.5(\text{stat.})^{+12.0}_{-5.0}(\text{syst.})\text{MeV}/c^2 \,, \\ |B/A| &= 0.50 \pm 0.04(\text{stat.})^{+0.10}_{-0.04}(\text{syst.})\left(\text{GeV}/c^2\right)^{-1/2} \,, \end{aligned}$$

where the systematic errors were were obtained by varying the track selection, fitting method and fit ranges. The mass and the width of ρ^0 are consistent with the values reported by the PDG [35], however the ratio of the non-resonant to the resonant amplitude, $|B/A|$, is lower compared to the earlier measurement by STAR [36, 39, 40] in Au collisions, where values $|B/A| = 0.81$ – 0.89 $\left(\text{GeV}/c^2\right)^{-1/2}$ for $\langle W_{\gamma N}\rangle$ in the range 7 – 12 GeV [36, 39, 40] were measured. One explanation for the lower value of $|B/A|$ observed by ALICE is, see [32], that is may indicate that the non-resonant contribution is more strongly absorbed in heavy nuclei at high energies, as had been previously suggested [41].

Another parametrization, due to Ross and Stodolsky [42] is

$$\frac{\mathrm{d}\sigma^{\mathrm{RS}}}{\mathrm{d}m_{\pi\pi}} = f \cdot BW\left(m_{\pi\pi}; m_{\rho^0}, \Gamma(m_{\pi\pi})\right)\left(\frac{m_{\rho^0}}{m_{\pi\pi}}\right)^k \tag{3.4}$$

using either the mass-dependent width from Equation (3.3), or

$$\tilde{\Gamma}(m_{\pi\pi}) = \Gamma_{\rho^0}\left(\frac{m^2_{\pi\pi} - 4m^2_\pi}{m^2_{\rho^0} - 4m^2_\pi}\right)^{3/2} \,, \tag{3.5}$$

i.e.

$$\frac{\mathrm{d}\sigma^{\mathrm{RS}'}}{\mathrm{d}m_{\pi\pi}} = f \cdot BW\left(m_{\pi\pi}; m_{\rho^0}, \tilde{\Gamma}(m_{\pi\pi})\right)\left(\frac{m_{\rho^0}}{m_{\pi\pi}}\right)^k \,. \tag{3.6}$$

The fit of Equation (3.6) to the data results in

$$\begin{aligned} M_{\rho^0} &= 769.2 \,\pm\, 2.8(\text{stat.})\,{}^{+8.0}_{-5.2}(\text{syst.})\ \text{MeV}/c^2 \,, \\ \Gamma_{\rho^0} &= 156.9 \,\pm\, 6.1(\text{stat.})^{+17.3}_{-5.9}(\text{syst.})\ \text{MeV}/c^2 \,, \\ k &= 4.7 \,\pm\, 0.2(\text{stat.})^{+0.8}_{-0.6}(\text{syst.}) \,, \end{aligned}$$

where as before the systematic errors were were obtained by varying the track selection, fitting method and fit ranges.

Also in this case the mass and width of ρ^0 obtained from the fit are in agreement with the values reported by the PDG. The parameter k, which parametrizes the deviation from a pure Breit-Wigner shape, can be compared to measurements on proton targets at HERA: ZEUS mea-

sured $k = 5.13 \pm 0.13$ averaged over all momentum transfers [43] and $k \approx 6$ for $t = 0$, while H1 reported $k = 6.84 \pm 1.00$, averaged over all momentum transfers [44]. The fact that k is smaller for Pb targets than for proton targets indicates that the invariant-mass distribution for Pb-targets deviates less from a pure Breit-Wigner resonance. Note that this is consistent with the fit parameters obtained using the Söding formula.

The yield is extracted from the resonant part of Equation (3.1), *i.e.*, setting $B = 0$ and integrating between the threshold, $2m_\pi$, and $M_{\rho^0} + 5\Gamma_{\rho^0}$. These integration limits were used in order to be compatible with earlier measurements at HERA and by the STAR experiment at RHIC. In addition, they are justified by the range of validity of the description of the invariant-mass spectrum by the Söding formula (3.1).

Figures 3.3 and 3.4 show two-pion invariant-mass spectra corrected for efficiency×acceptance, together with fits, using linear and logarithmic y-axes, respectively.

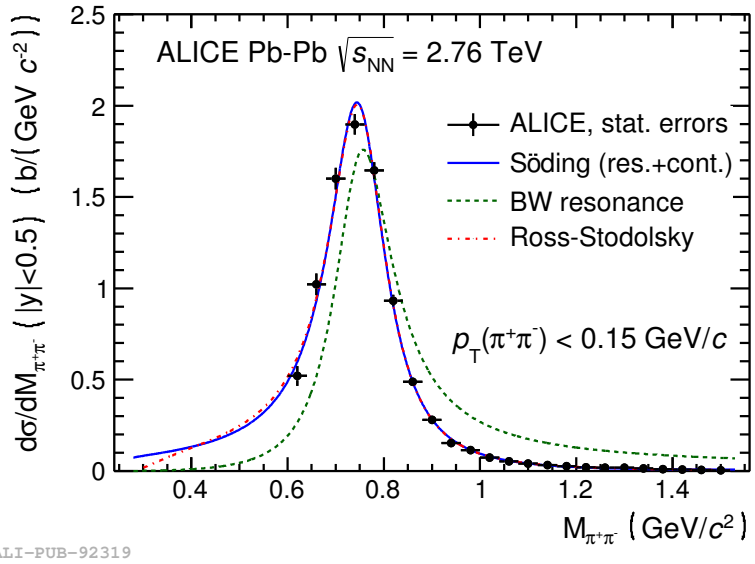

Fig. 3.3: Pion pair invariant-mass distribution corrected for efficiency and acceptance, together with fits of a Söding and a Ross-Stodolsky parametrization The resonant part of the Söding parametrization which is used for extracting the ρ^0 the yield is shown separately.

Subtraction of the incoherent ρ^0 production The cut on pair transverse momentum ensures that *mostly* coherently produced ρ^0s are selected. However there is a small contamination by incoherent UPC ρ^0 production. Therefore, in a second step, this contamination is estimated using the pion-pair transverse momentum spectrum.

The incoherent contribution to events with $p_T < 0.15$ GeV/c was determined in two different ways:

1. by fitting the sum of two exponential functions in p_T^2 to the p_T histogram and integrating

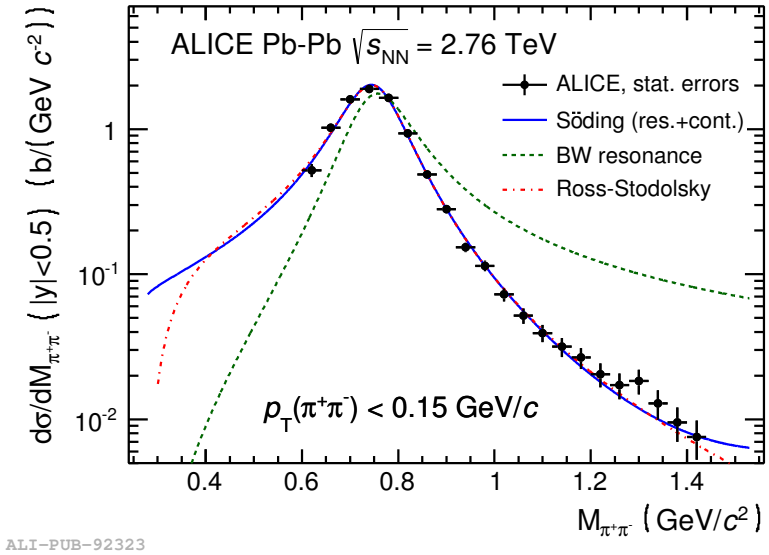

Fig. 3.4: Pion pair invariant-mass distribution corrected for efficiency and acceptance, like in Fig. 3.3 but with a logarithmic y-axis. There is a small bump near the f_2 mass indicating two-photon production of the f_2 meson.

them over the interval $[0, 0.15]$ GeV/c, and

2. by using STARLIGHT-generated templates fitted to the p_T distribution, see Fig. 3.5. For this, p_T-templates for coherent and incoherent ρ^0 production are obtained from a STARLIGHT MC simulation and then fitted to the two-pion transverse-momentum distribution obtained from data.

In both cases the relative number of incoherent events with $p_T < 0.15$ GeV/c is 5.1%.

The two-pion transverse-momentum distribution shows a clear peak at $p_T < 150$ MeV/c, consistent with coherent photoproduction, and a high-p_T tail which is very well described by STARLIGHT.

However, the coherent peak in data is slightly shifted towards lower two-pion transverse momenta in data compared to the STARLIGHT prediction. This has been observed before at lower collision energies by STAR [45]. The two-pion transverse momentum distribution is related to the Fourier transform of the nuclear profile function which can be modeled by a Wood-Saxon function (1.7). In fact, STAR has obtained the nuclear profile function by a one-dimensional Fourier transform from the diffraction pattern, see Figures 3.6.

The form factor of the nuclear profile function used in STARLIGHT is obtained from elastic electron-nucleus scattering data which probes the nuclear *charge* density only, while the ρ^0 couples both to protons and to neutrons. However the current limit on the difference of the neutron and proton radii of ^{208}Pb, called "neutron skin", of 0.3 fm [46] does not fully account

for the difference between the STARLIGHT prediction and the data.

The coherent peak in the two-pion transverse-momentum distribution can be parametrized as an exponential distribution with slope b,

$$\frac{\mathrm{d}N}{\mathrm{d}t} \propto \exp\left(-bt\right), \tag{3.7}$$

where $t = -p_T^2$. Note that the slope b is expected to be proportional to the square of the nuclear radius, R^2. ALICE has measured this slope and found $b = 428 \pm 6(\text{stat.}) \pm 15(\text{syst.})$ GeV$^2/c^2$. In order to avoid interference effects at very low t, the region below $|t| < 0.002$ GeV$^2/c^2$ was excluded from the fit of equation (3.7) to the data. We have verified that acceptance$\times$efficiency is flat for small p_T. Therefore the systematic error on the slope b was obtained from the difference between STARLIGHT generated events at generator level and after passing through the full detector simulation.

The corresponding measurement of the the slope b by STAR in Au-Au collisions is reported in [36] where $b = 388 \pm 24$ GeV$^2/c^2$ was found. The slopes found in ALICE and in STAR are compatible within errors if one takes into account the different sizes of Au and Pb nuclei from which an increase in b by $\approx$4-8% in Pb w.r.t. Au is expected.

Table 3.1 summarizes the systematc error taken into account for the cross section for the SPD+TOF+VZERO triggered sample:

- The integrated luminosity was deterimined using the cross section for triggering on at least one neutron in the ZDC, see [30] from where its systematic error was taken.
- The systematic error on the trigger efficiency is obtained by comparing the trigger efficiency in MC simulation with the trigger efficiency obtained from a data sample triggerd by ZDC only, see [47]. In addition there is a correction for TOF trigger dead time due to late particles whose systematic uncertainty was estimated to be $\pm$1.3%.
- The systematic error on the normalized yield N_{yield} is obtained by varying the fit method (χ^2 vs. log likeligood fitting) and fit ranges
- In order to determine the systematic error on track selection, three other track selections have been used in addition to the default track selection described above: accepting tracks reconstructed only in the ITS in addition to global ITS-TPC tracks, using only tracks recontructed in the TPC, and using the default track selection with a stronger requirement on the TPC.
- The contamination with continuum $\gamma\gamma \to \mu^+\mu^-$ was treated as an systematic errror. It was estimated to be 5% using two different methods: STARLIGHT simulation and measuring the number of $\gamma\gamma \to e^+e^-$ events.

– The systematic uncertainty of the relative number of incoherent events was determined to be $\pm 0.7\%$ by using different track selections.

– Events with one or more additional SPD tracklets were rejected. The relative number of rejected events in MC was taken as the systematic error for this cut.

– The data sample taken with a TOF only trigger allows to estimate relative number of coherent events cut by the VZERO veto which is found to be 10%. The systematic error is determined from the estimated hadronic contamination, *i.e.*, from events which have a signal in the ZDCs.

Table 3.1: Summary of the systematic error in the cross section calculationfor the SPD+TOF+VZERO trigger sample.

Variable	Systematic error
Luminosity	$^{+6.5}_{-5.1}$ %
Trigger efficiency	$^{+3.8}_{-9.0}$ %
Trigger dead time correction	$\pm 1.3\%$
Signal extraction	$^{+0.8}_{-1.4}$ %
Track selection	$^{+3.7}_{-3.0}$ %
Particle ID	$^{+0.0}_{-5.0}$ %
Incoherent contribution	$\pm 0.7\%$
SPD tracklets	$\pm 0.5\%$
VZERO offline selection	$^{+0.0}_{-3.1}$ %
Total	$^{+9.2}_{-11.2}$ %

The total systematic error for the combined TOF-only and SPD+TOF+VZERO-triggered sample is obtained using the method described in [48], carefuylly disentangling correlated and uncorrelated errors.

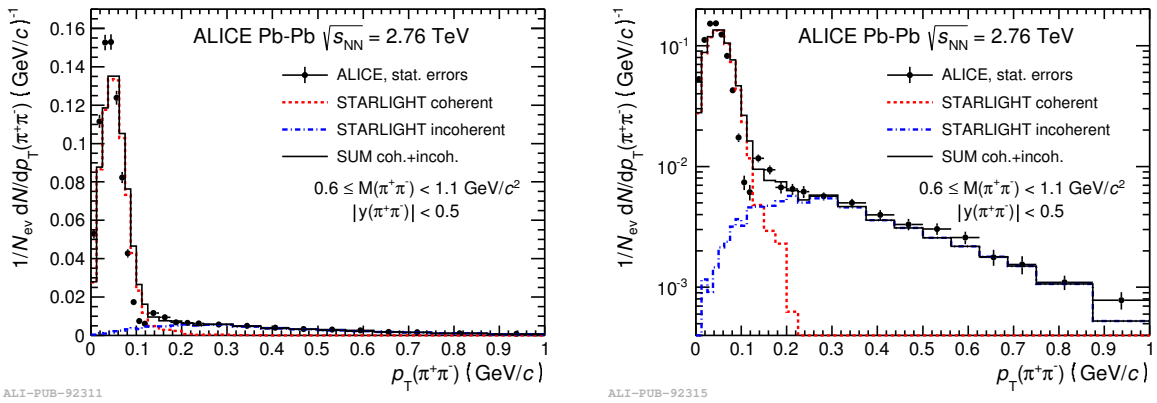

Fig. 3.5: The two-pion transverse momentum spectra with a fit of STARLIGHT generated templates for coherent and incoherent ρ^0 production. Left: linear y-axis, right: logarithmic y-axis.

The number of ρ^0s obtained from the fit to the invariant-mass spectrum is corrected for

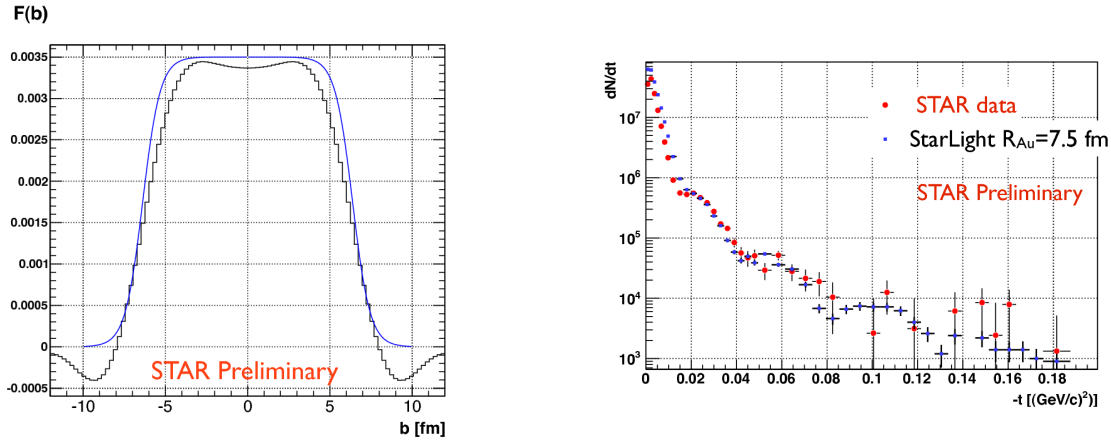

Fig. 3.6: Left: the one-dimensional Fourier transformation of the measured diffraction pattern shown a a black histogram. The Wood-Saxon functional form with $R = 6.38$ fm and $a_0 = 0.535$ fm is shown with a blue curve [45]. Right: the unnormalized distribution for the $-t$ value of ρ mesons generated with Starlight is shown with blue markers to compare them with the same distribution extracted from data.

- incoherent events with $p_T < 0.15$ GeV/c (f_{incoh})
- events which have one or more additional SPD tracklet (f_{SPD})
- number of coherent ρ^0 events lost by the VZERO veto (f_{VZERO})

in the following way:

$$N_\rho^{\text{coh}} = \frac{N_{\text{yield}}}{1 + f_{\text{incoh}} + f_{\text{SPD}} + f_{\text{VZERO}}} , \tag{3.8}$$

with $f_{\text{incoh}} = 0.051 \pm 0.007$, $f_{\text{SPD}} = 0.030 \pm 0.005$, and $f_{\text{VZERO}} = -0.100^{+0.031}_{-0.000}$.

Using the corrected coherent yield, the integrated luminisity and the used rapidity interval, the differential (in rapidity) cross section at mid-rapitity is obtained as follows

$$\frac{\mathrm{d}\sigma}{\mathrm{d}y} = \frac{N_\rho^{\text{coh}}}{L_{\text{int}} \cdot \Delta y} . \tag{3.9}$$

Combining the two data samples, the cross section for coherent ρ^0 photoproduction was found to be

$$\left|\frac{\mathrm{d}\sigma}{\mathrm{d}y}\right|_{y=0} = 425 \pm 10(\text{stat.})^{+42}_{-50}(\text{sys.})\ \text{mb} . \tag{3.10}$$

Figure 3.7 shows a comparison of the measured cross section with model predictions. The measured cross section is in agreement with STARLIGHT [9, 10] and the calculation by Goncalves and Machado (GM) [49] while the GDL (Glauber-Donnachie-Landshoff) prediction [50, 51] is about a factor of two above the data. For a more recent calculation of the cross section of ρ^0 photoproduction, which appeared after the ALICE measurement was published, see [52]. In this more recent calculation, the includsion of nucleon shadowing in the calculation improves

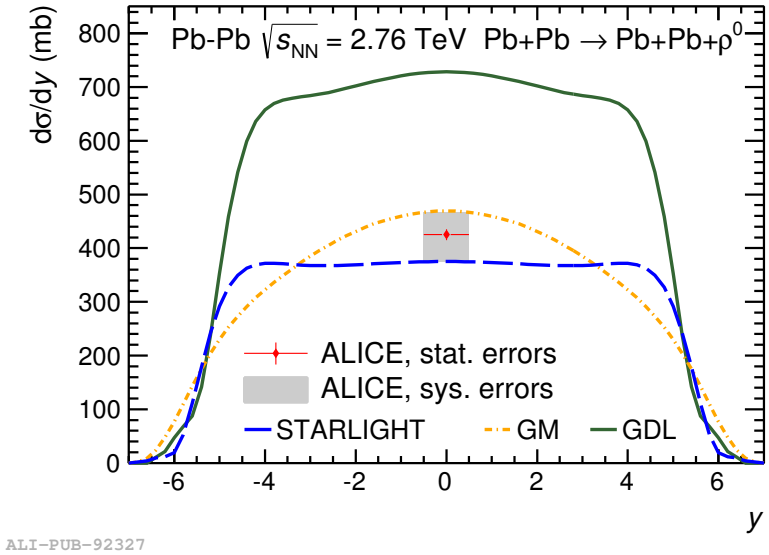

Fig. 3.7: Comparison of the measured coherent UPC ρ^0 cross section at mid-rapidity with model predictions.

the agreement with data.

3.1.4 *Extrapolation from mid-rapidity to the total photoproduction cross section*

The cross section measured at mid-rapidity, $|y(\pi^+\pi^-)| < 0.5$, can be extrapolated to the total cross section by extrapolation. For this extrapolation to the total cross section, both STARLIGHT and the GDL model were used. The deviation of these two ways of extrapolation from their mean is about 8% and was added to the systematic error. In this way the total cross section for coherent ρ^0 photoproduction was obtained to be

$$\sigma\left(\mathrm{Pb}+\mathrm{Pb}\to\mathrm{Pb}+\mathrm{Pb}+\rho^0\right) = 4.2\pm0.1(\mathrm{stat.})^{+0.5}_{-0.6}(\mathrm{sys.})\ \mathrm{b} \quad \text{at } \sqrt{s_{\mathrm{NN}}} = 2.76\ \mathrm{TeV}\,. \tag{3.11}$$

The total cross section is shown in figure 3.8 as a function of $\sqrt{s_{\mathrm{NN}}}$ where STAR measurements at different $\sqrt{s_{\mathrm{NN}}}$ in Au-Au collisions and the ALICE measurement in PbPb collisions are compared to STARLIGHT and GDL predictions.

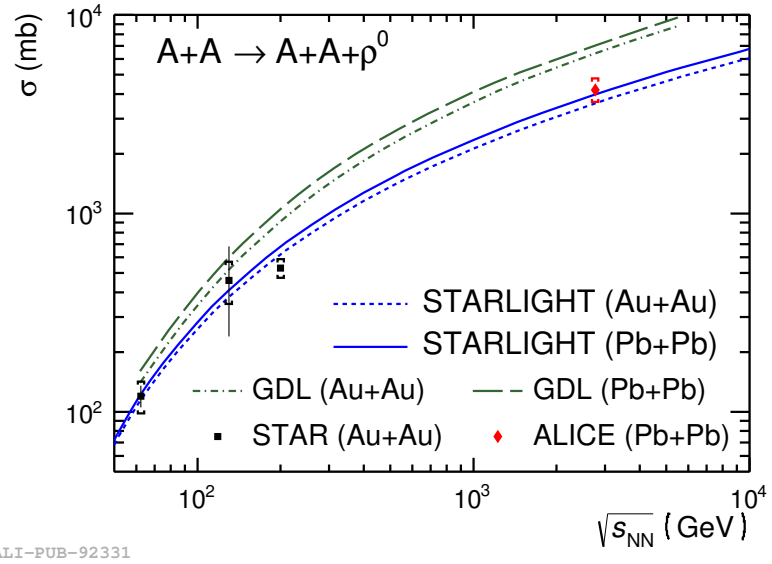

Fig. 3.8: Comparison of the total coherent UPC ρ^0 cross section (*i.e.*, extrapolated to full rapidity) with model predictions, together with earlier measurements by STAR in Au-Au collisions.

3.1.5 *Nuclear breakup in coincidence with ρ^0 photo-production*

The ACLIE zero-degree calorimeters (ZDC) have an excellent detection probability of 99% for neutrons with $|\eta| > 8.8$ [30]. Figure 3.9 shows the neutron spectrum in the ZDC for the events selected for this analysis. Peaks corresponding to 0,1, and several neutrons are clearly separated. The fit shown in this figure consists of a sum of Gaussian function, where the mean of the nN Gaussian is n times the mean of the 1N Gaussian and the width of the nN Gaussian is $\sqrt{n}$ times the width of the 1N Gaussian.

Three Different classes of events are considered using the ZDC neutron distributions:

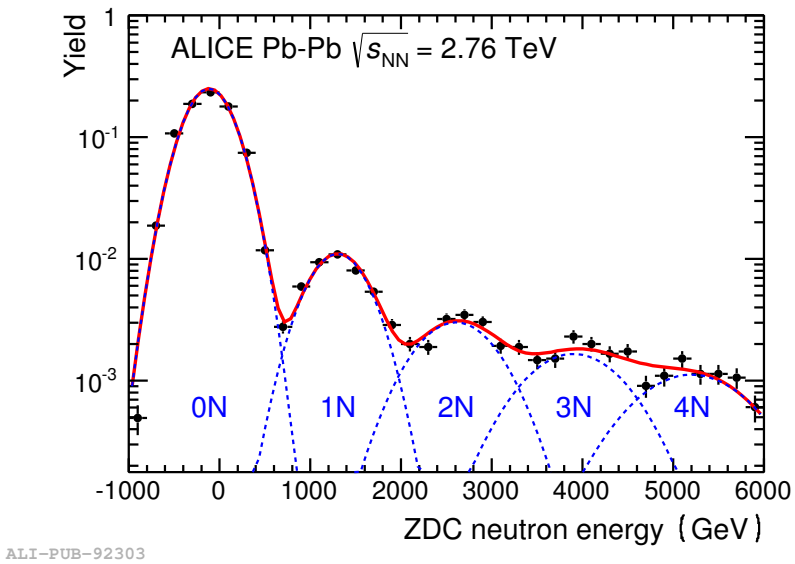

Fig. 3.9: Energy deposit in the Zero-Degree Calorimeters. The curves correspond to Gaussian fits for 0, 1, 2, 3, or 4 neutrons entering the calorimeter.

- 0N: no neutron in the ZDC, i.e, calorimeter energy less than 600 GeV
- 1N: exaclty one neutron in the ZDC, *i.e.*, calorimeter energy between 600 GeV and 2000 GeV, and
- XN: one or more neutron in the ZDC, *i.e.*, calorimeter energy above 2000 GeV.

As there are two ZDCs, one on each side of the interaction point, out of these three classes of events for a single ZDC the following combinations were considered:

- 0N0N: no neutron detected in any ZDC,
- XN: at least one neutron detected in any ZDC,
- 0NXN: no neutron detected in one ZDC and at least one neutron detected in the other ZDC,
- XNXN: at least one neutron detected in both ZDCs.

Note that some of the fractions shown in table 3.2 are correlated, *i.e.*, the fractions for 0N0N for XN should add up to 100%; likewise the sum of 0NXN and of XNXN should be equal to XN. Because the fraction of incoherent events was estimated and subtracted independently for each case the correlated fraction add up to 100% only within statistical errors. The fraction shown in table 3.2 are consistent with STARLIGHT and GDL predictions within three standard deviations.

Table 3.2: The number of events that satisfy various selections on the number of neutrons detected in the ZDCs. 0N0N corresponds to no neutrons emitted in any direction; XN to at least one neutron emitted in any direction; 0NXN to no neutrons in one direction and at least one neutron in the other direction; XNXN to at least one neutron in both directions.

Selection	Number of events	Fraction	STATLIGHT	GDL
All events	7293	100 %		
0N0N	6175	$87.4 \pm 0.4(\text{stat.})^{+0.4}_{-1.9}(\text{sys.})$ %	79 %	80 %
XN	1174	$16.1 \pm 0.4(\text{stat.})^{+2.2}_{-0.5}(\text{sys.})$ %	21 %	20 %
0NXN	958	$13.1 \pm 0.4(\text{stat.})^{+0.9}_{-0.3}(\text{sys.})$ %	16 %	15 %
XNXN	231	$3.2 \pm 0.2(\text{stat.})^{+0.4}_{-0.1}(\text{sys.})$ %	5.2 %	4.5 %

3.2 ρ^0 photoproduction in Pb-Pb collisions at $\sqrt{s_{NN}} = 5.02$ TeV

The cross section for coherent ρ^0 photoproduction in ultra-peripheral collisions of lead ions has also been measured in LHC run 2 at a higher collision energy [53].

The trigger for ultra-peripheral events used in this analyis consists of vetoes on VZERO and on AD and of a topological requirement in SPD. This topological SPD trigger requires a 4-fold coincidence in SPD with a back-to-back topology, see figure 2.3. The event selection is as follows

- require exactly two good tracks
- pair-$p_T < 0.2$ GeV/c
- pair-rapidity $\left|y(\pi^+\pi^-)\right| < 0.5$

The resulting acceptance×efficiency w.r.t. two-pion invariant mass for the trigger and event selection is shown in figure 3.10 right.

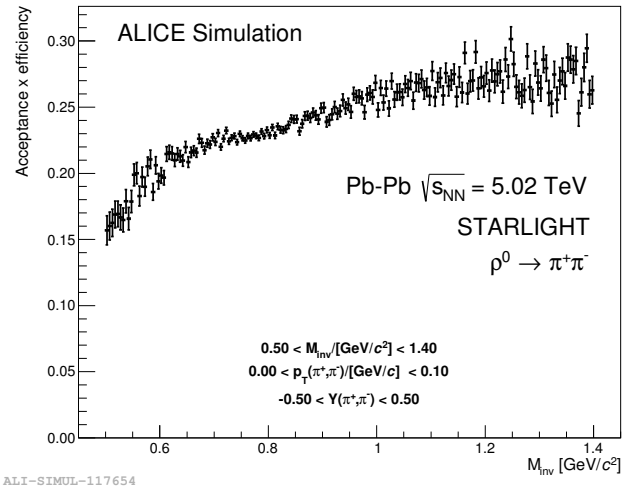

Fig. 3.10: Acceptance×efficiency w.r.t. two-pion invariant-mass [53].

A correction for the shadowing of ultra-peripheral events by the used vetoes was applied: when

there are soft electromagnetic dissociaion processes in coincides within the timing windows of the veto detectors proper ultra-peripheral events are shadowed by the veotes, *i.e.*, lost because there is no ultra-peripheral trigger. This effect was estimated by using an unbiased trigger, observing the strength of veto shadowing as a function of interaction rate, and then applying a correction to the observed ρ^0 yield.

The invariant-mass spectrum is corrected for acceptance×efficiency and then the sum of three amplitudes is fitted to it, see figure 3.11: a relativistic Breit-Wigner amplitude, $BW(\rho^0)$, see equation (3.2), for ρ^0, a constant amplitude, B, describing non-resonant pion pair production, and an additional Breit-Wigner amplitude, $BW(\omega)$, describing the process $\omega \to \pi^+\pi^-$:

$$\frac{\mathrm{d}\sigma}{\mathrm{d}m_{\pi\pi}} = \left|A \cdot BW(\rho^0) + B + Ce^{i\alpha} \cdot BW(\omega)\right|^2 + N \cdot \mathrm{pol6}\,. \tag{3.12}$$

The background from continuum $\gamma\gamma \to \mu^+\mu^-$ production is fixed to a STARLIGHT MC template, and any remaining backgrounds are modelled by a polynomial of degree 6.

The mass of the omega (ω) meson is 782.65 ± 0.12 MeV/c^2 and its branching ratio into two pions is $1.53^{+0.11}_{-0.13}\%$ [35]. Although this branching ratio is small, the available statistics in the LHC run 2 data sample is sufficient for detecting the interference between ρ^0 and ω in the invariant mass spectrum as a kink around the ω mass. In the fit, the mass and width of ρ^0 are

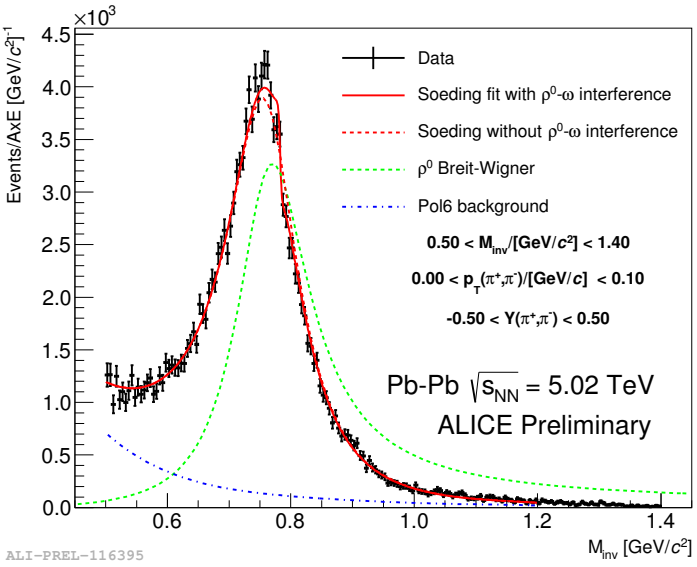

Fig. 3.11: Two-pion invariant-mass spectrum, corrected for acceptance×efficiency, together with a fit of the sum of three amplitudes to the data, see equation (3.12) [53].

fixed to their known values which were taken from [35], and as before the yield is obtained by integrating the resonant part for ρ^0 in equation (3.12), *i.e.*, setting B, C,and N to zero, in the interval $\left[2m_\pi, M_{\rho^0} + 5\Gamma_{\rho^0}\right]$.

In the two-pion transverse momentum spectrum, shown in figure 3.12, the first and the second

diffractive peak can be clearly seen. As for the run 1 analyis, the shape of the coherent peak is more narrow in data as in the STARLIGHT MC simulation. While in the run 1 analyis the contamination with continuum $\gamma\gamma \to \mu^+\mu^-$ was treated as a systematic error, here it is subtracted using a template generated by STARLIGHT.

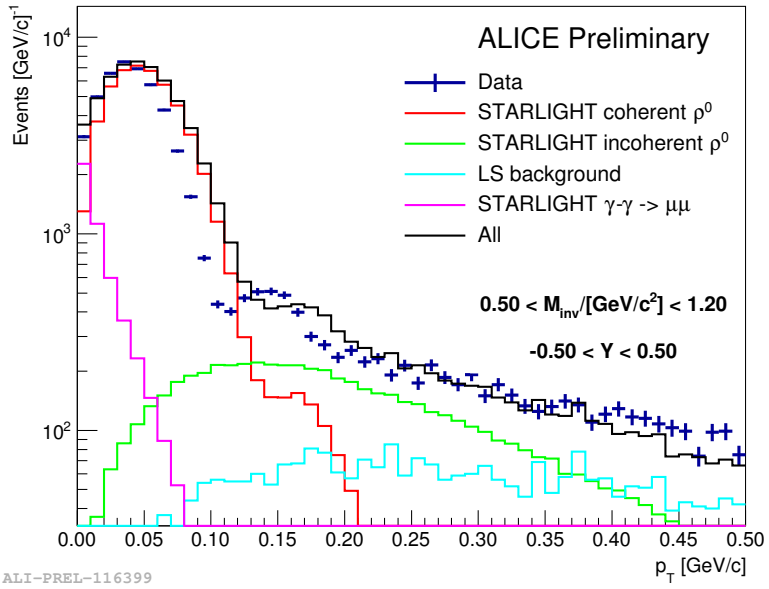

Fig. 3.12: Shown is the Two-pion transverse momentum distribution, together with templates for coherent and incoherent ρ^0 production and for continuum $\gamma\gamma \to \mu + \mu^-$ production, all generated by STARLIGHT. The fitted template for incoherent ρ^0 production is used to subtract the constribution of incoherent ρ^0 production below $p_T < 0.2$ GeV/c, [53].

As a result, the following cross section for coherent ρ^0 photoproduction in Pb-Pb collision at $\sqrt{s_{\mathrm{NN}}} = 5.02$ TeV at mid-rapidity is obtained

$$\left.\frac{\mathrm{d}\sigma}{\mathrm{d}y}\right|_{y=0} = 448 \pm 2(\mathrm{stat.})^{+38}_{-75}(\mathrm{syst.})\ \mathrm{mb}\ . \tag{3.13}$$

Figure 3.13 compares this measurement with a number of model predictions: STARLIGHT [10], a Color Dipole Model (CDM) [54, 55], and a prediction due to Guzey, Kryshen, and Zhalov (GKZ) [56]. The STARLIGHT prediction is compatible with the measurement within 1σ, while all other models shown in Figure 3.13 over-estimate the measured cross section.

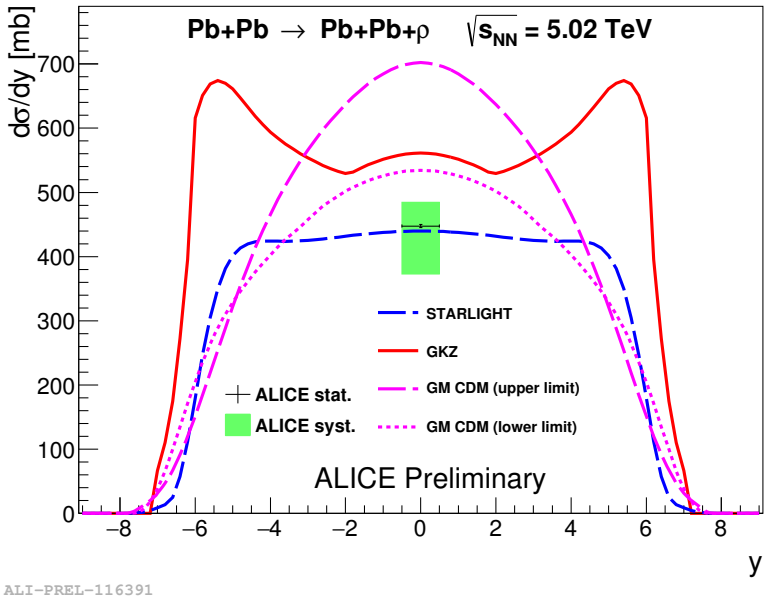

Fig. 3.13: Comparison of the measured cross section at mid-rapidity with model predictions: STARLIGHT [10], CDM [54, 55], and GKZ [56].

4 $\gamma\gamma$ processes in Pb-Pb collisions at $\sqrt{s_{NN}} = 2.76$ TeV

4.1 Low-mass continuum dielectron photoproduction

For the two data samples used for tho ρ^0 analysis described in section 3, ALICE also has measured the cross section for continuum $\gamma\gamma \to e^+e^-$ photoproduction [32]. For this measurement, events with e^+e^- pairs in the kinematic range $0.6 \leq M\left(e^+e^-\right) \leq 2.0$ GeV/c^2, and $\left|\eta(\pi^+)\right| < 0.9$ and $\left|\eta(\pi^-)\right| < 0.9$ were used, and the cuts for particle identification were modified to select dielectron events; otherwise the same cuts as for the ρ^0 analysis were applied.

The corrections for trigger efficiencies and for detector acceptance were obtained using STARLIGHT events processed through the full ALICE detector simulation. As a result, the following cross section for continuum $\gamma\gamma \to e^+e^-$ photoproduction was measured

$$\sigma\left(0.6 \leq M\left(e^+e^-\right) \leq 2.0\,\mathrm{GeV}/c^2, \left|\eta(e^\pm)\right| < 0.9\right) = 9.8 \pm 0.6(\mathrm{stat.})^{+0.9}_{-1.2}(\mathrm{syst.})\,\mathrm{mb}\,. \quad (4.1)$$

This measurement is compatible with the prediction by STARLIGHT which for the same kinematic range given $\sigma = 9.7$ mb. As a check it was verified that the cross sections obtained for the two used data samples, TOF-only triggered, and SPD+TOF+VZERO-triggered, are compatible.

4.2 High-mass continuum dielectron photoproduction

In LHC run 1 there were two periods with Pb-Pb collisions: one in the end of 2010 and one in the end of 2011. The analyses described so far, *i.e.*, coherent ρ^0 photoproduction and $\gamma\gamma \to e^+e^-$ photoproduction at e^+e^- invariant masses below 2 GeV/c^2, are based on data taken in 2010.

For the Pb-Pb run in 2011 the ultra-peripheral trigger in ALICE was modified in order to trigger on higher invariant-mass two-track events such as $J/\psi \to e^+e^-$ and high-mass dielectron photoproduction. This was achieved by modifying the trigger condition in TOF: while before the TOF trigger requirement was that ≥ 2 TOF maxi-pads are active, for this analysis a topological trigger condition in TOF was used.

This topological TOF trigger, see section 2.3, requires that between between 2 and 6 TOF maxi-pads are fired and that the opening angle of at least one pair of fired TOF maxi-pads exceeds 150°. As a consequence the invariant-mass of two-track final states is biased towards higher invariant-masses above about 2 GeV/c^2.

The measurement of two-photon photoproduction of electron pairs described below is published in [47]. The trigger for ultra-peripheral events consisted of the following three requirements: (1) at least two hits in the SPD detector; (2) the TOF topological trigger described above and in section 2.3, a veto on VZERO-A and on VZERO-C. About 6.5×10^6 events were selected by this trigger, corresponding to an integrated luminosity of $L_{\text{int}} = 21.7^{+0.7}_{-1.1}\mu\text{b}^{-1}$.

The integrated luminosity was determined in two ways: in a van der Meer scan [37] where $\sigma = 4.10^{+0.22}_{-0.13}$(sys) b was found [57]. An alternative method based on using neutrons detected in the two ZDCs was also used, see section 3.1.1 and [30]. The difference between these two methods is about 3% which is consistent within one signal of the errors quoted above.

For this analysis the following cuts were applied, quoting [47]:

- a number of reconstructed tracks $1 \leq N_{\text{TRK}} \leq 10$, where a track is defined with loose criteria: more than 50% of findable clusters in the TPC fiducial volume and at least 20 TPC clusters, matching with those found in the ITS;
- a reconstructed primary vertex;
- only two good tracks passing tighter quality cuts: at least 70 TPC clusters, at least 1 SPD cluster and rejection of tracks with a kink. Moreover the tracks extrapolated to the reconstructed vertex should have a distance of closest approach (DCA) in the longitudinal beam direction $\text{DCA}_{\text{L}} \leq 2$ cm, and $\text{DCA}_{\text{T}} \leq 0.0182 + 0.0350/p_T^1.01$ cm in the plane orthogonal to the beam direction, where p_T is in units of (GeV/c);
- at least one of the two good tracks selected with the tight track selection with $p_T \geq 1$ GeV/c; this cut reduces the background while it does not affect the genuine leptons from J/ψ decay and from two-photon e^+e^- photoproduction;
- the VZERO trigger required no signal within a time window of 25 ns around the collision time in any of the scintillator tiles of both VZERO-A and VZERO-C. The time width of the trigger windows are limited by the design of the VZERO front-end electronics which is operated at the frequency of the LHC clock, *i.e.*, 40 MHz. In the offline analysis the

event selection criteria consisted in an absence of a reconstructed signal in any of the VZERO scintillator tiles. The time windows in the offline analysis are enlarged to 40 ns and 60 ns around the collision time in VZERO-A and VZERO-C, respectively, and were chosen in order to maximize the vetoing efficiency;

– the $\mathrm{d}E/\mathrm{d}x$ for the two tracks is compatible with that of electrons or muons; Figure 4.1 shows the TPC $\mathrm{d}E/\mathrm{d}x$ of the positive lepton candidate as a function of the dE/dx of the negative lepton candidate, for J/ψ candidates in the invariant mass range between 2.8 and 3.2 GeV/c^2. It is worth noting that the TPC PID resolution does not allow to distinguish between muons and charged pions;

– the two tracks have same or opposite charges, depending on the analysis

– invariant mass either between 2.2 and 2.6 GeV/c^2 or between 3.7 and 10 GeV/c^2, excluding the J/ψ and $\Psi(2S)$ resonances.

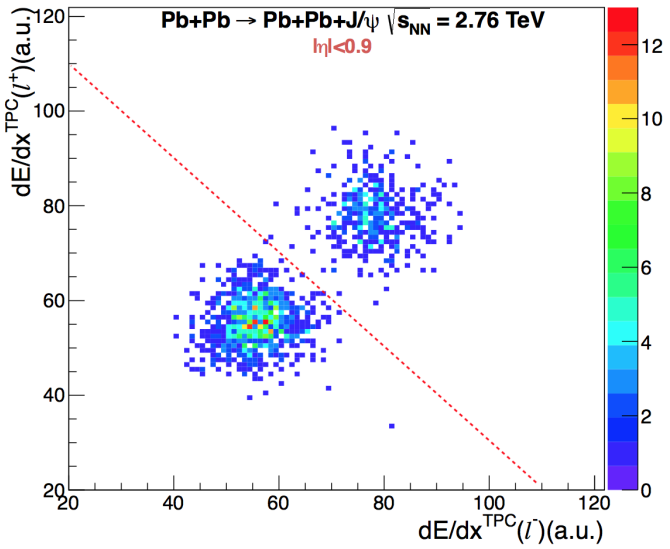

Fig. 4.1: $\mathrm{d}E/\mathrm{d}x$ of the positive lepton versus the negative one, as measured by the TPC for J/ψ candidates in the ultra-peripheral Pb-Pb collisions at $\sqrt{s_{\mathrm{NN}}} = 2.76$ TeV in the invariant mass range $2.8 < M < 3.2$ GeV/c^2 $-0.9 < \eta < +0.9$ [47]. Muon pairs and electron pairs are clearly separated, with the latter showing higher $\mathrm{d}E/\mathrm{d}x$ values.

The systematic errors are summarized in table 4.1, and include systematic errors for the integrated luminosity, trigger dead time, signal extraction, trigger efficiency, acceptance×efficiency, and electron particle identification.

The cross section for $\gamma\gamma \to e^+e^-$ can be obtained as follows

$$\sigma\left(\gamma\gamma \to e^+e^-\right) = \frac{N_{\gamma\gamma}}{\left(\mathrm{Acc} \times \mathrm{Eff}\right) \cdot L_{\mathrm{int}}} \,. \tag{4.2}$$

Table 4.1: Summary of the contributions to the systematic error of the $\gamma\gamma$ cross section measurement.

Source	$\gamma\gamma$ (low)	$\gamma\gamma$ (high)
Luminosity	$^{+5}_{-3}\%$	$^{+5}_{-3}\%$
Trigger dead time	$\pm 2.5\%$	$\pm 2.5\%$
Signal extraction	$\pm 1\%$	$\pm 4\%$
Trigger efficiency	$^{+3.9}_{-9.0}\%$	$^{+3.9}_{-9.0}\%$
Acc$\times$Eff	$\pm 0.3\%$	$\pm 0.3\%$
e/μ separation	$\pm 1.7\%$	$\pm 4.0\%$

For the low dielectron invariant mass region $186 \pm 13(\text{stat.}) \pm 4(\text{sys.})$ dielectron events were found, and the product of acceptance and efficiency was estimated to be 5.6%. Thus the measured cross section is for this case

$$\sigma\left(2.2 \leq M\left(e^+e^-\right) \leq 2.6\,\text{GeV}/c^2, \left|\eta(e^\pm)\right| < 0.9\right) = 154 \pm 11(\text{stat.})^{+17}_{-11}(\text{syst.})\,\mu\text{b}\,. \quad (4.3)$$

For the high dielectron invariant mass interval $93 \pm 10(\text{stat.}) \pm 4(\text{sys.})$ dielectron events were found, and the product of acceptance and efficiency was determined to be 4.73%. This results in the following cross section measurement,

$$\sigma\left(3.7 \leq M\left(e^+e^-\right) \leq 10.0\,\text{GeV}/c^2, \left|\eta(e^\pm)\right| < 0.9\right) = 91 \pm 10(\text{stat.})^{+10}_{-8}(\text{syst.})\,\mu\text{b}\,. \quad (4.4)$$

No like-sign events were found in both cases.

The cross section measurements in (4.3), (4.4) are to be compared with predictions by STARLIGHT of $\sigma = 128\mu$b, and $\sigma = 77\mu$b, respectively. While both measured cross sections are about 20% above the prediction by STARLIGHT, both are fully compatible with the predictions within 1.0 and 1.5 sigma, respectively.

Figure 4.2 shows the measured $\gamma\gamma \to e^+e^-$ cross section w.r.t. dielectron invariant mass, together with the prediction by STARLIGHT for both considered invariant mass ranges. Likewise, figure 4.3 shows dielectron pair-p_T distributions, along with STARLIGHT predictions. Note that the broadening of the transverse momentum distributions with increasing dielectron invariant mass is correctly described by STARLIGHT.

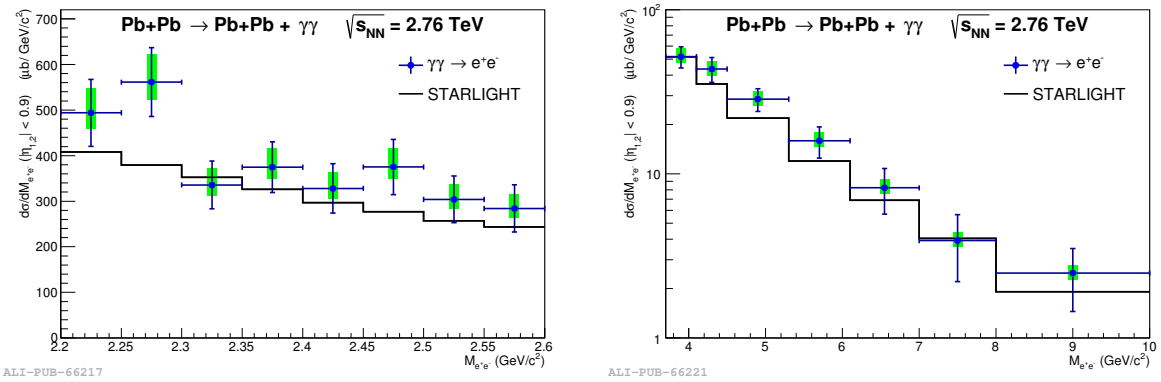

Fig. 4.2: ALICE measurement of coherent $\gamma\gamma \to e^+e^-$ photoproduction in e^+e^- invariant-mass ranges below (left) and above (right) the J/ψ and $\Psi(2S)$ resonances, compared to STARLIGHT [47].

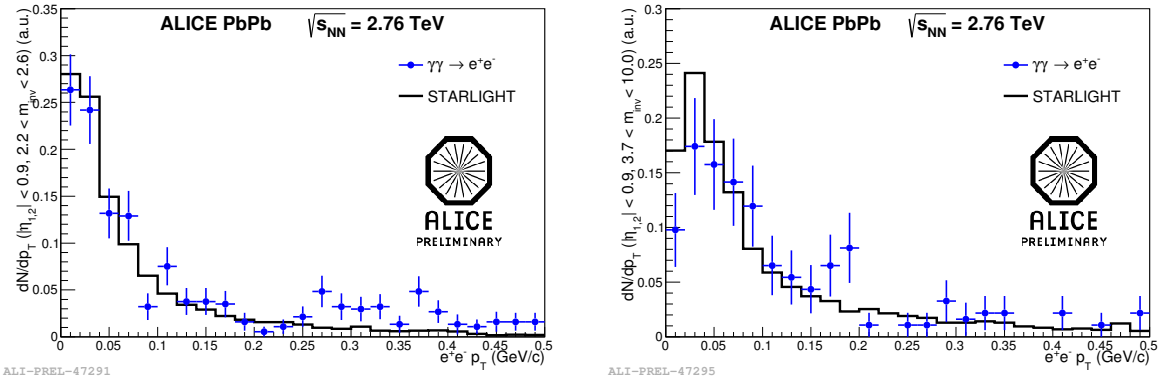

Fig. 4.3: e^+e^- pair-p_T distributions for $\gamma\gamma \to e^+e^-$ photoproduction in e^+e^- invariant-mass ranges below (left) and above (right) the J/ψ and $\Psi(2S)$ resonances, compared to STARLIGHT [47]. Note that the broadening of the pair-p_T distribution with increasing e^+e^- invariant-masses is correctly described by STARLIGHT.

4.3 Low- and high-mass continuum dielectron photoproduction

Figure 4.4 summarizes the ALICE measurements of $\gamma\gamma \to e^+e^-$ cross sections at $\sqrt{s_{\rm NN}} = 2.76$ TeV. The range in dielectron invariant mass is from 0.6 to 10 GeV/c^2, excluding the region around the J/ψ and $\Psi(2S)$ resonances. It would be very interesting to repeat this analysis for Pb-Pb data taken at $\sqrt{s_{\rm NN}} = 5.02$ TeV.

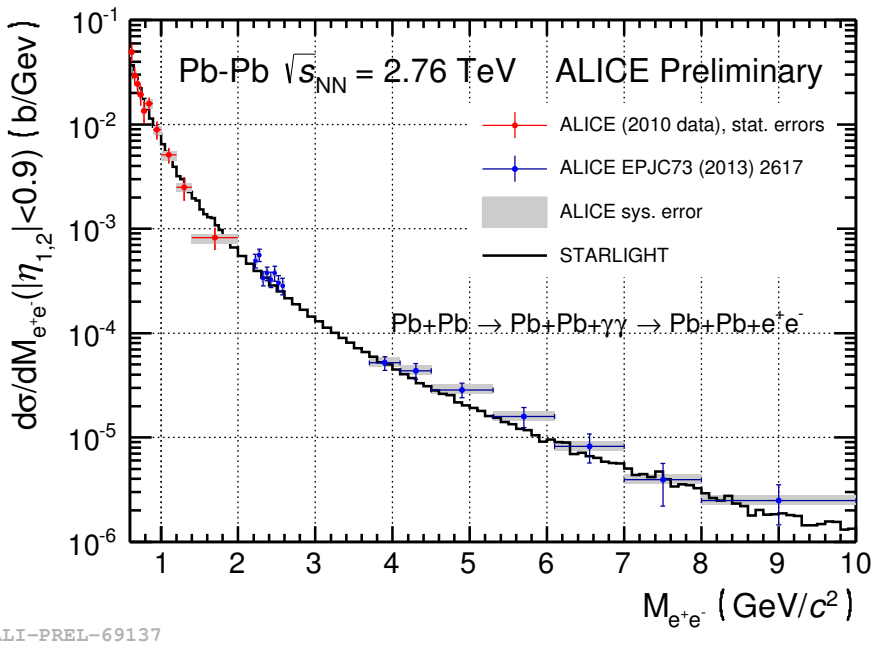

Fig. 4.4: ALICE measurement of coherent $\gamma\gamma \to e^+e^-$ photoproduction in the e^+e^- invariant-mass range from 0.6-10 GeV/c^2 compared to STARLIGHT.

5 High-mass vector meson production

In this section, ALICE measurements of J/ψ photoproduction in ultra-peripheral Pb-Pb collisions at $\sqrt{s_{\rm NN}} = 2.76$ TeV and in p-Pb collisions at $\sqrt{s_{\rm NN}} = 5.02$ TeV are summarized.

5.1 J/ψ photoproduction in Pb-Pb collisions at $\sqrt{s_{\rm NN}} = 2.76$ TeV

ALICE has measured J/ψ photoproduction in Pb-Pb collisions at $\sqrt{s_{\rm NN}} = 2.76$ TeV, at forward rapidities using the muon forward spectrometer [58], and in the central barrel [47]. The first measurement was performed in the forward rapidity region $-3.6 < y < -2.6$ and allows us to constrain the nuclear gluon distribution at Bjorken-$x \approx 10^{-2}$, while the measurement at mid-rapidity probes the region $x = M_{\rm J/\psi}/\sqrt{s_{\rm NN}}e^{\pm y} \approx 10^{-3}$. In the following, we focus on the measurement in the central barrel.

The ultra-peripheral trigger and the event and track selection used in this analysis are the same as for the high-mass $\gamma\gamma \to e^+e^-$ photoproduction measurement described in section 4.2. In addition to the cuts in section 4.2, a cut on pair-$p_T < 200$ MeV/c was used. In the following we call data samples with this additional cut "coherent enriched". The integrated luminosity for the used data sample is $L_{\rm int} = 23.0^{+0.7}_{-1.2}\,\mu{\rm b}^{-1}$.

Combining electron and muon pairs, figure 5.1 shows the invariant mass distribution for $2.2 < M < 6.0$ GeV/c^2 for opposite-sign (OS) and like-sign (LS) pairs. The J/ψ resonance is clearly visible as a peak on top of a continuum due to $\gamma\gamma$ continuum production of dilepton pairs.

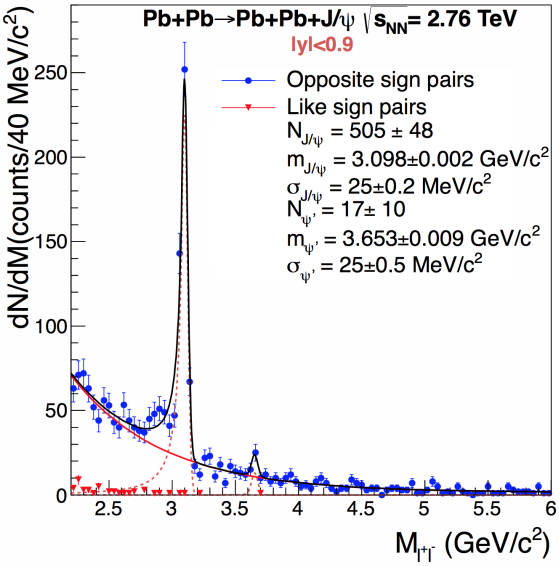

Fig. 5.1: Invariant mass distribution for ultra-peripheral Pb-Pb collisions at $\sqrt{s_{\rm NN}} = 2.76$ TeV and $-0.9 < y < 0.9$ for events satisfying the event selection described in section 4.2, in the invariant mass interval $2.2 < M < 6$ GeV/c^2 [47]. Coherent dielectron and dimuon candidates are summed together.

Using STARLIGHT generated J/ψ events passed through the full ALICE detector simulation, acceptance×efficiency was determined. Small variations in detector performance during the data taking period were taken into account by computing the luminosity-weighted average. The average values for the combined acceptance and efficiency for J/$\psi \to e^+e^-(\mu^+\mu^-)$ were found to be 2.71% (4.57%). The trigger efficiency obtained from MC was measured using a data sample collected in a dedicated run triggered by the ZDCs only, by replaying the ultra-peripheral trigger condition offline.

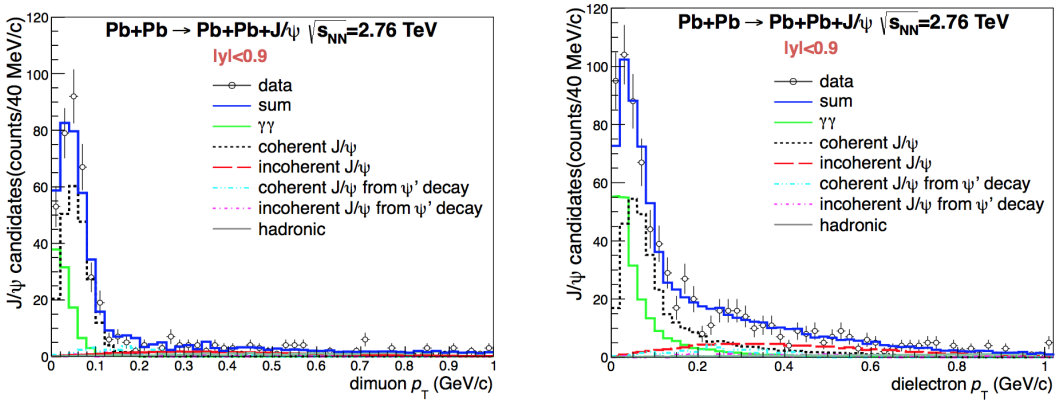

Fig. 5.2: Di-muon (left) and dielectron (right) p_T distribution for ultra-peripheral Pb-Pb collisions at $\sqrt{s_{\rm NN}} = 2.76$ TeV at $-0.9 < y < 0.9$ for for events satisfying the event selection in the invariant mass interval $3.0 < M < 3.2$ GeV/c^2 and $2.2 < M < 3.2$ GeV/c^2 respectively [47]. The data points are fitted summing six different Monte Carlo templates: coherent J/ψ production (black), incoherent J/ψ production (red), J/ψs from coherent $\Psi(2S)$ decay (light blue), J/ψs from incoherent $\Psi(2S)$ decay (violet), $\gamma\gamma$ (green), and J/ψ produced in peripheral hadronic collisions (gray). The solid histogram (blue) is the sum.

The yield of coherently producted J/ψs was determined by fitting the pair-p_T distributions for the e^+e^- and $\mu^+\mu^-$ final states to a number of templates, see figure 5.2:

- coherent J/ψ photoproduction;
- incoherent J/ψ photoproduction;
- J/ψ from coherent $\Psi(2S)$ decay;
- J/ψ from incoherent $\Psi(2S)$ decay;
- two-photon production of continuum pairs ($\gamma\gamma$):
- J/ψ produced in peripheral hadronic collisions.

The first five of these templates were obtained from STARLIGHT MC simulations, while the template for J/ψs produced in peripheral hadronic collisions was obtained from [59]. For the correction to the yield for feed-down from $\Psi(2S)$ decaying into J/ψs we refer to [47].

As a result we obtain $\mathrm{d}^{\mathrm{coh}}_{\mathrm{J}/\psi}/\mathrm{d}y = 2.27 \pm 0.14(\mathrm{stat.})^{+0.30}_{-0.20}(\mathrm{syst.})$ mb for the dimuon channel and $\mathrm{d}^{\mathrm{coh}}_{\mathrm{J}/\psi}/\mathrm{d}y = 3.19 \pm 0.50(\mathrm{stat.})^{+0.45}_{-0.31}(\mathrm{syst.})$ mb for the dielectron channel. The weighted average of the dimuon and the dielectron cross sections, shown in figure 5.3, is

$$\left.\frac{\mathrm{d}^{\mathrm{coh}}_{\mathrm{J}/\psi}}{\mathrm{d}y}\right|_{y=0} = 2.38^{+0.34}_{-0.24}(\mathrm{stat.} + \mathrm{syst.})\ \mathrm{mb}. \tag{5.1}$$

The measured cross section is compared to six different models, RSZ-LTA [51] based on the leading twist approximation, STARLIGHT [9, 10], AB [60] using a number of different parametrization of the nuclear wave function, GM [49], CSS [61], and LM-fIPSAT [62].

The model AB-MSTW08 does not include nuclear effects and over-estimates the measurement. The models STARLIGHT, GM, CSS and LM use a Glauber approach to calculate the number of nucleons contributing to the scattering, and there are partonic models, where the cross section is proportional to the nuclear gluon distribution squared (AB-EPS08, AB-EPS09, AB-HKN07, and RSZ-LTA).

The measured coherent J/ψ cross section at mid-rapidity is found to be in good agreement with the model AB-EPS09, which takes into account nuclear gluon shadowing according to the EPS09 parametrization. Those models which include no nuclear gluon shadowing are inconsistent with the measured results, as are those which use the Glauber model to incorporate nuclear effects.

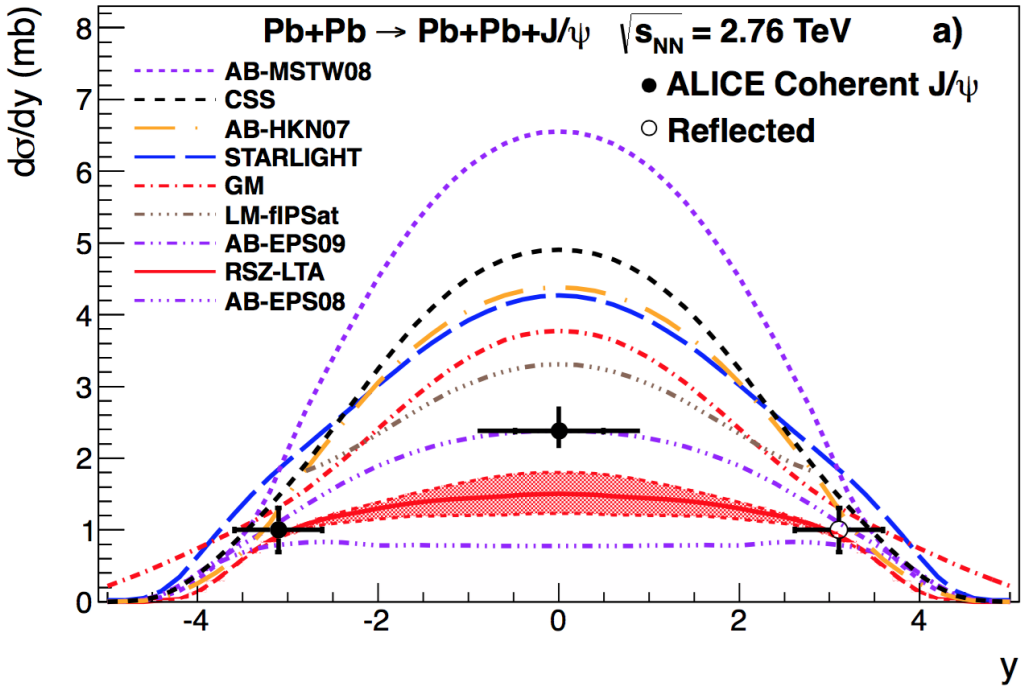

Fig. 5.3: Measured differential cross section of coherent J/ψ photoproduction in ultra-peripheral Pb-Pb collisions at $\sqrt{s_{\rm NN}} = 2.76$ TeV and at $-0.9 < y < 0.9$ [47]. The error is the quadratic sum of the statistical and systematic errors. For the ALICE measurement at forward rapidities see [58].

5.2 J/ψ photoproduction in p-Pb collisions at $\sqrt{s_{\rm NN}} = 5.02$ TeV

ALICE has measured for the first time exclusive J/ψ photoproduction off protons in ultra-peripheral proton-lead collisions at the LHC at $\sqrt{s_{\rm NN}} = 5.02$ TeV [63, 64].

A typical event displays of a J/$\psi \to \mu^+\mu^-$ candidate event in an ultra-peripheral collision detected in the forward muon spectrometer is shown in figure 5.4.

In proton-lead collision, exclusive J/ψ production off protons is enhanced w.r.t. production off lead ions because the equivalent photon flux around the lead ions is much larger than around protons [13, 14].

The LHC provided proton-lead collisions in two collision modes, *i.e.*, with two directions for the proton beam. For the case in which both muons from the J/ψ decay are measured in the muon forward spectrometer [63], these two modes correspond to $2.5 < y < 4.0$ (p-Pb), called forward, and $-3.6 < y < -2.6$ (Pb-p), called backward, in terms of J/ψ rapidities y measured in the laboratory frame. The equivalent γp energy ranges are $21 < W_{\gamma p} < 45$ GeV for $y < 0$, and $577 < W_{\gamma p} < 952$ GeV for $y > 0$, which exceeds the energy range of previous measurements at HERA, see figure 1.4.

Another way in which exclusive J/ψ photoproduction off protons in ultra-peripheral proton-

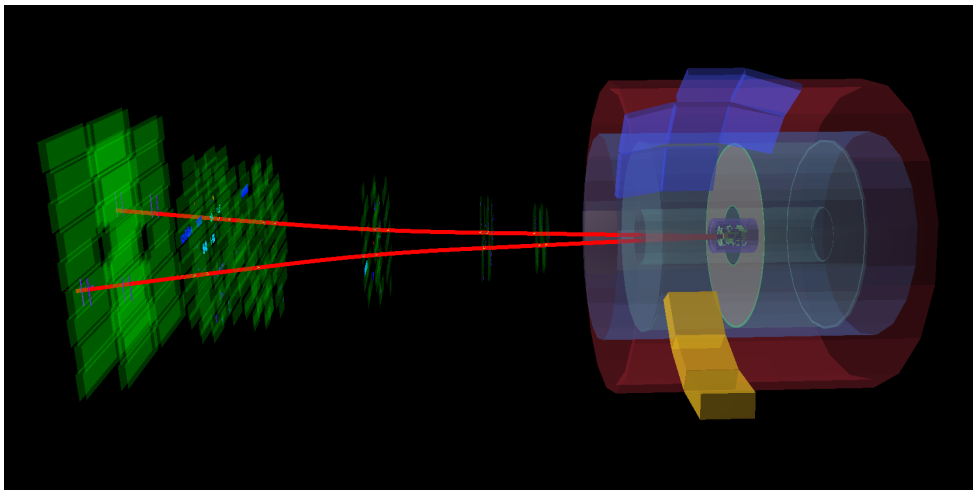

Fig. 5.4: Event display of an ultra-peripheral J/$\psi \to \mu^+\mu^-$ candidate event measured in the forward muon spectrometer.

lead collisions can be measured in ALICE is by analyzing events in which one muon is detected in the muon forward spectrometer and the other muon is detected in the central barrel [64]. For both directions of the beams the corresponding J/ψ rapidity ranges are $-2.5 < y < -1.2$, called semi-backward, and $1.2 < y < 2.7$, called semi-forward, and correspond to equivalent γp energy ranges of $41 < W_{\gamma p} < 87$ GeV for $y > 0$ and $287 < W_{\gamma p} < 550$ GeV for $y < 0$.

Finally, exclusive J/ψ photoproduction can be measured in the central barrel alone [64], *i.e.*, $|y| < 0.8$ corresponding to an equivalent γp energy range of $106 < W_{\gamma p} < 235$ GeV. In this case, both e^+e^- and $\mu^+\mu^-$ final states are available thanks to the PID capabilities of the ALICE TPC.

The trigger for the measurement at forward rapidities required two oppositely charged tracks in the muon spectrometer and a veto on VZERO-A beam-beam interactions. In the p-Pb configuration beam-induced backgrounds were suppressed by requiring in addition at least one hit in VZERO-C and adding a veto on the VZERO-A beam-gas trigger. The integrated luminosity for both configurations is $L = 3.9$ nb$^{-1} \pm 3.7\%$ (syst.) for p–Pb and $L = 4.5$ nb$^{-1} \pm 3.4\%$ (syst.) for Pb–p data.

For the semi-forward measurement the trigger required one muon in the forward muon spectrometer, at most 4 cells active in VZERO-C, a veto on VZERO-A and at least one fast-or chip active in either inner or outer layer of SPD and at most 7 fast-or chips active in the outer layer of SPD. For the Pb-p data taking period, additional requirements on VZERO were added to the trigger In order to reduce beam-induced backgrounds [64]. The integrated luminosity is 3.1 nb^{-1} for the p-Pb period and 3.7 nb^{-1} for the Pb-p period.

The trigger for the measurement at mid-rapidity required a veto in both, VZERO-C and in VZERO-A, and a topological trigger requirements both on TOF and on SPD selecting back-

to-back activity patterns. The integrated luminosity for the central rapidity data samples is 2.1 nb^{-1} in p-Pb and 4.8 nb^{-1} in Pb-p. In order to increase the size of the central rapidity data sample the p–Pb and Pb–p data samples have been analyzed together, taking into account the inversion of the rapidity sign.

Figure 5.5 shows dimuon invariant mass spectra after event and track selection [64]. The J/ψ peak is clearly visible in both data sets, and is well described by a Crystal Ball parametrization [65], which yields masses and widths in agreement with the Monte Carlo simulations. The dimuon continuum is well-described by an exponential as expected from two-photon production of continuum pairs.

The dimuon pair-p_T distributions shown in figure 5.5 have clear peaks at low pair-p_T corresponding to coherent photoproduction. In order to extract the number of *exclusive* J/ψ candidates, the pair-p_T distribution have been fitted to a number of templates, including exclusive J/ψ production, $\gamma\gamma \to \mu^+\mu^-$, $\gamma + Pb$ and non-exclusive background, where the p_T shapes for the J/ψ in γp, $\gamma\gamma \to \mu^+\mu^-$, and coherent J/$\psi$ in γPb components were obtained using STARLIGHT [10]. The templates for non-exclusive J/ψ candidates were obtained from data by requiring events to have more than two hits in the VZERO-C counters and the same event selection as before.

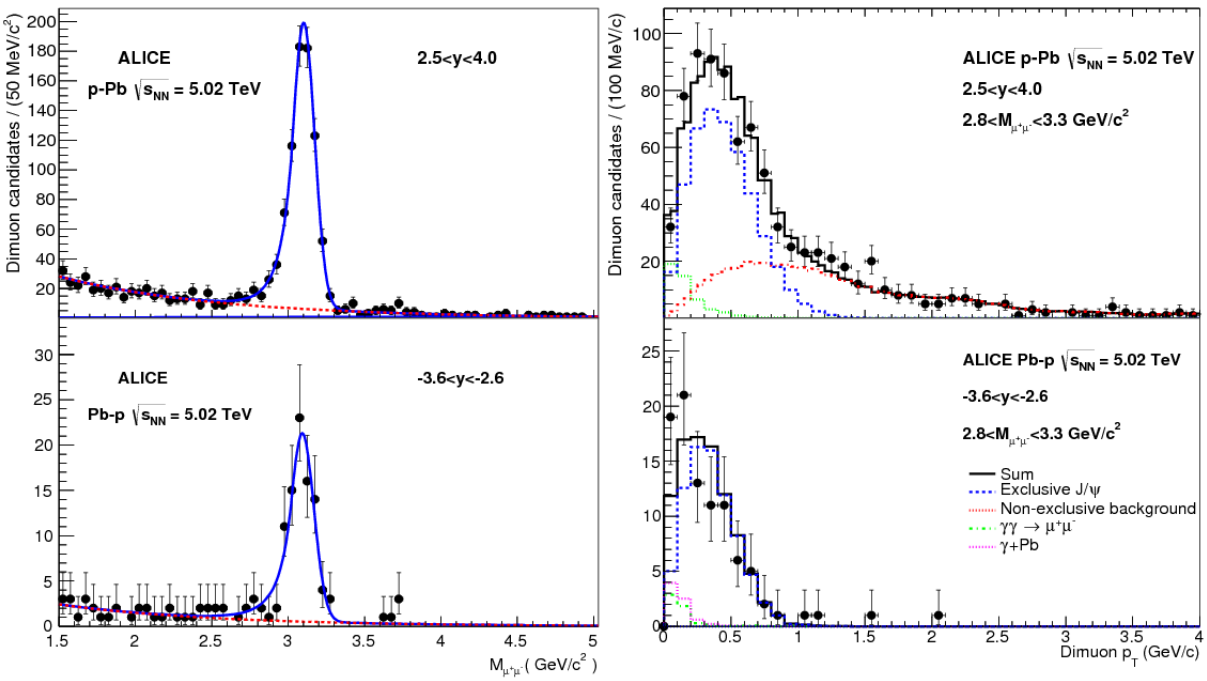

Fig. 5.5: Left: Invariant mass distribution for events with two oppositely charged muons, for both forward (top panel) and backward (bottom panel) dimuon rapidity samples; Right: Transverse momentum distribution for events with two oppositely charged muons, for both forward (top panel) and backward (bottom panel) dimuon rapidity samples [63].

For the semi-forward and central analysis, the invariant mass spectra for the event and track

selections in [64] are shown in figure 5.6. As for the forward analysis the J/ψ peak, which is clearly visible in all considered data data sets, is well described by a Crystal Ball parametrization [65], and yields masses and widths in agreement with the Monte Carlo simulations. The dimuon continuum is described by an exponential function, as expected from two-photon production of continuum pairs.

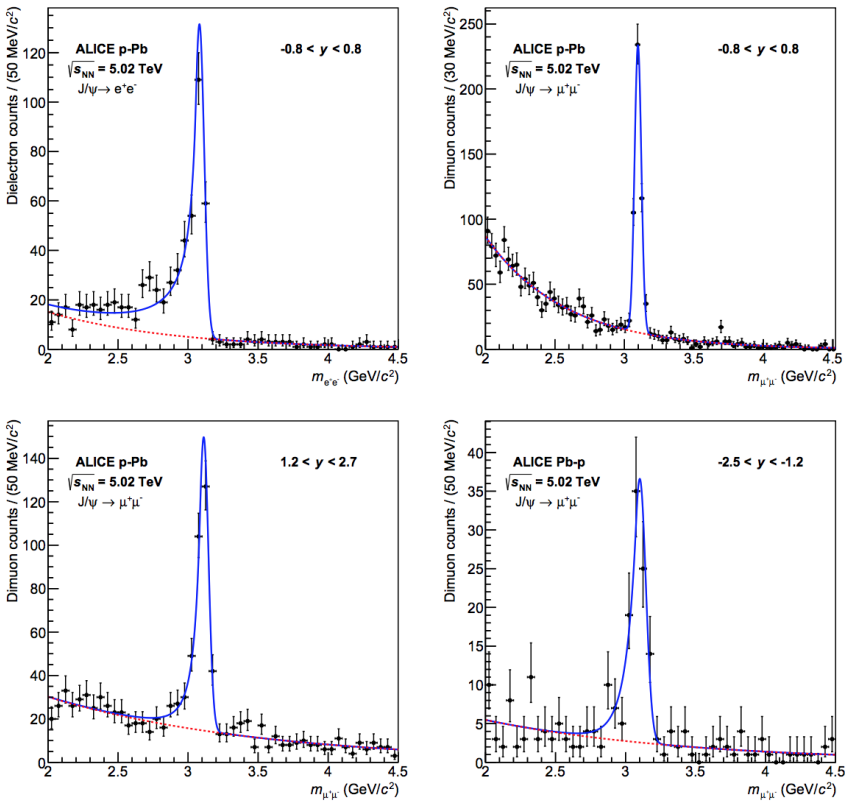

Fig. 5.6: Mass distributions of selected dileptons for the dielectron (upper left) and dimuon (upper right) samples for the central analysis and dimuon samples for the semi-forward (lower left) and semi-backward (lower right) analyses. In all cases the data are represented by points with error bars. The solid blue line is a fit to a Crystal-Ball function plus an exponential distribution, where this last contribution is shown by a dotted red line [64].

Like for the forward analysis, a number of templates were fitted to the pair-p_T spectra for the central and semi-forward data samples shown in figure 5.7. These templates were obtained from STARLIGHT generated events passed through the full detector simulation, except the templates for non-exclusive J/ψ production which werefg obtained from data.

Having extracted the number of exclusive J/ψ candidates from the pair-p_T template fits, a correction for feed-down from form $\Psi(2S)$ was applied, following the procedure described in [47, 58]

$$N_{J/\psi}^{\text{excl.}} = \frac{N_{J/\psi}}{1 + f_D}\,, \tag{5.2}$$

where the correction for the feed-down is 2% for the semi-forward and semi-backward analysis,

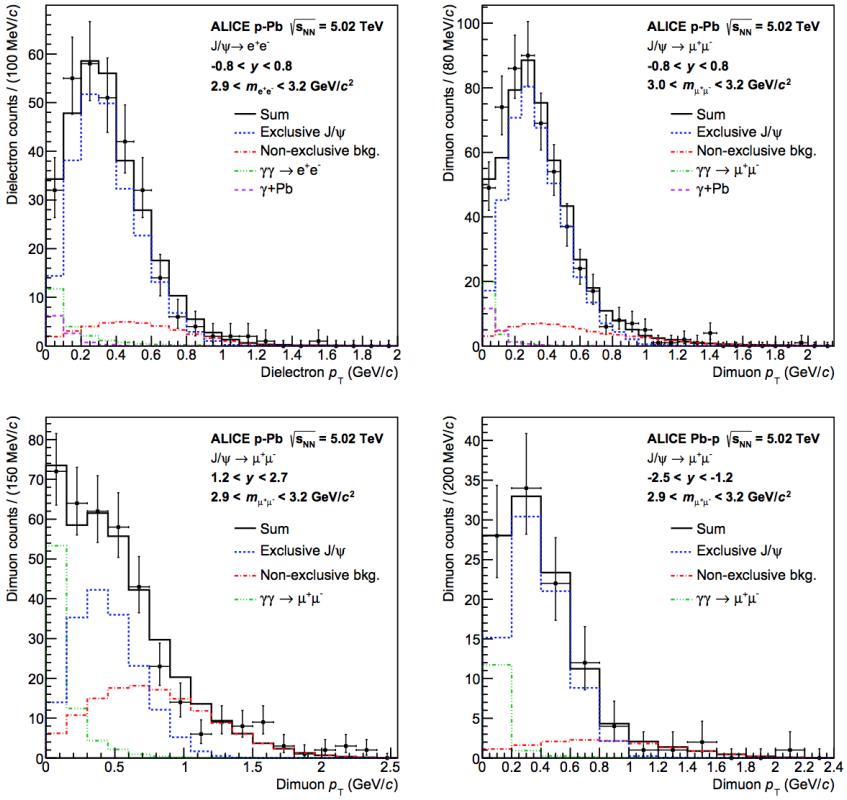

Fig. 5.7: Transverse momentum distributions of dileptons around the J/ψ mass for the dielectron (upper left) and dimuon (upper right) samples for the central analysis and dimuon samples for the semi-forward (lower left) and semi-backward (lower right) analyses. In all cases the data are represented by points with error bars. The blue, magenta (dash) and green (dash-dot-dot) lines correspond to Monte Carlo templates for J/ψ coming from exclusive photoproduction off protons or off lead and continuous dilepton production respectively. The red (dashdot) line is a template for dissociative and hadronic background obtained from data. The solid black line is the sum of all contributions [64].

4% for the central analysis and between 7.9% and 11% for the forward and backward analyses.

The cross sections for exclusive J/ψ production off protons are then obtained as follows,

$$\frac{\mathrm{d}\sigma}{\mathrm{d}y} = \frac{N^{\mathrm{excl.}}_{J/\psi}}{\varepsilon \times A \cdot \mathrm{BR}(J/\psi \to l^+l^-) \cdot L \cdot \Delta y}\,, \tag{5.3}$$

where Δy denotes the rapidity interval, the branching ratios of J/ψ decaying into muon and electron pairs, $\mathrm{BR}(J/\psi \to l^+l^-)$ are taken from [35], and efficiency$\times$acceptance is obtained from MC simulation.

Using equation (1.13), cross sections (5.3), *i.e.*, Pb scattering off protons, can be related to photoproduction cross sections off protons. Using STARLIGHT, the photon flux, $k\mathrm{d}N_\gamma/\mathrm{d}k$, has been computed in impact parameter space and convoluted with the probability of no hadronic interaction for each considered rapidity interval. Likewise, mean $W_{\gamma p}$ energies were computed for each rapidity interval by averaging $W_{\gamma p}$ with the photoproduction cross section from

STARLIGHT.

As a result, in figure 5.8 the energy dependence of exclusive J/ψ photoproduction off protons is shown as a function of $W_{\gamma p}$. The error bars shown in this figure are computed as the quadratic sum of the statistical and the total systematic uncertainties, where the total systematic uncertainties have two contributions: one due to the measurement procedure and a second contribution due to the uncertainty in the photon flux. The ALICE data points cover the $W_{\gamma p}$ range from 24 to

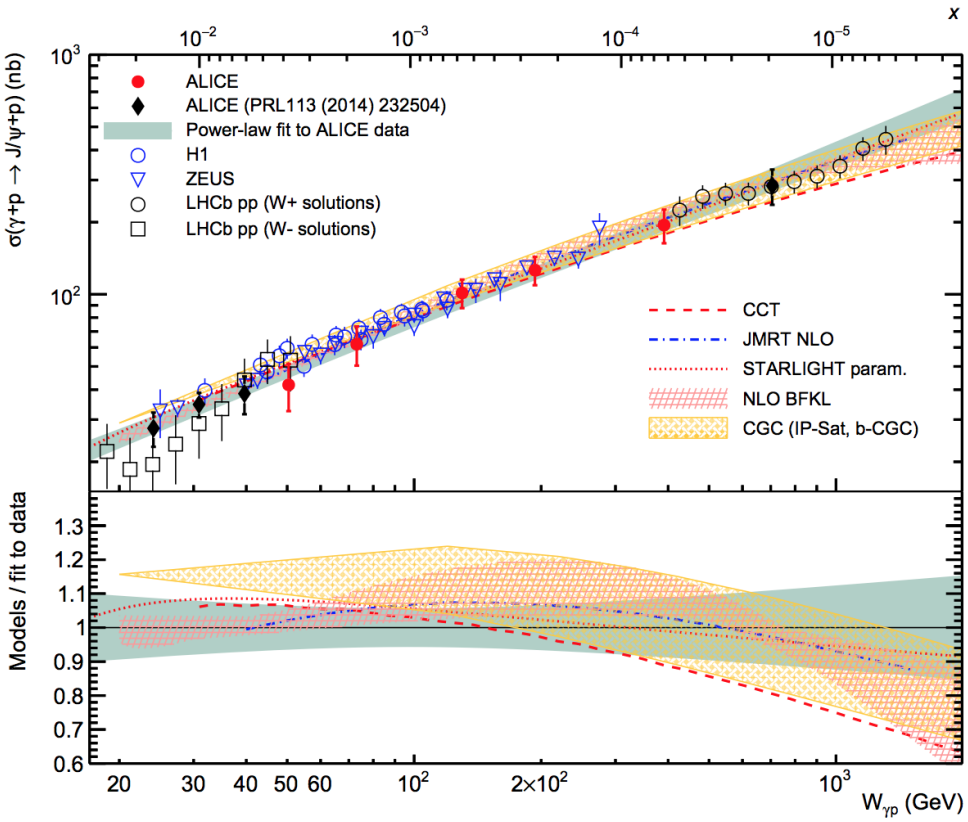

Fig. 5.8: (Upper panel) ALICE data (red symbols) on exclusive photoproduction of J/ψ off protons as a function of the center-of-mass energy of the photon–proton system $W_{\gamma p}$, obtained in collisions of protons and lead nuclei at $\sqrt{s_{\mathrm{NN}}} = 5.02$ TeV, including results from [63], compared to a power-law fit, to data from HERA [66, 67], to the solutions from LHCb [68] and to theoretical models. The uncertainties are the quadratic sum of the statistical and systematic uncertainties. (Lower panel) Ratio of the models shown in the upper panel to the power law fit through the ALICE data points. The Bjorken-x value corresponding to $W_{\gamma p}$ is also displayed on the top of the Figure [64].

706 GeV, which corresponds about to three orders of magnitude in Bjorken-x, from $\approx 2 \times 10^{-2}$ to $\approx 2 \times 10^{-5}$.

Following similar analyses at HERA [69], a power-law function,

$$f\left(W_{\gamma p}; N, W_0, \delta\right) = N \left(\frac{W_{\gamma p}}{W_0}\right)^{\delta}, \tag{5.4}$$

was fitted to the ALICE data with $W_0 = 90$ GeV. Both, the statistical and the systematic errors were taken into account in this fit, using a technique due to H1 [70]. Performing a χ^2 fit of (5.4) to the ALICE data,

$$N = 71.8 \pm 4.1 \text{ nb , and} \tag{5.5}$$

$$\delta = 0.70 \pm 0.05 \tag{5.6}$$

were obtained. The value of the exponent, δ, is compatible to earlier measurement by ALICE using the forward and backward data points alone [63]; it is also compatible to measurements at HERA [66, 67].

LHCb measured the exclusive production of J/ψ in pp collisions, where the photon source can not be identified because of the symmetry of the collision system. In order to extract the photoproduction cross section further assumptions are needed. LHCb reported for each measurement the two *solutions*, $W+$ and $W-$, [68] shown in figure 5.8, which agree with the ALICE measurements.

The ALICE measurements in figure 5.8 were also compared to a number of theory predictions:

- **CCT** [71]: This model is based on the color dipole approach. It takes into account the energy dependence of geometrical fluctuations of the proton structure in the impact parameter plane.
- **JMRT NLO** [72]: There are two predictions by the JMRT group. One of these is based on leading-order (LO) result from [73] while the second prediction also includes next-to-leading order (NLO) corrections. The parameters of both models have been determined by a fit to the same data set. As both models predict a very similar energy dependence, only the NLO prediction is shown.
- **STARLIGHT** [10]: The STARLIGHT prediction relies on a power-law fit to fixed target and to HERA data.
- **NLO BFKL** [74]: the BFKL evolution of HERA values (HERA Fit 2) with a photoproduction scale of $M^2 = 2.39$ GeV^2.
- **CGC** [75], a color dipole model.

All these models predictions, which are based on different physics assumptions, agree with the ALICE measurements within the current experimental uncertainties.

6 Outlook on LHC run 3 and 4

6.1 ALICE upgrades for LHC Run 3 and 4

Currently the ALICE experiment is being upgraded in view of the upcoming runs 3 and 4 of the LHC. According to the ALICE Upgrade LoI [76], the foreseen interaction rate in Pb-Pb collisions in Run 3 and Run 4 is 50 kHz. The precise filling scheme is not yet available but bunch trains with either 50 ns or 25 ns minimum bunch spacing will certainly be used.

During run 3 and run 4, ALICE will take data both in triggered mode and in continuous readout mode [77, 78]. In continuous readout mode there are no longer significant trigger and dead-time inefficiencies. Thus, ALICE will be able to integrate most of the delivered luminosity. Unlike in run 1 and 2, no trigger capabilities will be available in the central detectors. Therefore, the only way to collect ultra-peripheral events, which are characterized by rapidity gaps on both sides of the central rapidity region, is in continuous readout mode.

The inner tracking system, which in LHC runs 1 and 2 consisted of 6 layers of silicon-based detectors, being completely rebuilt, using newer silicon detector technologies and will have 7 layers. Whereas in run 1 and 2 the innermost layer was at a radial distance of 39 mm to the interaction point, the innermost layer in the upgraded ITS will between 22.4 and 26.7 mm away in the radial direction from the interaction point. Figure 6.1 shows the improvement in vertex pointing resolution and in momentum resolution expected for the upgraded ITS and central barrel.

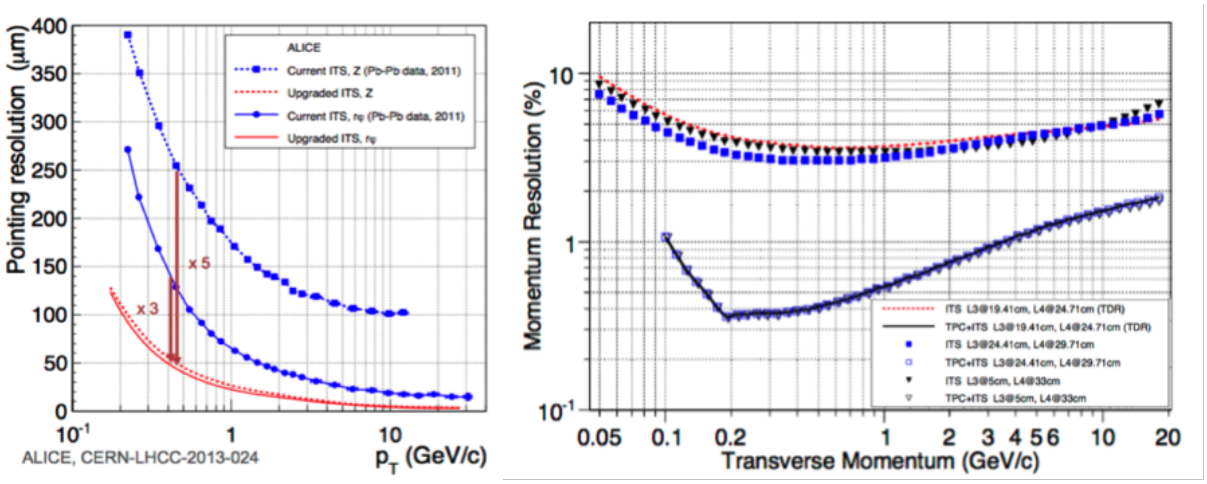

Fig. 6.1: Expected pointing resolution of the upgraded ALICE ITS (left); Expected momentum resolution of the ALICE upgraded central barrel (right); Taken from [79].

The time projection chamber is being upgraded in order to be able to cope with an interaction rate of 50 kHz in Pb-Pb collisions [80]. This is going to be achieved by replacing the multi-wire proportional chambers at the end plates of the TPC with a read-out based on so-called GEMs (Gas Electron Multiplier) [81].

The vetoes used in ultra-peripheral triggers in LHC run 1 and 2 will be replaced by requirements on the Fast Interaction Trigger (FIT) detector [82], which consists of the upgraded T0, VZERO, and AD detectors.

AD upgrade

The upgrade of AD, called Forward Diffraction Detector (FDD), is foreseen to proceed in the context of the FIT [82] detector, which originally included upgraded version of the T0 and VZERO detectors, only.

For the FDD, the locations, sizes, and the segmentation of the plastic scintillators will be the same as for AD. Also the way the light is extracted from the scintillator using wavelength shifting bars followed by clear fibers will be the same as for AD.

Due to a combination of (1) having large pulses, because mostly showers of secondary particles are seen by AD/FDD and (2) the fact that the time constant of the wavelength shifting bars used in AD is rather long, $\tau_{\mathrm{WLS}} \approx 8.5$ ns, typical pulses in Pb-Pb collisions in run 2 have been found to be considerably longer than one bunch crossing (25 ns). As a consequence, triggers following a large pulse can be shadowed because a pulse may not return below the threshold before the next pulse arrives.

Because this shadowing effect increases with increasing interaction rate, FDD wavelength shifting bars with a smaller time constant will be used, such as Nanostructured Organosilicon Luminophores (NOL), which have high photo-luminescence quantum yields and decay times τ_{WLS} down to 1 ns, to be compared to the 8.5 ns for the present EJ-280 AD wavelength shifters.

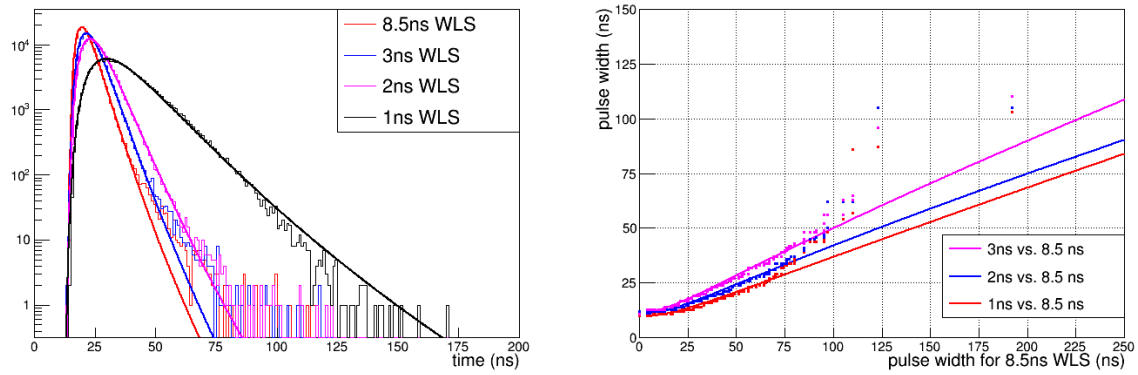

Fig. 6.2: Left: pulse shapes for different time constants τ_{WLS} in the wavelength shifting bars. The solid lines are fits of log-normal pulse function (6.1) to the simulated data. Right: pulse widths w.r.t. pulse width for 8.5 ns time constant for pulses with the same charge.

The effect of using wavelength shifting bars with shorter time constants on the pulse width can be estimated in the following way: input are GEANT4 [83] simulations for different time constants τ_{WLS} in the wavelength shifting bars where a minimum ionizing particle is hitting

the center of an FDD module, and the photons created in the scintillator are individually traced through the scintillator, the wavelength shifting bars and the clear fibers.[1] To the time distribution of these photons at the end of the clear fibers, a so-called log-normal pulse shape function is fitted,

$$f(t;t_0,\tau,\sigma) = \exp\left(-\frac{\left(\ln(t-t_0)-\mu\right)^2}{2\sigma^2}\right) \tag{6.1}$$

see figure 6.2 left. Using these log-normal functions for simulations with different time constants in the wavelength shifting fibers, one can then relate the width of a pulse for a time constant of 8.5 ns to the width of a pulse with the same integral, *i.e.*, charge, with a smaller time constant. This simple simulation indicates that the width of pulses can be reduced by more than a factor of ≈ 3 when using materials for the wavelength shifting bars with time constants less than 8.5 ns.

For maximum light collection efficiency, the absorption spectrum of the wavelength shifting bars needs to be matched to the emission spectrum of the scintillator. Therefore, using different wavelength shifting bars makes it necessary to use a different scintillator material which better matches the absorption spectrum. For FDD, the scintillator material matched to the fast wavelengths shifting bars made of NOL-38 will be BC-420.

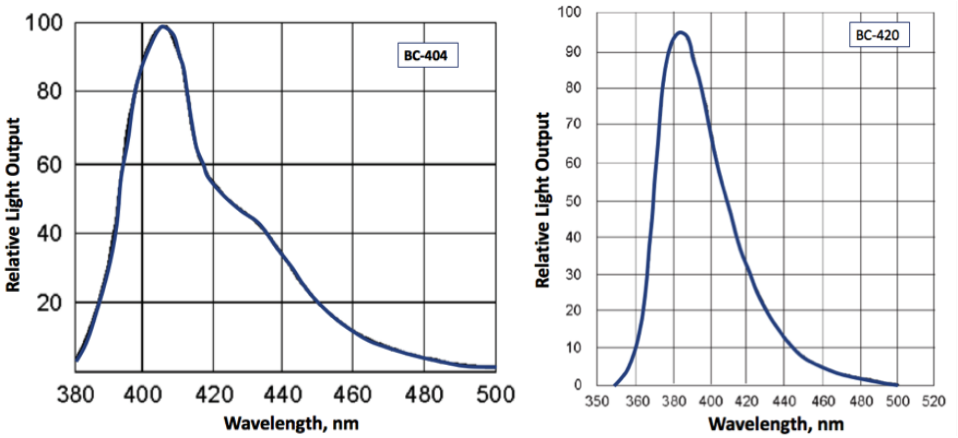

Fig. 6.3: Comparison of scintillation light wavelength spectra between BC-404 (left) and BC-420 (right).

In figure 6.3, emission spectra of the scintillator materials used in AD and in FDD are shown and in figure 6.4 the different absorption and emission spectra of the wavelength shifting bars are shown. Note that for FDD the overlap between absorption and emission is larger than for AD, indicating that the relative number of multiple absorptions is higher than for AD. However the effect of multiple re-absorptions on the pulse length is smaller than for AD given that the time constant is of the order of 1 ns.

[1] The GEANT4 simulations were performed by I. Monzon.

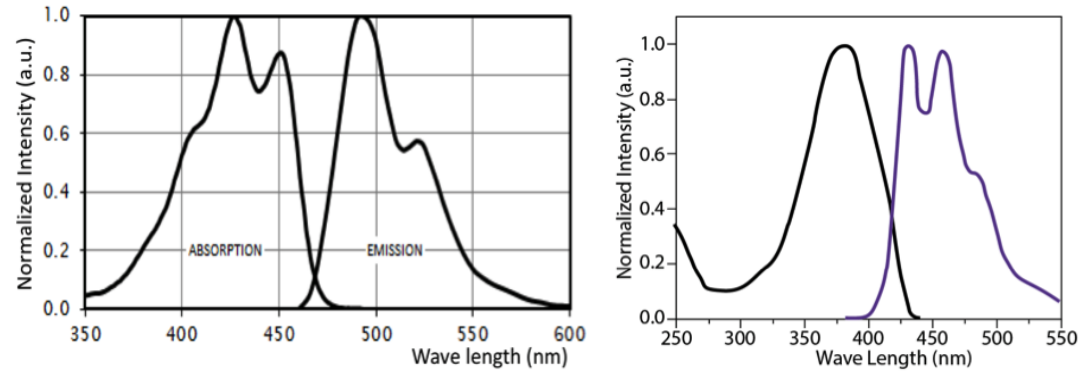

Fig. 6.4: Absorption and emission spectra as a function of wavelength, for wavelength shifter EJ-280 produced by Saint-Gobain, presently used in the AD (left), and NOL-38, produced by LuminoTech, Moscow (right).

In December 2018 a first module for the FDD has been assembled, with a scintillator made out of BC-420 and wavelength shifting bars made of NOL-38. Since no test beams are available at CERN until the start of run 3, the new module is being tested using cosmic muons. For these tests, a copy of the AD front-end electronics, which is located at the Meyrin site of CERN, is used. In figure 6.5 distributions of width (time over threshold) vs. charge (integral over a pulse) for an AD and an FDD module are compared. Due to the effect of time-slewing, larger pulses have larged widths. However, it can be clearly seen that for the same charge the pulses from the FDD module are shorter than the pulses from the AD module. This first successful test of an FDD module indicates that the pulses from the new FDD module are indeed shorter than pulses from AD modules.

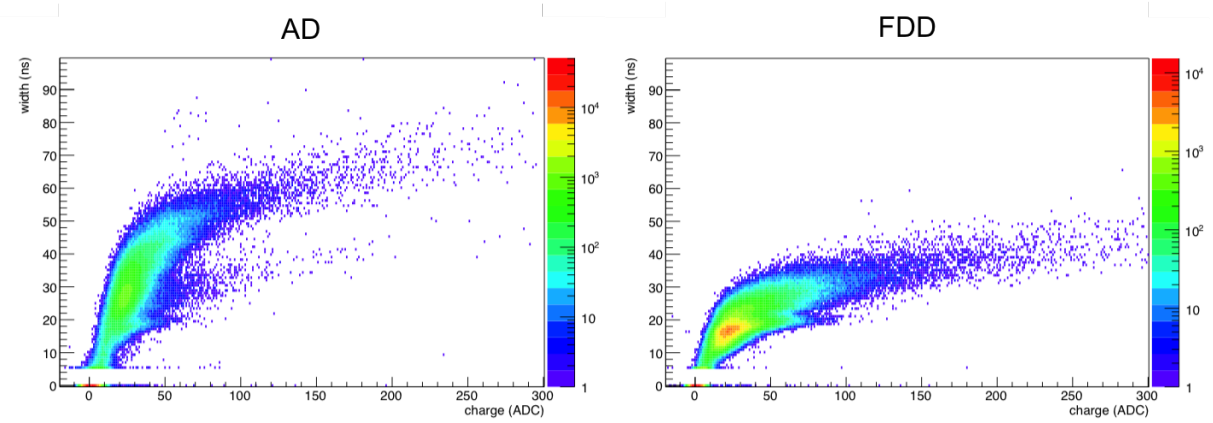

Fig. 6.5: Left: pulse width vs. charge for an AD module; Right: pulse width vs. charge for an FDD module. For these measurements, The PMT gains and the fixed thresholds were equalized.

The front-end electronics for the FDD will be based on the one which is being developed for FIT. This will allow to operate FDD in continuous readout mode, which is important for ultra-peripheral physics, given the absence of triggering capabilities in all central detectors in run 3 and 4, as discussed above.

6.2 Prospects for UPC measurements in LHC Run 3 and 4

An outlook on ultra-peripheral measurements in the forthcoming runs 3 and 4 of the LHC can be found a recent LPCC report, see section 10 in [84]. Here we summarize prospects for UPC measurements in LHC run 3 and 4 for Pb-Pb collisions. For other collision systems like p-Pb and collisions using other ions species besides Pb, we refer to the LPCC report.

The total acceptance×efficiency for ultra-peripheral events in ALICE is determined by the tracking efficiencies and the geometrical acceptances of the inner tracking system [79], of the time projection chamber [80, 81], and of the Muon Spectrometer [85]. In particular there will be no trigger inefficiencies anymore.

Table 6.1 shows acceptance cuts used in the LPCC report for estimating the yields of a number of ultra-peripheral processes in LHC runs 3 and 4, where the acceptances called "central 1" and "forward 1" correspond to the ones for ALICE. For these estimates, STARLIGHT is used as a baseline. However, since STARLIGHT does not include nuclear shadowing, a rapidity-dependent nuclear shadowing correction following [56] for the heavy quarkonium J/ψ, $\Psi(2S)$ and $\Upsilon(1S)$ was applied. This correction reduces the cross sections and rates obtained from STARLIGHT by factors of 0.42, 0.475 and 0.77 for the J/ψ, $\Psi(2S)$ and $\Upsilon(1S)$ respectively.

Table 6.1: Table of toy-model acceptance cuts for the different experiments [84].

Condition	Central 1 Narrow	Central 2 Wide	Forward 1 Narrow	Forward 2 Wide
Rapidity	$\|\eta\| < 0.9$	$\|\eta\| < 2.4$	$2.5 < \eta < 4.0$	$2 < \eta < 5$
$e/\pi/\mu$ pseudo-rapidity	$\|\eta\| < 0.9$	$\|\eta\| < 2.4$	$2.5 < \eta < 4.0$	$2 < \eta < 5$

Table 6.2: Table of cross sections and numbers of events in 13 nb^{-1} integrated luminosity for the different mesons in Pb-Pb collisions [84]. B, M and K denote 10^9, 10^6 and 10^3 respectively. Both the rates and cross sections include the relevant branching ratios. The cross sections and toy-model acceptances are determined using STARLIGHT [10]. For the J/ψ, $\Psi(2S)$ and $\Upsilon(1S)$, rapidity-dependent nuclear shadowing cross sections have been applied following the approach in [56].

Meson	σ	All	Central 1	Central 2	Forward 1	Forward 2
$\rho \to \pi^+\pi^-$	5.2b	68 B	5.5 B	21 B	4.9 B	13 B
$\rho' \to \pi^+\pi^-\pi^+\pi^-$	730 mb	9.5 B	210 M	2.5 B	190 M	1.2 B
$\phi \to K^+K^-$	0.22b	2.9 B	82 M	490 M	15 M	330 M
J/$\psi \to \mu^+\mu^-$	1.0mb	14 M	1.1 M	5.7 M	600 K	1.6 M
$\Psi(2S) \to \mu^+\mu^-$	30μb	400 K	35 K	180 K	19 K	47 K
$\Upsilon(2S) \to \mu^+\mu^-$	2.0μb	26 K	2.8 K	14 K	880	2.0 K

As a result, table 6.2 shows cross sections together with estimated yields for Pb-Pb collisions in LHC runs 3 and 4 for an integrated luminosity of 13 nb^{-1}. The large expected number of events for high-mass vector mesons J/ψ, $\Psi(2S)$ and $\Upsilon(1S)$ should allow tomographic measurements from which information on the nuclear wave function can be obtained. In the $\pi^+\pi^-$ channel the range of invariant masses above 2 GeV/c^2 will become accessible.

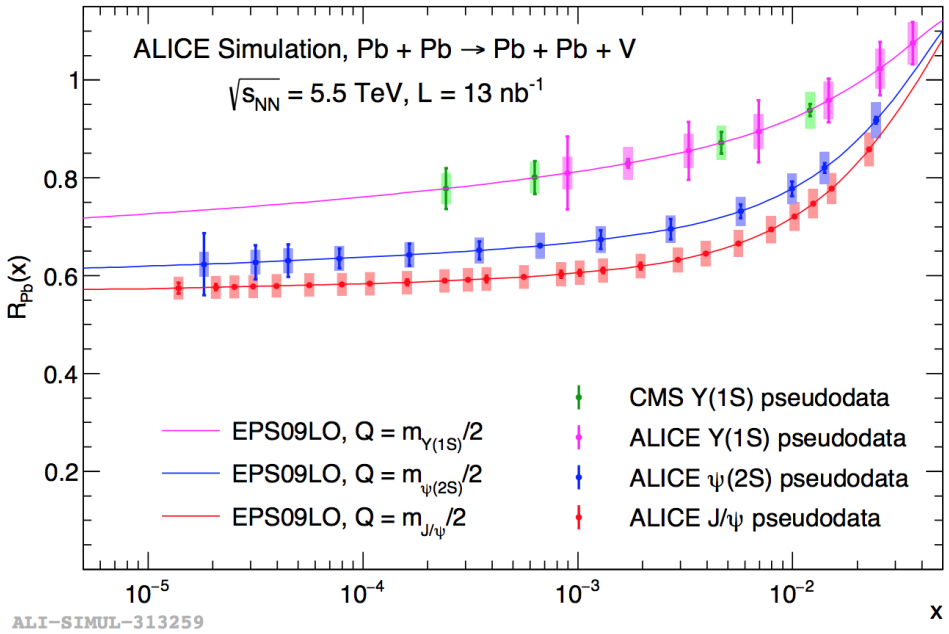

Fig. 6.6: Pseudo-data projections for the nuclear suppression factor by ALICE and CMS measured with the photoproduction of three heavy vector mesons in Pb-Pb ultra-peripheral collisions are shown [84]. The pseudo-data points are derived from EPS09-based photoproduction cross section projections following the method described in [86].

Finally, figure 6.6 shows pseudo-data projections for the nuclear suppression factor by ALICE and CMS measured with the photoproduction of three heavy vector mesons in Pb-Pb ultra-peripheral collisions. For ρ^0 nuclear shadowing is about a factor of 2 stronger than in the approach based on the Glauber model and the vector meson dominance model [52].

7 Summary and conclusions

In this thesis, ALICE measurements on photoproduction of $\rho^0 \to \pi^+\pi^-$ and of continuum production of $\gamma\gamma \to e^+e^-$ in ultra-peripheral collision of lead ions at $\sqrt{s_{NN}} = 2.76$ TeV at the LHC [32] are summarized. The cross section for ρ^0 photoproduction at mid-rapidity is compared to a number of model predictions, and is found to be compatible with the prediction by the STARLIGHT model [10], while all other models over-estimate the measured cross section. The fact that the GDL (Glauber-Donnachie-Landshoff) prediction [50, 51] is about a factor of two above the data may be explained by the presence of nuclear shadowing [56].

The ALICE cross section measurement of $\gamma\gamma \to e^+e^-$ in Pb-Pb collisions at $\sqrt{s_{\rm NN}} = 2.76$ TeV [32, 47], measured at mid-rapidity in different ranges of dielectron invariant mass in the range between 0.6 and 10 GeV/c^2, is compatible with the predictions of STARLIGHT. This cross section depends on the photon flux, which is well known, and on the process $\gamma\gamma \to e^+e^-$ which is calculable using perturbative QED. The fact that the model predictions agree with the measurements indicates that our current understanding of the theory are sufficient in order for the prediction to be compatible with the measurements. In particular it sets constraints on QED calculations that in include higher-order of $\alpha_{\rm EM}$ [87, 88], *e.g.*, in [89, 90], a reduction in the two-photon cross section of up to 30% compared with leading-order calculations has been predicted.

In addition to the cross section for continuum photoproduction of lepton pairs, ALICE has also measured cross section for J/ψ photoproduction in Pb-Pb collisions at $\sqrt{s_{\rm NN}} = 2.76$ TeV [47, 58]. The measured coherent J/ψ cross section at mid-rapidity is found to be in good agreement with the model AB-EPS09, which takes into account nuclear gluon shadowing according to the EPS09 parametrization. Those models which include no nuclear gluon shadowing are inconsistent with the measured results, as are models take into account nuclear effects by the Glauber model. The predictions from a calculation using the leading twist approximation (RSZ-LTA) are about 3 sigma below our measurement. However, the deviation from the upper limit of this model is only 1.5 sigma.

ALICE has measured the photoproduction of J/ψ mesons off protons in p–Pb interactions at $\sqrt{s_{\rm NN}} = 5.02$ TeV in different intervals of rapidity, using the muon forward spectrometer, the central barrel and a combination of both [63, 64]. The different intervals in rapidity probe $W_{\gamma p}$ energies from 24 to 706 GeV, corresponding to about three orders of magnitude in Bjorken-x, from $\approx 2\times10^{-2}$ to $\approx 2\times10^{-5}$. All considered models, which are based on different physics assumptions, are are compatible with the data within current uncertainties. However, it is interesting that, although the model predictions around and above 1 TeV are not very precise, all tend to be lower than then power-law fit in this region. This energy range will be reachable with the nebw LHC data from Run 2 and the data to be collected in Run 3 and Run 4.

In the upcoming runs 3 and 4 of the LHC, the higher LHC luminosity and the upgrade of ALICE will allow us to collect significantly more UPC events than during runs 1 and 2. In particular the use of continuous readout [78] will eliminate most of the limitations due to trigger inefficiencies. As explained in section 5, continuous readout is the only way in run 3 and 4 in which ultra-peripheral events can be collected in ALICE, since none of the central detectors will have trigger capabilities anymore.

The estimated number of events for light meson production are very large: we expect to collect billions of ρ^0 and ρ' events and hundreds of millions on ϕ mesons. In addition to precise cross section measurements, the expected rates for J/ψ, $\Psi(2S)$ and $\Upsilon(1S)$ should be sufficient for multi-differential, tomographic measurements from which information about the nuclear wave functions can be obtained. For final states of $\pi^+\pi^-$, dipion invariant masses above 2 GeV/c^2 will come into reach.

The following list of measurements of vector meson photoproduction which will become possible in LHC runs 3 and 4, which is partially taken in part from [78], shows that there are many new opportunities to improve our understanding of photo-nuclear interactions producing heavy, light, and multiple vector mesons.

- Extend substantially the x range for coherent J/ψ photoproduction on nuclei using information on the impact parameter distribution in peripheral and ultra-peripheral collisions provided by forward neutron production
- Measure with high enough statistics coherent $\Upsilon(1S)$ production in γ-p and γ-A scattering to check the expectation of the 20% reduction of the coherent cross section, which would allow one to probe gluon shadowing at a factor of ≈ 10 higher Q^2 than in J/ψ production.
- Study coherent production of two pions with masses above 1 GeV/c^2 to study an interplay of soft and hard dynamics as a function of $M(\pi\pi)$ and $p_T(\pi)$.
- Measure the production of heavier 2π, 4π and other resonances on ion targets, and search for the photoproduction of the observed exotic mesons.

In addition to the $\gamma\gamma$ processes described in this thesis in section 4, *i.e.*, continuum dielectron production, it would be very interesting to also measure the continuum production of proton anti-proton pairs with large statistics. Another interesting $\gamma\gamma$ process is light-by-light scattering, which recently has been measured for the first time by ATLAS and by CMS [91–93]. In run 3 and 4 ALICE might be able to measure light-by-light scattering for diphoton energies $M_{\gamma\gamma}$ below ≈ 3 GeV. For such low $M_{\gamma\gamma}$ the light-by-light scattering cross section is large, however there is also a large contribution from pseudo-scalar resonances such as η, $\eta'(958)$ decaying into two photons. For some ideas on how to disentangle these, see [94].

8 Author's contribution

Section 1

– I developed and implemented a MC generator for spin-1 particles decaying into $\pi^+\pi^-$ with flat distributions for invariant-mass, pair transverse momentum, and pair rapidity, see section 1.4. This generator was used, together with STARLIGHT, in the ρ^0 analyses and has the advantage that the sampling in invariant mass is uniform, *i.e.*, statistical fluctuations at the tails of the invariant mass distribution are avoided.

Section 2

– AD detector:
  – I was part of the test of AD detector modules in a PS test beam, where I helped to get the front-end electronics to work and then analyzed the data.
  – I adapted the FPGA firmware from VZERO to AD, which involved, *e.g.*, adding coincidences between adjacent pads.
  – I adapted and extended the detector control system which is based on the one for VZERO to AD.
  – I develped a correction for ADC saturation, which is performed in a calibration pass, and allows to use AD as a new centrality estimator in ALICE.
  – I took care about the calibration of the AD detector which involved making HV gain curves, doing the channel timing equalization, and the set-up of beam-beam and beam-gas timing windows.
  – I extended and fixed bugs in the offline code for AD reconstruction and MC simulation
  – Day-to-day taking care of detector operations

– I developed the topological SPD triggers which were used in UPC triggers in ALICE, including MC studies and verification of the implementation in the SPD FPGA. Without these triggers only a fraction of the data could have been collected.

– I contributed to the understanding of the effect of imposing vetoes on activity in VZERO and AD online vs. offline.

Section 3

– I performed the analysis for the measurement of the cross section of coherent ρ^0 photoproduction at mid-rapidity in Pb-Pb collisions in LHC run 1

– Determination of the integrated luminosity for UPC triggered events: due to late particles there is a tail in TOF activity after minimum-bias collisions which can shadow UPC events. When this is not taken into account, the luminosity for ultra-peripheral triggers is severely biased. For the first data sample used in the ρ^0 analysis at $\sqrt{s_{\mathrm{NN}}} = 2.76$ TeV the correction for TOF trigger dead time was ≈ 1 and for the 2nd data sample it was ≈ 5.

– I developed and implemented a correction for the SPD fast-or chip efficiency which was used in MC simulations used for the ρ^0, J/ψ and $\gamma\gamma \to e^+e^-$ analyses.

Section 4

– I performed the measurement of the cross section of coherent $\gamma\gamma \to e^+e^-$ cross section at mid-rapidity in Pb-Pb collision in LHC run 1 in the e^+e^- invariant-mass range from 0.6 to 10 GeV/c^2.

Section 5

– I estimated efficiency$\times$acceptance for J/ψs decaying in the central rapidity region

– I estimated the luminosity for the data sample used in the J/ψãnalysis in Pb-Pb collisions.

Section 6

– I contributed to the upgrade of AD for LHC runs 3 and 4, including analyzing data comparing a new FDD module with an AD module and developing a strategy for how to use the FIT front-end electronics for FDD.

– I contributed to the estimates for the expected yield of various UPC processes in Pb-Pb collisions for LHC runs 3 and 4 (table 6.2)

9 Acknowledgments

I am very grateful to Prof. Marek Kowalski for directing me towards ultra-peripheral physics and for his continuous support over the last 9 years. Likewise, I would like to thank the ALICE group in the Institute for Nuclear Physics in Kraków, in particular Prof. Lidia Goerlich and Prof. Jan Figiel, for welcoming me at a time when not many people from outside Poland were part of this group.

This work would not have been possible without the guidance of, and cooperation with Prof. Joakim Nystrand; the two visits to Bergen in the beginning of my work in this field helped a lot to get started in ultra-peripheral analysis. I am also grateful to Prof. Eugenio Scapparone for his support during the time when he was coordinating the UPC analysis group.

I gratefully acknowledge the support of the ALICE group at CERN, and of CERN, not only during the four times I was able to work at CERN as a Corresponding Associate.

Finally, I would like to thank Prof. Jean-Pierre Revol for his support over the last few years. I am very grateful for the opportunity to follow the development of the AD detector, from test measurements in a test beam at the CERN PS, through its installation, day-to-day taking care of it, and most recently the preparations for its upgrade.

This work was supported by the grants UMO–2012/05/B/STE/02524, UMO–2013/08/M/ST2/00598, and UMO–2016/22/M/ST2/00176 from the Polish National Science Center (NCN), and by DIR/WK/2016/2018/17–1 from the Polish Ministry of Science and Higher Education (MNiSW).

References

[1] G. Baur, K. Hencken, D. Trautmann, S. Sadovsky, and Y. Kharlov, "Coherent gamma gamma and gamma-A interactions in very peripheral collisions at relativistic ion colliders," *Phys. Rept.* **364** (2002) 359–450, arXiv:hep-ph/0112211 [hep-ph].

[2] A. J. Baltz, "The Physics of Ultraperipheral Collisions at the LHC," *Phys. Rept.* **458** (2008) 1–171, arXiv:0706.3356 [nucl-ex].

[3] S. Klein and J. Nystrand, "Ultraperipheral nuclear collisions," *Phys. Today* **70** no. 10, (2017) 40–47.

[4] E. Fermi, "On the theory of collisions between atoms and electrically charged particles," *Nuovo Cim.* **2** (1925) 143–158, arXiv:hep-th/0205086 [hep-th]. [,243(1925)].

[5] E. Fermi, "On the Theory of the impact between atoms and electrically charged particles," *Z. Phys.* **29** (1924) 315–327.

[6] C. F. von Weizsacker, "Radiation emitted in collisions of very fast electrons," *Z. Phys.* **88** (1934) 612–625.

[7] E. J. Williams, "Nature of the high-energy particles of penetrating radiation and status of ionization and radiation formulae," *Phys. Rev.* **45** (1934) 729–730.

[8] C. A. Bertulani, S. R. Klein, and J. Nystrand, "Physics of ultra-peripheral nuclear collisions," *Ann. Rev. Nucl. Part. Sci.* **55** (2005) 271–310, arXiv:nucl-ex/0502005 [nucl-ex].

[9] S. Klein and J. Nystrand, "Exclusive vector meson production in relativistic heavy ion collisions," *Phys. Rev.* **C60** (1999) 014903, arXiv:hep-ph/9902259 [hep-ph].

[10] S. R. Klein, J. Nystrand, J. Seger, Y. Gorbunov, and J. Butterworth, "STARlight: A Monte Carlo simulation program for ultra-peripheral collisions of relativistic ions," *Comput. Phys. Commun.* **212** (2017) 258–268, arXiv:1607.03838 [hep-ph].

[11] R. D. Woods and D. S. Saxon, "Diffuse Surface Optical Model for Nucleon-Nuclei Scattering," *Phys. Rev.* **95** (1954) 577–578.

[12] **H1, ZEUS** Collaboration, N. Cartiglia, "Diffraction at HERA," in *The Strong interaction, from hadrons to partons: Proceedings, 24th SLAC Summer Institute on Particle Physics (SSI 96), Stanford, Calif., 19-30 Aug 1996*, pp. 337–363. 1996. arXiv:hep-ph/9703245 [hep-ph].
http://www.slac.stanford.edu/pubs/confproc/ssi96/ssi96-014.html.

[13] L. Frankfurt, M. Strikman, and M. Zhalov, "Elastic and large t rapidity gap vector meson production in ultraperipheral proton-ion collisions," *Phys. Lett.* **B640** (2006) 162–169, arXiv:hep-ph/0605160 [hep-ph].

[14] V. Guzey and M. Zhalov, "Rapidity and momentum transfer distributions of coherent J/ψ photoproduction in ultraperipheral pPb collisions at the LHC," *JHEP* **02** (2014) 046, arXiv:1307.6689 [hep-ph].

[15] A. J. Baltz, S. R. Klein, and J. Nystrand, "Coherent vector meson photoproduction with nuclear breakup in relativistic heavy ion collisions," *Phys. Rev. Lett.* **89** (2002) 012301, arXiv:nucl-th/0205031 [nucl-th].

[16] A. J. Baltz, M. J. Rhoades-Brown, and J. Weneser, "Heavy ion partial beam lifetimes due to Coulomb induced processes," *Phys. Rev.* **E54** (1996) 4233–4239.

[17] **ALICE** Collaboration, N. Antoniou *et al.*, "Letter of Intent for A Large Ion Collider Experiment,".

[18] **ALICE** Collaboration, P. Cortese *et al.*, "ALICE: Physics performance report, volume I," *J. Phys.* **G30** (2004) 1517–1763.

[19] **ALICE** Collaboration, C. W. Fabjan *et al.*, "ALICE: Physics performance report, volume II," *J. Phys.* **G32** (2006) 1295–2040.

[20] **ALICE** Collaboration, K. Aamodt *et al.*, "The ALICE experiment at the CERN LHC," *JINST* **3** (2008) S08002.

[21] **ALICE** Collaboration, B. B. Abelev *et al.*, "Performance of the ALICE Experiment at the CERN LHC," *Int. J. Mod. Phys.* **A29** (2014) 1430044, arXiv:1402.4476 [nucl-ex].

[22] **ALICE** Collaboration, G. Dellacasa *et al.*, "ALICE technical design report of the time-of-flight system (TOF),".

[23] **ALICE** Collaboration, P. Cortese *et al.*, "ALICE: Addendum to the technical design report of the time of flight system (TOF),".

[24] A. Akindinov *et al.*, "Performance of the ALICE Time-Of-Flight detector at the LHC," *Eur. Phys. J. Plus* **128** (2013) 44.

[25] **ALICE** Collaboration, F. Carnesecchi, "Performance of the ALICE Time-Of-Flight detector at the LHC," in *14th Workshop on Resistive Plate Chambers and Related Detectors (RCP2018) Puerto Vallarta, Jalisco State, Mexico, February 19-23, 2018.* 2018. arXiv:1806.03825 [physics.ins-det].

[26] A. Akindinov *et al.*, "A topological trigger based on the Time-of-Flight detector for the ALICE experiment," *Nucl. Instrum. Meth.* **A602** (2009) 372–376.

[27] **ALICE** Collaboration, E. Abbas *et al.*, "Performance of the ALICE VZERO system," *JINST* **8** (2013) P10016, arXiv:1306.3130 [nucl-ex].

[28] J. Christiansen, "HPTDC High Performance Time to Digital Converter," tech. rep., CERN, Geneva, 2004. https://cds.cern.ch/record/1067476. Version 2.2 for HPTDC version 1.3.

[29] **LHC Forward Physics Working Group** Collaboration, K. Akiba *et al.*, "LHC Forward Physics," *J. Phys.* **G43** (2016) 110201, arXiv:1611.05079 [hep-ph].

[30] **ALICE** Collaboration, B. Abelev *et al.*, "Measurement of the Cross Section for Electromagnetic Dissociation with Neutron Emission in Pb-Pb Collisions at $\sqrt{s_{NN}}$ = 2.76 TeV," *Phys. Rev. Lett.* **109** (2012) 252302, arXiv:1203.2436 [nucl-ex].

[31] **ALICE** Collaboration, "ALICE technical design report of the dimuon forward spectrometer,".

[32] **ALICE** Collaboration, J. Adam *et al.*, "Coherent ρ^0 photoproduction in ultra-peripheral Pb-Pb collisions at $\sqrt{s_{\rm NN}} = 2.76$ TeV," *JHEP* **09** (2015) 095, arXiv:1503.09177 [nucl-ex].

[33] **ALICE** Collaboration, C. Mayer, "Coherent photo-production of ρ^0 mesons in ultra-peripheral Pb-Pb collisions at the LHC measured by ALICE," *EPJ Web Conf.* **81** (2014) 02011.

[34] **ALICE** Collaboration, K. Skjerdal, "Photoproduction of ρ^0 in ultra–peripheral nuclear collisions at ALICE," *J. Phys. Conf. Ser.* **455** (2013) 012010, arXiv:1304.6850 [nucl-ex].

[35] **Particle Data Group** Collaboration, M. Tanabashi *et al.*, "Review of Particle Physics," *Phys. Rev.* **D98** no. 3, (2018) 030001.

[36] **STAR** Collaboration, B. I. Abelev *et al.*, "ρ^0 photoproduction in ultraperipheral relativistic heavy ion collisions at $\sqrt{s_{NN}}$ = 200 GeV," *Phys. Rev.* **C77** (2008) 034910, arXiv:0712.3320 [nucl-ex].

[37] S. van der Meer, "Calibration of the Effective Beam Height in the ISR,".

[38] P. Soding, "On the Apparent shift of the ρ meson mass in photoproduction," *Phys. Lett.* **19** (1966) 702–704.

[39] **STAR** Collaboration, G. Agakishiev *et al.*, "ρ^0 Photoproduction in AuAu Collisions at $\sqrt{s_{NN}}$=62.4 GeV with STAR," *Phys. Rev.* **C85** (2012) 014910, arXiv:1107.4630 [nucl-ex].

[40] **STAR** Collaboration, C. Adler *et al.*, "Coherent ρ^0 production in ultraperipheral heavy ion collisions," *Phys. Rev. Lett.* **89** (2002) 272302, arXiv:nucl-ex/0206004 [nucl-ex].

[41] T. Bauer, "High-energy photoproduction of nonresonant pi+ pi- pairs and the dipion final-state interaction," *Phys. Rev.* **D3** (1971) 2671–2685.

[42] M. H. Ross and L. Stodolsky, "Photon dissociation model for vector meson photoproduction," *Phys. Rev.* **149** (1966) 1172–1181.

[43] **ZEUS** Collaboration, J. Breitweg *et al.*, "Elastic and proton dissociative ρ^0 photoproduction at HERA," *Eur. Phys. J.* **C2** (1998) 247–267, arXiv:hep-ex/9712020 [hep-ex].

[44] **H1** Collaboration, S. Aid *et al.*, "Elastic photoproduction of rho0 mesons at HERA," *Nucl. Phys.* **B463** (1996) 3–32, arXiv:hep-ex/9601004 [hep-ex].

[45] **STAR** Collaboration, R. Debbe, "Rho Meson Diffraction off Au Nuclei," *J. Phys. Conf. Ser.* **389** (2012) 012042, arXiv:1209.0743 [nucl-ex].

[46] S. Abrahamyan *et al.*, "Measurement of the Neutron Radius of 208Pb Through Parity-Violation in Electron Scattering," *Phys. Rev. Lett.* **108** (2012) 112502, arXiv:1201.2568 [nucl-ex].

[47] **ALICE** Collaboration, E. Abbas *et al.*, "Charmonium and e^+e^- pair photoproduction at mid-rapidity in ultra-peripheral Pb-Pb collisions at $\sqrt{s_{\rm NN}}$=2.76 TeV," *Eur. Phys. J.* **C73** no. 11, (2013) 2617, arXiv:1305.1467 [nucl-ex].

[48] R. Barlow, "Asymmetric systematic errors," arXiv:physics/0306138 [physics].

[49] V. P. Goncalves and M. V. T. Machado, "Vector Meson Production in Coherent Hadronic Interactions: An update on predictions for RHIC and LHC," *Phys. Rev.* **C84** (2011) 011902, arXiv:1106.3036 [hep-ph].

[50] L. Frankfurt, M. Strikman, and M. Zhalov, "Signals for black body limit in coherent ultraperipheral heavy ion collisions," *Phys. Lett.* **B537** (2002) 51–61, arXiv:hep-ph/0204175 [hep-ph].

[51] V. Rebyakova, M. Strikman, and M. Zhalov, "Coherent ρ and J/ψ photoproduction in ultraperipheral processes with electromagnetic dissociation of heavy ions at RHIC and LHC," *Phys. Lett.* **B710** (2012) 647–653, arXiv:1109.0737 [hep-ph].

[52] L. Frankfurt, V. Guzey, M. Strikman, and M. Zhalov, "Nuclear shadowing in photoproduction of ρ mesons in ultraperipheral nucleus collisions at RHIC and the LHC," *Phys. Lett.* **B752** (2016) 51–58, arXiv:1506.07150 [hep-ph].

[53] **ALICE** Collaboration, D. Horak, "ALICE measurements on ρ^0 photoproduction in Pb-Pb ultra-peripheral collisions,". https://indico.cern.ch/event/433345/contributions/2373716/.

[54] V. P. Goncalves and M. V. T. Machado, "Photoproduction of ρ^0 meson in ultraperipheral heavy ion collisions at the BNL RHIC and CERN LHC," *Phys. Rev.* **C80** (2009) 054901, arXiv:0907.4123 [hep-ph].

[55] G. Sampaio dos Santos and M. V. T. Machado, "Light vector meson photoproduction in hadron-hadron and nucleus-nucleus collisions at energies available at the CERN Large Hadron Collider," *Phys. Rev.* **C91** no. 2, (2015) 025203, arXiv:1407.4148 [hep-ph].

[56] V. Guzey, E. Kryshen, and M. Zhalov, "Coherent photoproduction of vector mesons in ultraperipheral heavy ion collisions: Update for run 2 at the CERN Large Hadron Collider," *Phys. Rev.* **C93** no. 5, (2016) 055206, arXiv:1602.01456 [nucl-th].

[57] **ALICE** Collaboration, K. Oyama, "Reference cross section measurements with ALICE in pp and Pb-Pb collisions at LHC," in *LHC Lumi Days 2012 Geneva, Switzerland, February 29-March 1, 2012*. 2013. arXiv:1305.7044 [nucl-ex].

[58] **ALICE** Collaboration, B. Abelev *et al.*, "Coherent J/ψ photoproduction in ultra-peripheral Pb-Pb collisions at $\sqrt{s_{NN}} = 2.76$ TeV," *Phys. Lett.* **B718** (2013) 1273–1283, arXiv:1209.3715 [nucl-ex].

[59] **ALICE** Collaboration, K. Aamodt *et al.*, "Centrality dependence of the charged-particle multiplicity density at mid-rapidity in Pb-Pb collisions at $\sqrt{s_{NN}} = 2.76$ TeV," *Phys. Rev. Lett.* **106** (2011) 032301, arXiv:1012.1657 [nucl-ex].

[60] A. Adeluyi and C. A. Bertulani, "Constraining Gluon Shadowing Using Photoproduction in Ultraperipheral pA and AA Collisions," *Phys. Rev.* **C85** (2012) 044904, arXiv:1201.0146 [nucl-th].

[61] A. Cisek, W. Schafer, and A. Szczurek, "Exclusive coherent production of heavy vector mesons in nucleus-nucleus collisions at LHC," *Phys. Rev.* **C86** (2012) 014905, arXiv:1204.5381 [hep-ph].

[62] T. Lappi and H. Mantysaari, "J/ψ production in ultraperipheral Pb+Pb and p+Pb collisions at energies available at the CERN Large Hadron Collider," *Phys. Rev.* **C87** no. 3, (2013) 032201, arXiv:1301.4095 [hep-ph].

[63] **ALICE** Collaboration, B. B. Abelev *et al.*, "Exclusive J/ψ photoproduction off protons in ultra-peripheral p-Pb collisions at $\sqrt{s_{\rm NN}} = 5.02$ TeV," *Phys. Rev. Lett.* **113** no. 23, (2014) 232504, arXiv:1406.7819 [nucl-ex].

[64] **ALICE** Collaboration, S. Acharya *et al.*, "Energy dependence of exclusive J/ψ photoproduction off protons in ultra-peripheral p-Pb collisions at $\sqrt{s_{\rm NN}}$ = 5.02 TeV," arXiv:1809.03235 [nucl-ex].

[65] J. E. Gaiser, *Charmonium Spectroscopy From Radiative Decays of the J/ψ and ψ'*. PhD thesis, SLAC, 1982. http://www-public.slac.stanford.edu/sciDoc/docMeta.aspx?slacPubNumber=slac-r-255.html.

[66] **ZEUS** Collaboration, S. Chekanov *et al.*, "Exclusive photoproduction of J / psi mesons at HERA," *Eur. Phys. J.* **C24** (2002) 345–360, arXiv:hep-ex/0201043 [hep-ex].

[67] **H1** Collaboration, C. Alexa *et al.*, "Elastic and Proton-Dissociative Photoproduction of J/psi Mesons at HERA," *Eur. Phys. J.* **C73** no. 6, (2013) 2466, arXiv:1304.5162 [hep-ex].

[68] **LHCb** Collaboration, R. Aaij *et al.*, "Exclusive J/ψ and ψ(2S) production in pp collisions at $\sqrt{s} = 7$ TeV," *J. Phys.* **G40** (2013) 045001, arXiv:1301.7084 [hep-ex].

[69] P. Newman and M. Wing, "The Hadronic Final State at HERA," *Rev. Mod. Phys.* **86** no. 3, (2014) 1037, arXiv:1308.3368 [hep-ex].

[70] **H1** Collaboration, F. D. Aaron *et al.*, "Measurement of the Inclusive ep Scattering Cross Section at Low Q^2 and x at HERA," *Eur. Phys. J.* **C63** (2009) 625–678, arXiv:0904.0929 [hep-ex].

[71] J. Cepila, J. G. Contreras, and J. D. Tapia Takaki, "Energy dependence of dissociative J/ψ photoproduction as a signature of gluon saturation at the LHC," *Phys. Lett.* **B766** (2017) 186–191, arXiv:1608.07559 [hep-ph].

[72] S. P. Jones, A. D. Martin, M. G. Ryskin, and T. Teubner, "Probes of the small x gluon via exclusive J/ψ and Υ production at HERA and the LHC," *JHEP* **11** (2013) 085, arXiv:1307.7099 [hep-ph].

[73] M. G. Ryskin, "Diffractive J / psi electroproduction in LLA QCD," *Z. Phys.* **C57** (1993) 89–92.

[74] I. Bautista, A. Fernandez Tellez, and M. Hentschinski, "BFKL evolution and the growth with energy of exclusive J/ψ and Υ photoproduction cross sections," *Phys. Rev.* **D94** no. 5, (2016) 054002, arXiv:1607.05203 [hep-ph].

[75] N. Armesto and A. H. Rezaeian, "Exclusive vector meson production at high energies and gluon saturation," *Phys. Rev.* **D90** no. 5, (2014) 054003, arXiv:1402.4831 [hep-ph].

[76] **ALICE** Collaboration, B. Abelev *et al.*, "Upgrade of the ALICE Experiment: Letter Of Intent," *J. Phys.* **G41** (2014) 087001.

[77] **ALICE** Collaboration, P. Antonioli, A. Kluge, and W. Riegler, "Upgrade of the ALICE Readout & Trigger System,".

[78] P. Buncic, M. Krzewicki, and P. Vande Vyvre, "Technical Design Report for the Upgrade of the Online-Offline Computing System,".

[79] **ALICE** Collaboration, B. Abelev *et al.*, "Technical Design Report for the Upgrade of the ALICE Inner Tracking System," *J. Phys.* **G41** (2014) 087002.

[80] **ALICE** Collaboration, C. Lippmann, "Upgrade of the ALICE Time Projection Chamber,".

[81] **ALICE** Collaboration, J. Adam *et al.*, "Addendum to the Technical Design Report for the Upgrade of the ALICE Time Projection Chamber,".

[82] **ALICE** Collaboration, A. I. Maevskaya, "Fast Interaction Trigger for the upgrade of the ALICE experiment at CERN: design and performance," arXiv:1812.00594 [physics.ins-det].

[83] **GEANT4** Collaboration, S. Agostinelli *et al.*, "GEANT4: A Simulation toolkit," *Nucl. Instrum. Meth.* **A506** (2003) 250–303.

[84] Z. Citron *et al.*, "Future physics opportunities for high-density QCD at the LHC with heavy-ion and proton beams," in *HL/HE-LHC Workshop: Workshop on the Physics of HL-LHC, and Perspectives at HE-LHC Geneva, Switzerland, June 18-20, 2018*. 2018. arXiv:1812.06772 [hep-ph].

[85] **ALICE MFT Working Group** Collaboration, A. Uras and f. t. A. M. W. Group, "Muon Physics in ALICE: The MFT Upgrade Project," *J. Phys. Conf. Ser.* **446** (2013) 012054, arXiv:1212.6517 [hep-ex].

[86] V. Guzey, E. Kryshen, M. Strikman, and M. Zhalov, "Evidence for nuclear gluon shadowing from the ALICE measurements of PbPb ultraperipheral exclusive J/ψ production," *Phys. Lett.* **B726** (2013) 290–295, arXiv:1305.1724 [hep-ph].

[87] K. Hencken, E. A. Kuraev, and V. Serbo, "Exclusive and inclusive muon pair production in collisions of relativistic nuclei," *Phys. Rev.* **C75** (2007) 034903, arXiv:hep-ph/0606069 [hep-ph].

[88] P. A. Krachkov and A. I. Milstein, "High-energy $\mu^+\mu^-$ electroproduction," *Nucl. Phys.* **A971** (2018) 71–82, arXiv:1712.09770 [hep-ph].

[89] A. J. Baltz, "Higher Order QED Calculation of Ultrarelativistic Heavy Ion Production of mu+ mu- Pairs," *Phys. Rev.* **C80** (2009) 034901, arXiv:0901.0891 [nucl-th].

[90] A. J. Baltz, "Evidence for higher order QED in e+ e- pair production at RHIC," *Phys. Rev. Lett.* **100** (2008) 062302, arXiv:0710.4944 [nucl-th].

[91] **ATLAS** Collaboration, M. Aaboud *et al.*, "Evidence for light-by-light scattering in heavy-ion collisions with the ATLAS detector at the LHC," *Nature Phys.* **13** no. 9, (2017) 852–858, arXiv:1702.01625 [hep-ex].

[92] **CMS** Collaboration, A. M. Sirunyan *et al.*, "Evidence for light-by-light scattering and searches for axion-like particles in ultraperipheral PbPb collisions at $\sqrt{s_{\mathrm{NN}}} = 5.02$ TeV," arXiv:1810.04602 [hep-ex].

[93] **ATLAS** Collaboration, T. A. collaboration, "Observation of light-by-light scattering in ultraperipheral Pb+Pb collisions with the ATLAS detector,".

[94] M. Kłusek-Gawenda, R. McNulty, R. Schicker, and A. Szczurek, "Light-by-light scattering in ultra-peripheral heavy-ion collisions at low diphoton masses," arXiv:1904.01243 [hep-ph].